Thermoelastic and Vibration Response Studies of Shape Memory Alloy embedded Bimorph Composites

A Thesis Presented in Partial Fulfillment
of the Requirements for the Degree of

Doctor of Philosophy

by

Rupal Srivastava

Roll Number 14205265

to the

DEPARTMENT OF MECHANICAL ENGINEERING

INDIAN INSTITUTE OF TECHNOLOGY KANPUR, INDIA

February 2021

POST GRADUATE OFFICE
THESIS SUBMITTED
ON 15-02-2021
I. I. T., KANPUR - 16

Certificate

It is certified that the work contained in this thesis entitled "***Thermoelastic and Vibration Response Studies of Shape Memory Alloy embedded Bimorph composites***", by **Rupal Srivastava (Roll No. 14205265)**, has been carried out under my supervision and this work has not been submitted elsewhere for a degree.

Bishakh Bhattacharya

Dr. Bishakh Bhattacharya
Professor
Department of Mechanical Engineering,
Indian Institute of Technology Kanpur
Kanpur, Uttar Pradesh-208016, India

February 2021

Declaration

This is to certify that the thesis titled "***Thermoelastic and Vibration Response Studies of Shape Memory Alloy embedded Bimorph Composites***" has been authored by me. It presents the research conducted by me under the supervision of Prof. Bishakh Bhattacharya, Department of Mechanical Engineering, IIT Kanpur. To the best of my knowledge, it is an original work, both in terms of research content and narrative, and has not been submitted elsewhere, in part or in full, for a degree. Further, due credit has been attributed to the relevant state-of-the-art and collaborations (if any) with appropriate citations and acknowledgements, in line with established norms and practices.

Rupal Srivastava

Roll no.- 14205265

Department of Mechanical Engineering,

Indian Institute of Technology Kanpur

Kanpur, Uttar Pradesh-208016, India

February 2021

Thermoelastic and Vibration Response Studies of Shape Memory Alloy embedded Bimorph composites

Abstract

Thermoelastic and Vibration Response Studies of Shape Memory Alloy embedded Bimorph composites

In this thesis, the thermoelastic and vibration response analysis of four types of Shape Memory Alloy (SMA) reinforced composites will be discussed. The experimental results have been validated against the numerical results and the optimization of the structure has been conducted using NSGA-II. The vision is to fill the gap for unconventional deployment methods by active shape and vibration control. The present investigation presents an experimental analysis carried out on SMA based unimorph composite and SMA based bimorph (two SMA layers) composite, fabricated in a novel in-house designedalignment device and analysed using laser technology. On performing fabrication followed by mechanical tests of the SMA composites, the deflection about the transverse direction with respect to change in SMA temperature, and the change in the natural frequency upon the actuation of one or both of the SMA layers were obtained using the Laser Doppler Vibrometer (LDV). The results obtained from the experimental modal analysis and simulation involving temperature-dependent mechanical properties were found to be in close proximity. Further, the constitutive equations for the models have been presented, however, since no closed-form solution exists, the finite element model (FEM) is chosen for further analysis. This study has then been extended to SMA reinforced composites with honeycomb core and then to auxetic core. The Gaussian curvature of the synclastic and anticlastic bending response of the composite upon SMA actuation has been analyzed and a new composite to attain bimorph deformation through SMA embedding is proposed. In order, to attain a customized SMA composite with a predefined vibration range and required deflection, the SMA based design variables are identified formulating a multi-objective optimization problem with conflicting objective functions and subsequently solved using the Non-dominated Sorting Genetic Algorithm (NSGA-II). The eigenfrequencies of the SMA composites are found to be coupled, the decoupling is carried out using the optimization algorithm which can additionally interchange the corresponding eigenmodes by input variable optimization. The obtained results indicate that varying the SMA variables can allow us to tune the smart composites to a wider range of applications. It is envisaged that the experimental template integrated with FEM validation, and the optimization algorithm is capable of laying the foundation for complex SMA embedded deployable structures and active composites design.

Acknowledgment

“At times our own light goes out and is rekindled by a spark from another person.”

—*Albert Schweitzer*

I am truly indebted to my supervisor and promoter, Professor Bishakh Bhattacharya, for taking an overenthusiastic girl unsure of her research problem under his wing. More though, for honing and supporting me through this journey. Your ‘always make notes’ and ‘family-first’ are some of the many lessons that will forever stick with me and have made me a better researcher and person. Thank you Chitralekha Ma’am, for welcoming us in the family and making us feel at-home by making sure we ate as much as humanly possible at all our group dinners.

I cannot express how deeply I am touched by the unquantifiable help I have received from Aman, Arun, and Sankalp, my friends-turned-life-coaches. Without you, this would never have been possible, and my dreams of calling myself a ‘researcher’ would have remained unfulfilled. Thank you for being with me in the best and worst of times and for putting up with the ‘occasional’ whining and regular mood swings.

Without friends one would crumble, and I am proud to have found friends who became the pillars of my existence on campus- Anjali, Esha, Himanshu, Khushboo, Rhythm, Shruti, and Vaishnavi; thank you for accepting my vulnerability and being my constant source of motivation. You have helped more than you know and more than I could ever express. With our mismatched schedules, many of us have drifted apart, embarking on our own personal journies, Abhishek Ghosh, Akshay, Aravind, Deval, Dipti, Gagan, Iram, Nancy, Navanya, Pulkit, Rupam, Shubham, Shubh, Srishti, Swati, and many more incredible humans I have come across this adventure; I know we are unable to stay in touch as much as we might want to, still, you are always in my thoughts when I think of people who were with me through the ‘thicks-and-thins’, and for which I am perpetually beholden. I would also like to thank my Hall Executive Committee; you were the most diligent and hardworking set of people I had the opportunity to work with. Aditi, Amrita, Ekta, Pranjul, and Swikriti, you girls taught me the meaning of sisterhood, the importance of balancing research with administrative responsibilities, and how to compartmentalize my professional and personal life. I have deep love and respect for my hostel mess, sanitation, and office staff for making my personal life easier, I cannot fully express my gratitude for taking care of me. And dear Pranav, thank you for letting me be a part of your amazing effort, for giving me a small opportunity to give back to the society, I hope we continue to work in this direction in the future.

I sincerely thank all the previous and current lab members for your cooperation, for maintaining humor, and for introducing me to 'unlimited food' restaurants. Hopefully, we will again in future sit in the Sun with a cup of tea and have 'hour-long' discussions. Dear Anshi, one day you will grow up to be able to read this- thank you for bringing smile to our faces, warmth in our hearts, and being an essential extended member of the lab. Special thanks to Mr. Gyanendra Tripathi, the backbone of our lab, without whom no in-lab experiments are possible, and without Mr. Chandrashekhar Yadav how will we ever figure out the complex official procedures? I further want to extend my gratitude to Praveen Kumar D., Ranjit Kumar, and Dr. Sahil Kalra for their contribution to the experimental analysis and material characterisation of the shape memory alloys employed in this dissertation.

I would also like to take a moment and express my immense gratitude for my friends, Ankur, Asil, Neha Rani, Neha Singh, Niharika, Pragya, Priya, Shikhar, and Sumaiya; my temporary sweet escapes from the Ph.D. hustle. I hope to have you all in my life for many more decades, and I shyly urge your forgiveness for when in future I might go *awol* again. And if not for my best friend and constant companion, Abhishek Verma, I might not have opted IIT Kanpur for Ph.D., you have changed the course of my life forever and I am eternally in debt of you.

In the end, I would like to thank my family, who have dedicated their life to me and my goals. Thank you, Shivang, my little brother, for being my anchor and my safe harbor, for knowing exactly how I am feeling and for having the right memes to cure me. Your infectious laughter and 'take everything as lightly as possible' has got me through the challenging times and healed me again and again. And my beloved parents, my source of inspiration and constant motivation, for supporting me emotionally, physically, and even financially. For having faith in me when I lacked, for putting trust in me when I won't, and above all, for never pushing me to 'settle' down; for loving me unconditionally, through all the times, even when I was 'too busy', I promise to never be as busy ever again.

Finally, to the rebellious city, which has grown on me, and has embedded its essence to my soul... Kanpur.

Rupal Srivastava

ॐ

कर्पूरगौरं करुणावतारं संसारसारं भुजगेन्द्रहारम्।
सदा वसन्तं हृदयारविन्दे, भवं भवानीसहितं नमामि ||
-- यजुर्वेदः

Dedicated to

My great-grandfather, Late Shri Shankar Nath Srivastava,
who valued education above all, for all.

Contents

List of Figures **xiii**

List of Tables **xx**

Nomenclature **xx**

1 Introduction **1**

1.1 Motivation 1

1.2 An envisaged application of Shape Memory Alloy embedded composites: Gossamer Structures 2

1.3 Shape Memory Alloys 7

1.4 Auxetic Structures 13

1.5 Constitutive Modelling and Optmization 15

1.6 Research Methodology and Organisation 17

1.7 Closure 19

2 Mechanical Testing and Material Characterisation **22**

2.1 Parameters required for the ECTE Model 22

2.1.1 Block Recovery Test [σ_r] 23

2.1.2 Temperature controlled Tensile test [E_a] 23

2.2 Composite Mechanical Properties 26

2.3 Summary 29

3 Thermoelastic Response Analysis **31**

3.1 Specimen Fabrication 32

3.2 Results and Discussion 38

3.2.1 Single layer SMA embedded smart composite 38

3.2.2 Two layers SMA embedded smart composite 40

3.3 Summary 44

4 Free Vibration Response Analysis **45**
4.1 Experimental setup 45
4.2 Results and Discussion 49
4.2.1 Case I: Thermal actuation of SMA layer with 0°orientation angle . . 51
4.2.2 Case II: Thermal actuation of SMA layer with 90°orientation angle 53
4.2.3 Case III: Thermal actuation of both the SMA layers when connected in series 53
4.2.4 Case IV: Thermal actuation of both the SMA layers when connected in parallel 54
4.3 Summary 56

5 Constitutive Models and Mathematical Formulation **58**
5.1 Brinson 1D Constitutive Model 58
5.2 Turners Effective Coefficient of Thermal Expansion Model (ECTE) 63
5.3 Reduced Stiffness Matrix and Rule-of-Mixtures 65
5.4 Homogenization formulation for Periodic Honeycomb layer 67
5.5 Governing equations of SMA Hybrid Composite (SMAHC) plate 70
5.5.1 The stress field 71
5.5.2 The axial forces, shear forces, and the bending moment 73
5.6 Summary 76

6 Numerical Modeling and Parametric Study **78**
6.1 Specimen Configuration 78
6.2 Finite Element Modeling and Analysis 82
6.3 Results and Discussion 86
6.3.1 Thermoelastic Response 86
6.3.2 Bimorph radius of curvature 88
6.3.3 Free Vibration Response 92
6.4 Parametric study on the Honeycomb/Auxetic core and the SMAHC 94
6.4.1 Effect of reentrant angle 94
6.4.2 Effect of SMA fiber volume fraction and fiber angle orientation . . . 94
6.4.3 effect of volume fraction and reentrant angle of honeycomb constituent fiber 100
6.5 Summary 102

7 Evolutionary Optimisation and Eigenmode Decoupling **1**
7.1 Optimisation Problem Formulation 2
7.2 Optmisation Technique Comparison Study 4

7.3 Results and Discussion 10
7.3.1 Case 1: SMA unimorph 10
7.3.2 Case 2: SMA bimorph 13
7.3.3 Case 3: SMA bimorph with honeycomb core 14
7.3.4 Case 4: SMA bimorph with auxetic core 14
7.4 Summary 16

8 Conclusions and Future Work 18
8.1 Part I- Experimental analysis of Unimorph and Bimorph SMA Hybrid Composites 19
8.2 Part II- Numerical analysis of Unimorph and Bimorph SMA Hybrid Composites 20
8.3 Part III- Structural Optimisation of Unimorph and Bimorph SMA Hybrid Composites 22
8.4 Future Scope 23

Papers from Dissertation 26

Bibliography 27

List of Figures

1.1 A gossamer spider web has a higher Elastic modulus than Nylon 6. The Merriam-Webster Dictionary defines Gossamer as- a film of cobwebs floating in air in calm clear weather. (Photo by Tamas Tuzes-Katai on Unsplash.) 3
1.2 A timeline of the major Gossamer Space Structures advancements. With an increase in budget and sustainable space missions, a need to reduce payload and reuse existing technology by transforming it to current needs is becoming popular 4
1.3 Photograph of the deployed inflatable antenna system from Shuttle of the Spartan-207/IAE freeflyer (image credit: NASA). 5
1.4 Various rigidisation and inflation techniques used in conventional space inflatable structures as well as the proposed technique. 6
1.5 A toroidal structure is composed of postive, negative, and zero Gaussian curvature points causing spehrical, hyperboloidal, and cylindrical surfaces. 7
1.6 Stress-Strain-Temperature diagram of shape memory alloys showing Shape Memeory Effect and Superelasticity or Pseudoelasticity 8
1.7 The Reinvented Wheel by NASA for the Mars Rover consists of NiTiNOL mesh in austenite phase, thus able to bear large stresses without undergoing plastic deformation. This behavior is also called Pseudoelasticity. 9
1.8 A thermally activated soft artificial muscle is actuated with embedded wires of NiTiNOL and used for caudal fin locomotion of a swimming robot [Bartlett et al. (2017)]. 10
1.9 Application domain of Shape Memory Alloys. The Superelastic property finds more commercial applications as compared to the Thermal Shape Memory Effect. 11
1.10 Schematic diagram of positive and negative Poisson's ratio upon tensile loading applied to an undeformed bar (dashed line) in the longitudinal (x) direction. a) Non-auxetic behavior- lateral contraction and longitudinal extension (solid line). b) Auxetic behavior- longitudinal as well as lateral extension (solid line). 14

1.11 Summary of *'Part I: Experimental analysis of SMA embedded composites'*. 17
1.12 Summary of *'Part II: Numerical analysis of SMA embedded composites'*, and *'Part III: Structural Optmization of SMA embedded composites'*. 18
1.13 SMA reinforced single layered, honeycomb, and reentrant honeycomb core composites to obtain the three Gaussian curvatures of a toroidal structure- zero, negative, and positive respectively. 20

2.1 Tensile testing machine used for conducting temperature controlled stress-strain analysis (left), and inside view of the temperature chamber showing grippers holding a fixture mounted with NiTiNOL HT375 wire (right). . . 24
2.2 Experimental data requierd for Turner's Model. The sudden drop in the graph at 66°C is attributed to the phase transformation from Martensite to Austenite 25
2.3 Woven E-glass fiber (left) and E-glass fiber-reinforced Silicone matrix (right) constrained in the Instron 1195 Universal Testing Machine. In the case of Silicone matrix reinforced with glass fibers, the matrix is yielding and deforming plastically while the fibers are continuing to stretch elastically. . . 26
2.4 True stress-strain curves for woven E-Glass fiber and Silicone laminated E-glass fiber. A 165% increase in peak stress capability is observed. 29

3.1 Computer-Aided Design (CAD) model of the alignment frame device for the manufacturing of the unidirectionally and bidirectionally embedded NiTiNOL wires in soft composites. A set of vertically and horizontally movable plates are used to fix, align, and make the wires taut during the hand lay-up manufacturing of the SMAHCs. 33
3.2 Manufacture fixture/alignment frame for the SMAHC fabrication. Top view (a) of fixture with embedded composite and front view (b) of fixture. The fixtures has two horizontally movable and four vertically movable and detachable plates for the constraining of the SMA wires. 34
3.3 Schematic diagram of single-layer [(a)] and two-layer [(b)] SMAHC. The NiTiNOL wires are embedded in a digitated pattern and actuated through Joule heating. The offset embedding causes the composite bending upon SMA thermal actuation (thereby its contraction). 35
3.4 Experimental setup for the thermoelastic response analysis of the single-layer SMAHC (left), and two-layer bimorph SMAHC (right). The deflection of single-layer SMAHC upon SMA thermal actuation by Joule heating was observed using a sinle point laser sensor, whereas for the bimorph SMAHC was investugated through image processing method. 36

3.5 Deflection profile of single layer SMA composite. Since the SMA wire is embedded at an offset, its thermal actuation by Joule heating causes the composite to bend. As SMA contracts, the compression and tensile forces at either end of the thickness cause the bending. The SMAHC goes from the initial position with no deflection(a) to a maximum of 45mm (f) (average) deflection. . . . 37
3.6 Top fiber tip deflection of single-layer SMA embedded composite. A maximum curvature obtained was 0.2 corresponding to 14V and an average of 45mm deflection was observed in this case. A residual displacement of 5mm was observed in the composite upon return with no external cooling caused due to the stiffness of the E-glass fiber. . . . 39
3.7 Beam deflection profile with increasing volatge for single-layer SMA reinforcement. . . . 40
3.8 Schematic showing the thermal conductivities of the constituents materials. In Case II, when the top SMA ply is actuated, the heat is dissipated along the z-direction. This leads to losing heat to the surroundings, and the second SMA ply is not actuated. However, when the second ply is actuated, the trapped heat actuates the first SMA ply as well. Since the SMA wires are embedded orthogonally, the motion is highly constrained, and hence a diminished bimorph behavior is obtained. . . . 41
3.9 Bidirectional bending of the two-layer active bimorph SMAHC . . . 42
3.10 Deflection profile of Active Bimorph Composite with two layers of SMA reinforcement. (a) First layer (actuated) side B (image processing data), (b) First layer side C, (c) First layer side D, (d) Second layer side A, (e) Second layer side B, and (f) Second layer side C. . . . 43

4.1 Block diagram for bimorph SMAHC modal analysis along with the actuation setup and sensing mechanism. . . . 46
4.2 Schematic of basic components of LDV scanning head. Source- Wikipedia Public Domain- no copyright image. . . . 47
4.3 Experimental setup- (a) 3D Laser Doppler Vibrometer, (b) LDV software showing the assigned response points, (c) Bimorph SMAHC specimen placed horizontally on the electromagnetic shaker, and the incident laser beam. . . . 48
4.4 Current input function generated using the programmable DC supply. . . . 49

4.5 Schematic of SMA layer actuation cases: thermal actuation of- (I) SMA layer with 0°fiber orientation angle, (II) SMA layer with 90°fiber orientation angle, (III) both the SMA layers when SMA wires are connected through series connection, and (IV) both the SMA layers when SMA wires are connected through parallel connection. 50
4.6 Natural frequency of the bimorph SMAHC with varying SMA layer actuation and series/parallel connection. Case I- when SMA layer with 0°orientation angle is actuated, Case II- when SMA layer with 90°orientation angle is actuated, Case III- when both SMA layers are actuated with series connection, and Case IV- when both SMA layers are actuated with parallel connection. The dependence of the ferquency is also plotted against the velocity of the structure; thus a minimum value of zero is shown in the figure. 51
4.7 Young's modulus as a function of total martensite fraction (stress-induced + temperature-induced), plotted from Brinson's model Brinson (1993). . . 52
4.8 Summarising the change in natural frequency with increase in SMA temperature. Case I: 0°SMA, Case II: 90°SMA, Case III: Series connection, Case IV: Parallel connection. Note- Each frequency shown is an average of five sets of experiments with error within 5%. 55

5.1 Stress-strain curves for varying temperatures obtained plotted against Brinson Model 62
5.2 Brinson 1D Model for shape memory alloys. (a) Martensite Fraction vs Temperature. $\xi_{so} = 0$, $\xi_{to} = 1$, T = 5°C from stress-strain analysis with $\sigma_o = \epsilon_o$. (b) Residual Strain vs Temperature. $\xi_{so} = 0.02/\epsilon_L$, $\xi_{to} = 0.5$, (c) Martensite Fraction vs Temperature. $\xi_{so} = 0.02/\epsilon_L$, $\xi_{to} = 0.5$, (d) Recovery Stress vs Temperature. $\epsilon_o = 0.5\%$ & 0.9%, $\xi_{so} = 0.046$ & 0.073, $\xi_{to} = 0$ & 0.92, $\sigma_o = 128$ 62
5.3 Volume element of the SMAHC lamina [Turner (2000)]. 63
5.4 Representative volume element of the honeycomb lamina; l, h are the inclined and the vertical honeycomb struts respectively, t is the thickness of the strut; h= 2.5 x l. 69
5.5 Variation of different non-dimensionalised mechanical properties with cell angle θ for honeycomb ($\theta > 0°$) and reentrant honeycomb ($\theta < 0°$) lattices for $h/l = 2$ 70
5.6 Bending of an element of the smart composite in X-Z plane showing both mid-plane deformation as well as pure bending. Shear deformation is neglected in this model. 72
5.7 Stress resultant and moments in SMAHC plate mid-plane. 74

5.8 Schematic of ply lay-up of SMA wire embedded unimorph composite. . . . 75

6.1 Schematic of SMA wire embedded composite [Srivastava et al. (2018)], SMA is shown digitated as fabricated for experiment. 79
6.2 Schematic of SMA wire embedded honeycomb ply (positive reentrant angle - positive Poisson's ratio) and auxetic ply (negative reentrant angle - negative Poisson's ratio). (a) Honeycomb layer with SMA wire/fiber-reinforcement, (b) Auxetic layer with SMA wire/fiber-reinforcement; (refer Figure 5.4 for strut details). 81
6.3 Schematic of SMA wire embedded composites- unimorph SMAHC, bimorph SMAHC, and hoeycomb/auxetic plies- laminate configuration and dimensions. (a) A two-ply unimorph with unidirectional SMA, (b) A four-ply bimorph with cross-ply reinforcement of SMA, and (c) A two-ply honeycomb/reentrant-honeycomb bimorph with unidirectional SMA. . . . 84
6.4 Flow-diagram of thermoelastic and vibration response finite element analysis of the SMA embedded unimorph and bimorph SMAHC, and honeycomb & auxetic ply. 85
6.5 Validation of the numerical model against experimental results, SMA fiber volume fraction, (V_f^{SMA})= 0.024, E-glass fiber volume fraction, (V_f^{EGF}) = 0.7, SMA fiber orientation angle, (θ^{SMA})= 0°. 87
6.6 Deflection of SMA reinforced bimorph composites upon thermal actuation. $V_f^{EGF} = 0.7$ (two unidirectional plies orthogonally to model the woven ply), $V_f^{SMA} = 0.024, \theta^{SMA} = 0°$, strut fiber volume fraction, $V_f^h = 0.9, \theta^h = \pm 60°$. 88
6.7 Node points for curvature analysis; nodes denote radius of curvature at: $R_c^{x'}$= minimum deflection centerline point, R_c^x= maximum deflection centerline point, $R_e^{y'}$= minimum deflection edge point, R_e^y= maximum deflection edge point. 89
6.8 Deflection of SMA reinforced bimorph composites upon thermal actuation. $V_f^{EGF} = 0.7$ (two unidirectional plies orthogonally to model the woven ply), $V_f^{SMA} = 0.024, \theta^{SMA} = 0°$, strut fiber volume fraction, $V_f^h = 0.9, \theta^h = \pm 60°$. 90
6.9 Deflection of SMA reinforced bimorph composites upon thermal actuation. $V_f^{EGF} = 0.7$, $V_f^{SMA} = 0.024, \theta^{SMA} = 0°$, strut fiber volume fraction, $V_f^h = 0.7, \theta^h = \pm 30°$. 91
6.10 Free vibration response of unimorph and bimorph SMAHC. Note that the natural frequencies are more widely distributed in the case of unimorph SMAHC (41.79 Hz - 200.916 Hz) in comparison to bimorph SMAHC (38.475 Hz - 176.94 Hz). $V_f^{EGF} = 0.7$, $V_f^{SMA} = 0.024, \theta^{SMA} = 0°$. 93

6.11 Free vibration response of SMA embedded honeycomb and auxetic ply. Note that for SMA embedded honeycomb and auxetic ply, the first two modes (bending and coupled bending-twisting mode) are widely separated in comparison to all other structures indicating strong decoupling of the fundamental frequencies. $V_f^{EGF} = 0.7$, $V_f^{SMA} = 0.024, \theta^{SMA} = 0°$, strut fiber volume fraction, $V_f^h = 0.7, \theta^h = \pm 30°$. 93
6.12 Effect of strut fiber volume fraction (V_f^h) on the elastic modulus of the honeycomb and the auxetic ply. θ^h increment at 0.01. 96
6.13 Effect of V_f^h on the Poisson's ratio of the honeycomb and the auxetic ply. θ increment at 0.01. 97
6.14 Effect of V_f^h on the shear modulus of the honeycomb and the auxetic ply. θ increment at 0.01. 98
6.15 Deflection of SMA reinforced composites upon thermal actuation. 99
6.16 Effect of V_f^h and θ^h on the deflection and natural frequency of the honeycomb and the auxetic ply. 101

7.1 Schematic of SMA wire embedded composites- unimorph SMAHC, bimorph SMAHC, and honeycomb/auxetic core SMAHC- laminate configuration and dimensions (non-optimised). 4
7.2 Comparison study of MOPS, NCGA, and NSGA II algorithm when no constraints are proided. The desired optimised design parameters lie in Section III of NSGA-II results as show in the figure. The selection and application of constraint is based on the NSGA-II results. 6
7.3 Basic structure and sequence of the evolutionary algorithm 7
7.4 Flow-diagram explaining the steps for the finite element modelling of the SMAHC cases- multi-objective optimisation comparison, objective functions, and variable constraints. 9
7.5 Single objective opmisation of the SMA unimorph for maximising deflection 7.5a, and 7.5b, minimising first eigenfrequency 7.5c, and 7.5d, and maximising second eigenfrequency 7.5e, and 7.5f. 11
7.6 Pareto Optimal Curve for the unimorph SMAHC sample case (Case 1), single variable- θ with deflection and decoupling bounds. 12
7.7 Pareto Optimal Curve for the unimorph SMAHC sample case (Case 1), multi-variable- θ and t, with deflection and decoupling bounds. 12
7.8 Pareto Optimal Curve for the bimorph SMAHC sample case (Case 2), multi-variable- θ and t, with deflection and decoupling bounds. 13
7.9 Pareto Optimal Curve for the bimorph SMAHC with honeycomb ply sample case (Case 3), multi-variable- θ and t, with only deflection bounds. . . . 15

7.10 Pareto Optimal Curve for the bimorph SMAHC with reentrant-honeycomb ply sample case (Case 4), multi-variable- θ and t, with only deflection bounds. 15

8.1 A sequential representation of the steps involved for the design of SMAHC based torus for controlled shape control of deployment and rigidisation process. 24

List of Tables

2.1 Mechanical testing results for the woven E-glass fiber and E-glass fiber reinforced silicone matrix 27

2.2 Manufacturer provided material properties of E-glass fiber (Azo Materials, Asia), Silicone rubber (Dragon Skin™ 30, Smooth-On, Pennsylvania, USA), and NiTiNOL wire (Dynalloy Inc.) 28

3.1 Flexinol HT90 SMA Wire properties for 1m wire with 3-5% deformation . 36

4.1 Input current vs natural frequency result for all the four cases. Case I: 0 SMA actuation, Case II: 90 SMA actuation, Case III: Series SMA actuation, Case IV: Parallel SMA actuation. 54

5.1 SMA material properties used for the Brinson (1993) model. 61

6.1 Equivalent orthotropic material properties for E-glass fiber-Silicone rubber matrix lamina 80

6.2 Equivalent material properties for E-glass fiber-Silicone rubber matrix-honeycomb struts 80

6.3 Equivalent temperature dependent orthotropic mechanical properties for SMA fiber (NiTiNOL)-Silicone rubber matrix lamina, $E_2 = 3.46\times10^2 kPa, G_{12} = G_{13} = 1.162 \times 10^2 kPa, G_{23} = 88 kPa, \nu_{12} = 0.474$, and $\rho = 1.2 \times 10^3 kg/m^3$. 80

6.4 Equivalent orthotropic material properties for honeycomb and auxetic ply, strut fiber volume fraction (V_f^h)= 0.9, reentrant angle $\theta^h = 60^{\circ}$, (refer Figure 5.4 for strut details). 82

6.5 Summary of all SMA embedded composites. EGF-SM: E-glass fiber-Silicone matrix, H: Honeycomb ply, RH: Reentrant-honeycomb ply 92

7.1 Optimised vs non-Optimised deflection and eigenfrequencies for the four sample cases. 16

Nomenclature and Acronyms

$[\bar{Q}]$	Compliance Matrix
$[Q]$	Reduced Stiffness Matrix
α	Coefficient of Thermal Expansion
α_f	Fiber Coefficient of Thermal Expansion
α_m	Matrix Coefficient of Thermal Expansion
β	Angle between laser beam and velocity direction
ϵ	Strain
ϵ_L	Maximum Recoverable Strain
ϵ_o	Initial Strain
γ	Shear Strain
κ	Principal Curvature
$\kappa_x, \kappa_y, \kappa_z$	Plate curvature about x-, y-, and z-direction
λ	Wavelength of the incident beam
ν	Poisson's Ratio
ν_a	SMA Poisson's Ratio
ν_f	Fiber Poisson's Ratio
ν_m	Matrix Poisson's Ratio
Ω	Transformation Tensor
ρ_f	Fiber Density
ρ_h	Density of honeycomb cell
ρ_m	Matrix Density
ρ_s	Density of the honeycomb material
σ	Stress
σ_f^{cr}	Critical Stress Finish
σ_o	Initial Stress
σ_r	Recovery Stress
σ_s^{cr}	Critical Stress Start
σ_{ro}	Initial Recovery Stress

τ	Shear Stress
Θ	Thermal Coeffiecient of Expansion (Brinson Model)
θ	Honeycomb cell Reentrant angle
θ^h	Reentrant angle
θ^{SMA}	SMA fiber orientation angle
ξ	Total Martensite Volume Fraction
ξ_s	Stress-induced Martensite Volume Fraction
$\xi_s o$	Initial Stress-induced Martensite Volume Fraction
ξ_t	Temperature-induced Martensite Volume Fraction
$\xi_t o$	Initial Temperature-induced Martensite Volume Fraction
A_f	Austenite Finish Temperature
A_s	Austenite Start Temperature
C_A	Stress Influence Coefficient for Austenite Phase
C_M	Stress Influence Coefficient for Martensite Phase
E_A	SMA Young's Modulus in Austenite Phase
E_a	SMA Young's Modulus
E_a	SMA Young's modulus
E_f	Fiber Young's Modulus
E_M	SMA Young's Modulus in Martensite Phase
E_m	Matrix Young's Modulus
E_o	Initial Young's Modulus
E_s	Honeycomb material Young's modulus
EF_1, EF_2	First and second Eigenfrequency
f_c	Frequency of the carrier beam
f_d	Doppler Shift
f_o	Frequency of the initial incident beam
G_a	SMA Shear Modulus
G_m	Matrix Shear Modulus
G_s	Honeycomb material Shear Modulus
M_f	Martensite Finish Temperature
M_s	Martensite Start Temperature
$R_c^{x'}$	Minimum deflection centerline point
R_c^x	Maximum deflection centerline point
$R_e^{y'}$	Minimum deflection edge point
R_e^y	Maximum deflection edge point
T_o	Initial Temperature

u_o, v_o, w_o	Mid-plane displacement along x-, y-, and z-direction
U_{mag}	Maximum deflection
V_a	SMA Volume Fraction
V_f	Fiber Volume Fraction
V_f^h	Honeycomb Fiber Volume Fraction
V_m	Matrix Volume Fraction
V_{in}	Input Voltage
V_{out}	Output Voltage
M	Equivalent Moment tensor
N	Stress resultant tensor
K	Gaussian Curvature
ABS	Active Bimorph Structure
ASC	Active Surface Compensation
c	Speed of light
CAD	Computer Aided Design
CLPT	Classical Laminated Plate Theory
CNT	Carbon Nanotubes
d	Sample Tip Displacement
E	Young's Modulus
ECTEM	Effective Coefficient of Thermal Expansion Model
f	Frequency of the incident beam
FRP	Fiber-Reinforced Polymer
G	Shear Modulus
h	Height of the honeycomb cell
HIAD	Hypersonic Inflatable Aerodynamic Decelerator
IAE	Inflatable Antenna Experiment
IN-STEP	In-Space Technology Experiments Program
K	Bulk Modulus
l	Length of the inclined honeycomb cell strut
LaRC	Langley Research Centre
LDV	Laser Doppler Vibrometer
MOPS	Multiobjective Particle Swarm
N	Newton
NAL	National Aerospace Laboratories
NASA	National Aeronautics and Space Administration
NCGA	Neighbourhood Cultivation Genetic Algorithm

NiTiNOL	Nickle-Titanium Alloy, Naval Ordinance Laboratory
NSGA	Non-dominated Sorting Genetic Algorithm
OV	Oribitting Vehicle
PasComSat	Passive Communication Satellite
SMA	Shape Memory Alloy
SMAHC	Shape Memory Alloy Hybrid Composite
SME	Shape Memory Effect
SMPU	Shape Memory Polyurethanes
T	Temperature
t	Thickness of the honeycomb cell strut
UCS	Union of Concerned Scientists
UTM	Universal Testing Machine
UV	Ultraviolet
V	Applied voltage
v	Velocity of the vibrating surface

Chapter 1

Introduction

1.1 Motivation

The curiosity of the human race has led to great technological endeavours and driving the exploration of heaven and the Earth. The quest for space exploration began in the 1950s when on Oct. 4, 1957, the first artificial satellite, Sputnik 1, was launched by the Soviets into space, and today, as per the Union of Concerned Scientists (UCS) database, we have 2,666 active satellites in space (April 2020 records). Satellites have not only pushed the boundaries of telecommunication and navigation but have also enabled scientists to monitor natural disasters and issue warnings, surveillance and security, scout the planet for mineral reserves, and deep space imaging and understanding. Even with varying objectives, space exploration is associated with a similar set of challenges such as, expenditure on the development and testing and the cost of heavy payload. Hence, the research for soft and lightweight inflatable space structures was pioneered by the ECHO I and II experiments in the late 1950s and early 1960s by NASA LaRC [Elder (1995)].

However, several challenges were faced during the deployment, inflation, and rigidisation of these structures; uncontrolled inflation and deployment were among the main challenges and the risk of degassing due to space debris impact causing abrasion. Several methods of deployment and inflation have been experimentally explored to overcome these challenges, however, an absolute solution is yet to be achieved. This thesis presents one such solution for the deployment and subsequent rigidisation of an inflatable toroidal space structure for antenna support. We investigate shape memory alloy reinforced composites for this purpose and present experimental, numerical, and optimised model of the same. The following section discusses the need and emergence of space inflatable Gossamer structures and its evolution through technological advancements.

1.2 An envisaged application of Shape Memory Alloy embedded composites: Gossamer Structures

The word Gossamer is borrowed from nature for space inflatable structures, given the similarities in the material behavior of these structures with a thin film of floating cobwebs. The ultra-lightweight and high modulus of elasticity of spider silk makes it a unique material, thus inspiring several research applications. With an increased focus on space exploration, the search for budget space programs became necessary, and reducing the payload costs was an effective method in this direction. Thus, the concept of compact structures (later named as Gossamer space structures), which can be stowed during the launch and deployed in space, thereby increasing their size manifolds, has become a focal point of interest. These smooth and thin membrane inflatable structures reduce thermal gradient in space and can withold heavy load over an extensive surface area even with negligible inherent bending stiffness. They can without constraint also conform to curved as well as complex surfaces, and with an optimised design, can aid in eliminating distortions on surface acting in opposition to a continuous restoring inflation pressure.

The first successful demonstration of the inflatable structure technology was in the 1960s when NASA launched an inflatable Mylar balloon with a vapour-deposited aluminium layer- Project ECHO, a passive communications satellite for reflecting radio and radar signal [Shapiro and Jones (1960)]. However, this concept was liquidated due to the unwanted solar sail effects experienced by the ECHO I and II missions and replaced by technologically advanced OV1-8 PasComSat (Passive Communication Satellite) launched by the United States Air Force in 1966. Following the success of these missions, the application domain of Gossamer structure has expanded to antenna bases, solar sails, and modular habitats at the International Space Station [Valle and Wells (2017)]. A detailed timeline of the evolution of the Gossamer structures technology is shown in Figure 1.2.

Figure 1.1: A gossamer spider web has a higher Elastic modulus than Nylon 6. The Merriam-Webster Dictionary defines Gossamer as- a film of cobwebs floating in air in calm clear weather. (Photo by Tamas Tuzes-Katai on Unsplash.)

In the realm of inflatable space structures, the toroidal configuration holds a discernible position for structural support to communication antennas and solar sails. The double curvature profile of a torus causes coupling between bending and stretching, thus preventing large deflection when compared to other geometries [Sharma and Bhattacharya (2019)]. The famous Inflatable Antenna Experiment (IAE) in the 1990s, demonstrated and established the potential of a large, low-cost inflatable antenna structure [Freeland et al. (1997)]. In a collaborative project under the IN-STEP (In-Space Technology Experiments Program) between NASA and LGarde Inc., a deployable aluminized Mylar antenna supported by Neoprene coated Kevlar torus of 14m diameter was launched on May 19, 1996 [Figure 1.3]. The canister with the stowed inflatable struts, torus, and the antenna was opened and deployment was carried out by the floor plate loaded with springs. The struts and the antenna supporting torus were inflated using nitrogen gas followed by the tension and inflation of the lenticular reflector.

The success of the IAE experiment opened doors to a multitude of inflated torus-based space applications such as the pressurised torus and multi-torus space habitat [Geuskens et al. (2013)], and the Hypersonic Inflatable Aerodynamic Decelerator (HIAD) structure [Young et al. (2017)]. Several space exploration agencies have carried out a series of exper-

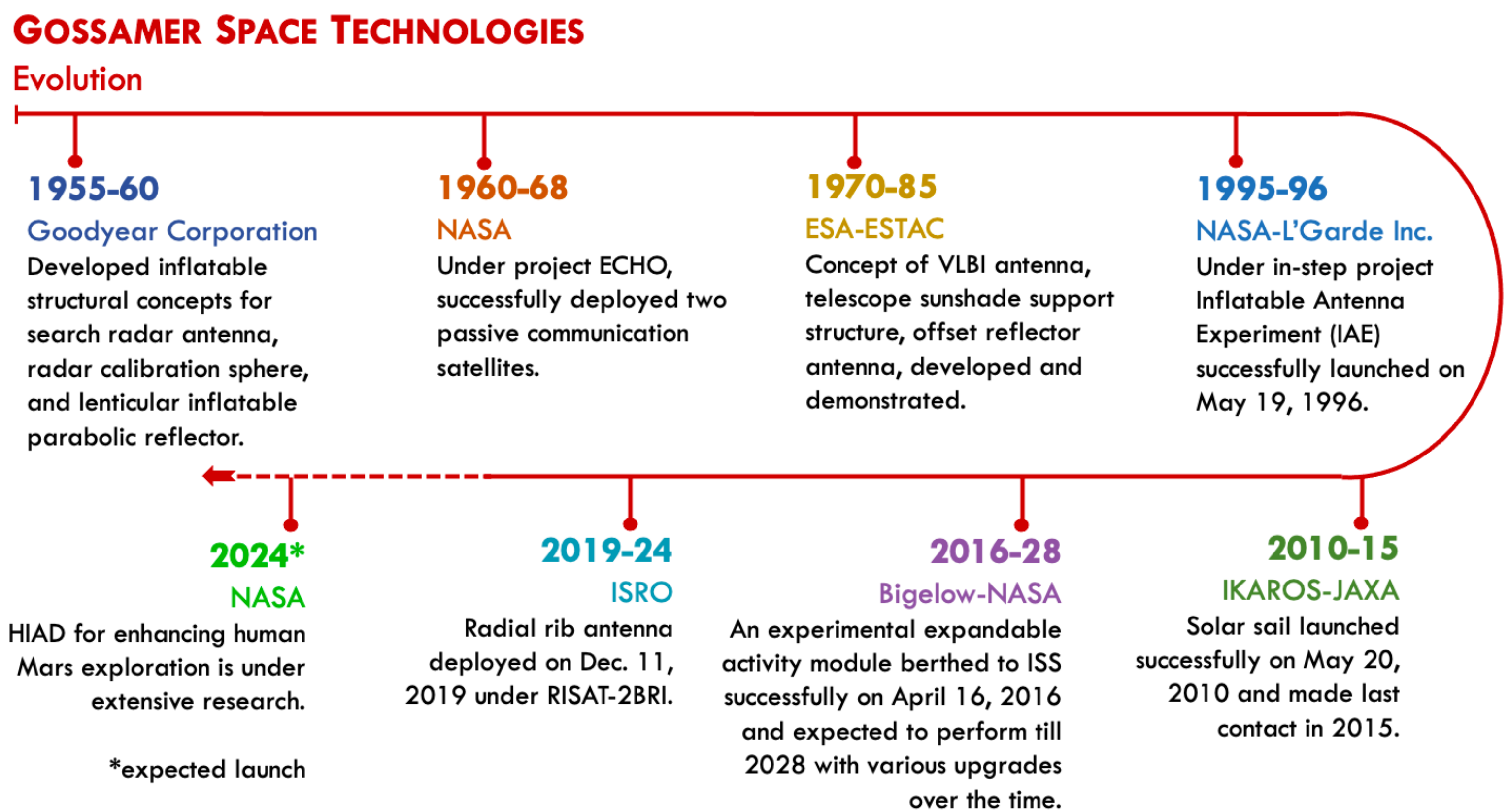

Figure 1.2: A timeline of the major Gossamer Space Structures advancements. With an increase in budget and sustainable space missions, a need to reduce payload and reuse existing technology by transforming it to current needs is becoming popular

iments on deployable membrane antennas; however, the longevity of these structures is yet to be improved. Some other challenges for space inflatables that were established through the IAE were unexpected dynamics during the ejection process, near-instant expansion of the inflatables, uncontrolled and sequential inflation causing incomplete tension in the lenticular structure, and finally, degassing due to leakage.

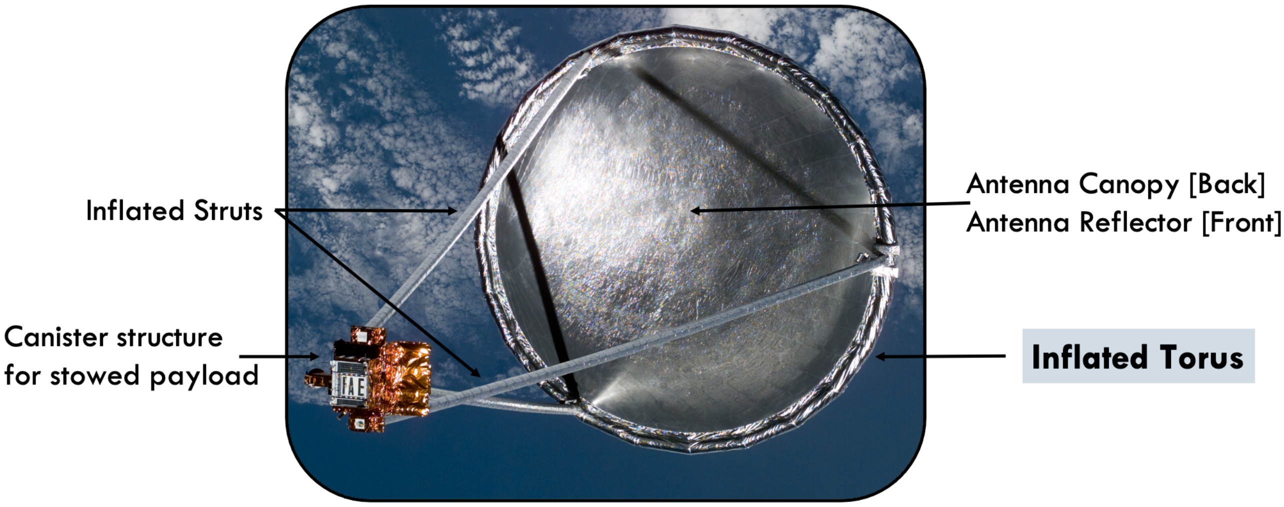

Figure 1.3: Photograph of the deployed inflatable antenna system from Shuttle of the Spartan-207/IAE freeflyer (image credit: NASA).

The inflation and rigidisation of torus membrane structures pose several challenges depending upon the method involved. The chemical rigidisation of deployable structures is done by impregnating the membrane with photoinitiators and UV curable resins, which rigidizes the structure in the desired shape upon deployment and exposure to sunlight [Allred et al. (2002)]. However, the loss of process control and cure time due to shadowing and the thermosetting nature of the photo-initiated materials limit this method to specific applications.

Another inflation method proposed for future space applications is electrostatic inflation of the Gossamer structures. In this method, through active charge emission, the structure is subjected to an electrostatic charge which leads to repulsive electrostatic forces and subsequent inflation of the membranes into a partially rigid structure [Stiles et al. (2010)]. For the purpose of self-repulsion and to negate the differential forces due to solar radiation and drag due to atmosphere and gravity, high potentials are required to produce large electrostatic forces. The high potential requirement is one of the challenges of this design. The electrostatic discharge can cause harm due to the differentially charged components. The conventional and current rigidization and inflation techniques are explained in the infographic Figure 1.4.

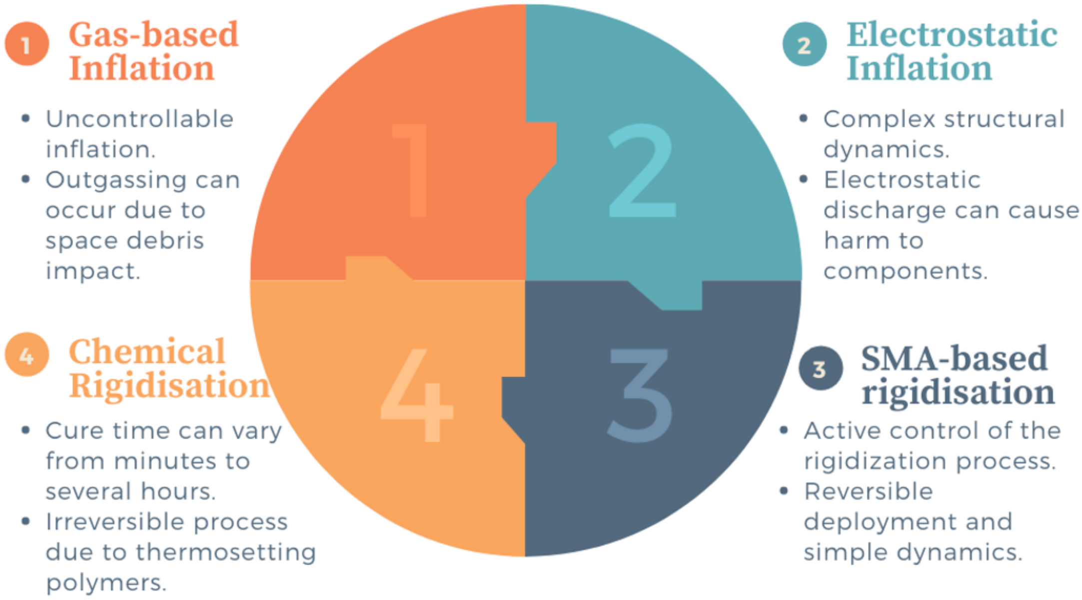

Figure 1.4: Various rigidisation and inflation techniques used in conventional space inflatable structures as well as the proposed technique.

The present thesis targets a novel inflation method using shape memory alloy (SMA) embedded in composites to form elementary parts of a toroidal structure. As shown in Figure 1.5, a toroidal structure is a combination of spherical, hyperboloidal, and cylindrical surfaces caused due to the negative, positive, and zero Gaussian curvatures.[1]

To achieve these curvatures, we extract anticlastic and synclastic behavior from SMA embedded composites of positive and negative Poissons ratio (ν), respectively. For this, we utilise the thermally actuated bending caused in the structure due to the shape memory effect (SME) of the SMA fibers embedded at an offset. As we will see in the following

[1]In differential geometry, the Gaussian curvature, K of a surface at a point is the product of the principal curvatures, κ_1 and κ_2, at the given point: $K = \kappa_1\kappa_2$. [Taken from Pollard and Fletcher (2005)]

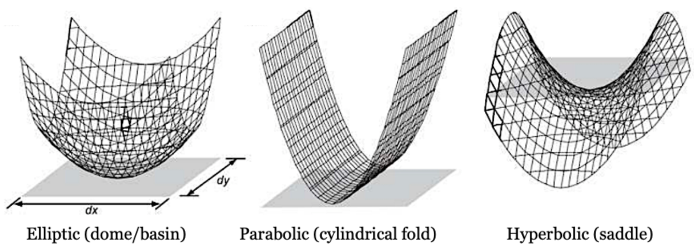

chapters, embedding shape memory alloys in conventional composites gives us zero Gaussian curvature, with honeycomb core gives us an anticlastic or saddle shaped behavior corresponding to the negative Gaussian curvature, and with auxetic core gives a dome-like or synclastic bending behavior corresponding to the positive Gaussian curvature (refer Figure 1.13). Hence, we obtain the three major curvatures required to shape a torus. The proposed approach also helps in the active shape and vibration control of the embedded composite structures and allows process reversibility. In the next section, we discuss the fundamentals of the shape memory alloy and the state-of-the-art of the SMA embedded composites.

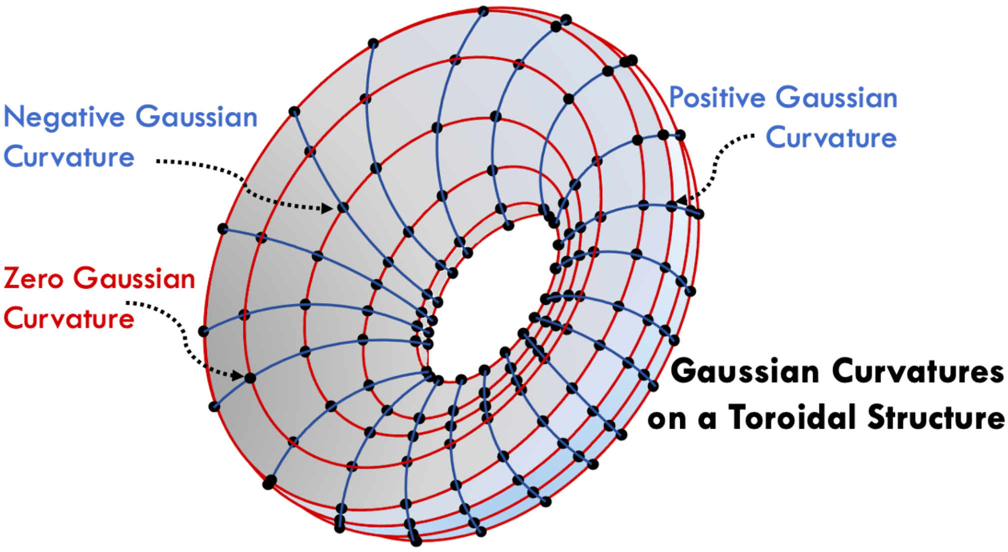

Figure 1.5: A toroidal structure is composed of postive, negative, and zero Gaussian curvature points causing spehrical, hyperboloidal, and cylindrical surfaces.

1.3 Shape Memory Alloys

Shape memory alloys are a unique class of metallic alloys that exhibit two very unique characteristics- thermal shape memory effect (SME) and superelasticity (or pseudoelasticity). SMAs can be copper-based, iron-based, and the most popular one is titanium-based. Upon thermal actuation the alloy transforms from its lower temperature martensite phase to its higher temperature austenite phase. During this process, it recovers the imparted strain and returns to its parent shape, thus '*remembering* its initial shape/dimension; this is called the Shape Memory Effect (SME). SME was first discovered in the Au-Cd (Gold-

Cadmium) alloy by Chang and Read (1951); however, the effect gained popularity after the discovery of SME in Nickel-Titanium alloys by Buehler et al. (1963), termed NiTiNOL (Naval Ordinance Lab), that demonstrated larger shape memory effect in comparison to other existing shape-memory materials. Not only a 100% recovery of up to 8% strain was observed, an over twice increase in Youngs modulus in the austenite phase in comparison with the martensite phase was also seen. Figure[2] 1.6 shows the qualitative stress-strain behavior of NiTiNOL and the effect of temperature variation on the same.

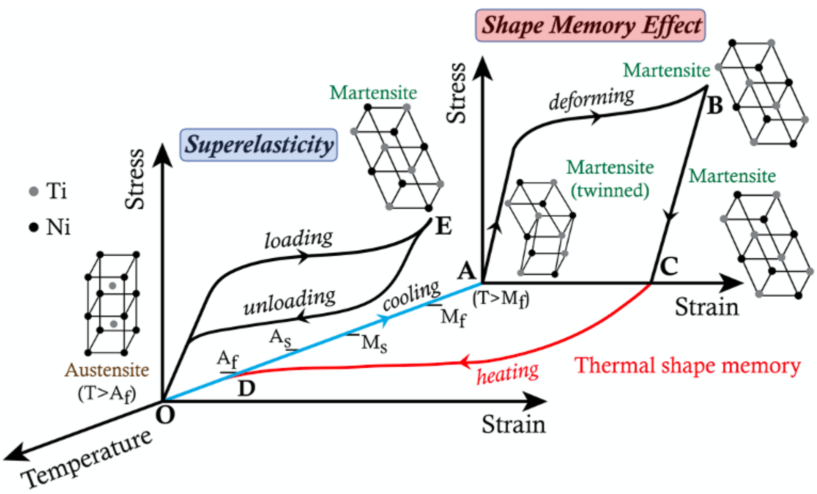

Figure 1.6: Stress-Strain-Temperature diagram of shape memory alloys showing Shape Memeory Effect and Superelasticity or Pseudoelasticity

The need for active control of mechanical properties and, consequently, the functional performance of a structure is continuously growing, giving rise to a new class of synthetic adaptive composites. With their superior characteristics like variable flexibility, they prove to be efficient in tailoring the static and dynamic responses of a system. These useful variations in responses have been previously achieved by controlling the ply layup, thickness, fiber volume-fraction, and fiber orientation of the composite. More recently, the advances in smart materials involve combining the benefits of heterogeneity of existing conventional composites with self-adapting characteristics of reinforcement elements, hence, conceiving a new domain of self-adaptive smart composites. Herein, we integrate smart materials, like Shape Memory Alloys (SMA), piezoelectric fibers, and magnetostrictive nano-particulates, into the composite through embedding/reinforcing, making the

[2]In Figure 1.6, M_f, M_s, A_s, and A_f denote the Martensite finish, Martensite start, Austenite start, and Austenite finish temperatures respectively.

composites functional for vibration attenuation, shape morphing, damage sensing, and self-healing. For instance, Bachmann et al. (2012) explore the enhancement of passive damping of carbon fiber-reinforced composite (CFRP) by embedding shunted piezoelectric material as well as SMA wires; Arrieta et al. (2013) explore a bi-stable wing-shaped model actuated using piezoelectric composites.

Another method to achieve structural control is through the reinforcement of SMA into the composite, bonding SMA to the top laminate or by embedding SMA wires in bonded sleeves, even in some cases integrating the structure with SMA springs. SMA integrated composites are especially suitable for applications that require large-deformation morphing as well as damping enhancement. Using SMA as an actuator/sensor, we utilize the phase change from martensite to Austenite and vice-versa through temperature or stress-induced transformation. While some applications utilize the shape memory effect, some use superelasticity and some of the recovery forces generated during the phase transformation. Examples of external SMA integration includes early work done by Loughlan et al. (2002), wherein composites consisting of continuous SMA actuators within sleeves, running along the neutral plane of the laminated plates, are analyzed for active buckling control; Machairas et al. (2018) reported fluid-structure interaction of an adaptive airfoil actuated using 1D SMA wires on a two-link adaptive mechanism. SMA wires embedded in ribs/sleeves attached to a pre-stressed elastomeric composite are also utilized more recently in morphing automotive fender skirts for drag reduction [Chillara et al. (2019)]. A unique category of SMA integrated carbon nanotubes (CNT) is explored by Fonseca et al. (2013), wherein the in-situ

Figure 1.7: The Reinvented Wheel by NASA for the Mars Rover consists of NiTiNOL mesh in austenite phase, thus able to bear large stresses without undergoing plastic deformation. This behavior is also called Pseudoelasticity.

polymerization and mechanical melt mixing techniques are employed for manufacturing shape memory polyurethanes(SMPU) integrated carbon nanotube (CNT) nanocomposites to attain shorter recovery time. Drive for the efficiency of SMA for medical applications have dominated the smart materials industry, successfully fabricating SMA based dentures [Miyazaki (1998)], SMA stents [Duerig et al. (1999)] and SMA based bone scaffolds by Bormann et al. (2013) for biocompatible load-bearing.

Especially with the advancement of soft robotics, SMA springs have gained more popularity due to larger displacement output compared to the SMA wires. Holschuh and Newman (2014) have reported low spring index SMA coils for their implementation in morphing aerospace systems. A combined bias spring-SMA wire actuator rotary manipulator, as well as a controlling technique for the same, have been proposed by Narayanan and Elahinia (2016), while an SMA bias-spring linear actuator model is presented by Thomas et al. (2019) for optimal dimensioning of the system to maximize the stroke of the actuator.

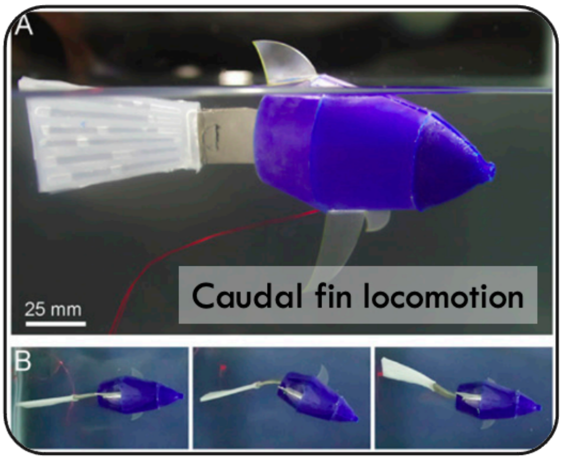

Figure 1.8: A thermally activated soft artificial muscle is actuated with embedded wires of NiTiNOL and used for caudal fin locomotion of a swimming robot [Bartlett et al. (2017)].

A study utilising SMA strips was done by Bartlett et al. (2017) involving the fabrication of SMA strips to function as bistable arches for wing chord morphing. SMA strip has also found its application in tunable resonators in nanotechnology application by Stachiv et al. (2017), where NiTi SMA film is sputtered on single-crystal silicon as the elastic substrate material. Another noteworthy research in the design of tunable metamaterial beam utilizes phase transformation to achieve a considerable shift in the elastic moduli of the resonators enabling active shifting of the bandgap over a temperature range [Candido de Sousa et al. (2018)].

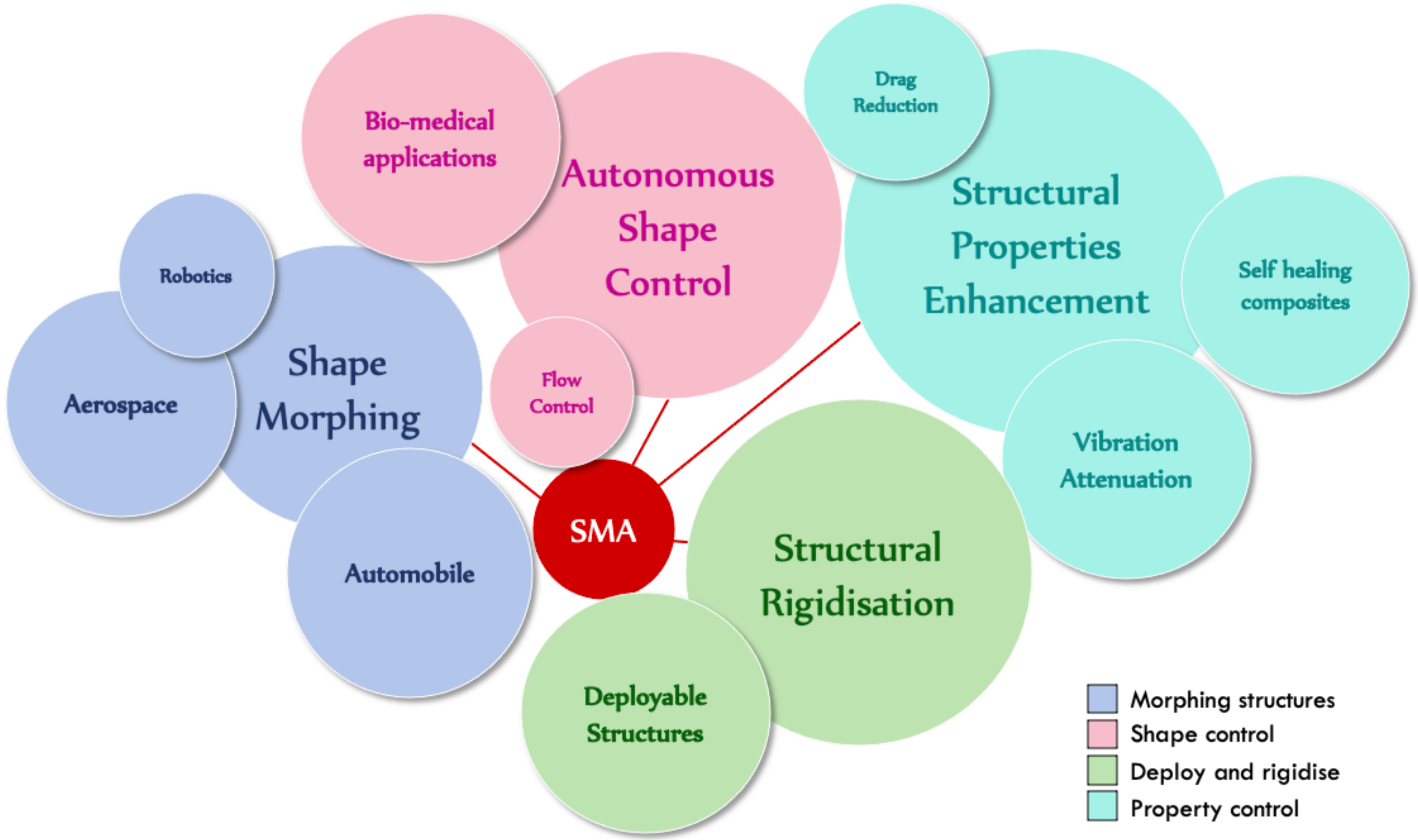

Figure 1.9: Application domain of Shape Memory Alloys. The Superelastic property finds more commercial applications as compared to the Thermal Shape Memory Effect.

The academic community has extensively explored SMA embedded fiber-reinforced composites (FRPs) [Cohades and Michaud (2018)]. Prior research substantiates the conjecture that embedded SMA in FRPs provides not only passive but also active damping of a structure, enhance the impact and buckling properties, allow shape morphing when embedded at an offset, and introduce self-healing bio-inspired processes [Meo et al. (2013), Tao et al. (2006), Bertagne et al. (2018), Lee et al. (2018)]. SMAs have also found their way into the textile industry, allowing morphing, self-fitting wearables [Ashir et al. (2019), Granberry et al. (2019)]. Khalili et al. (2013) present a non-linear finite element model for dynamic analysis of an SMA embedded composite plate embedded using a unified formulation. A combined smart composite comprising of shape memory polymer (SMP) and SMA wire is devised by Lelieveld et al. (2016) to achieve 90°bending deformation. A general outline of the application domain of the SMAs is summarised in Figure 1.9.

A substantial amount of research in this field can be summarised into two major categories: Active Property Tuning (APT) and Active Strain Energy Tuning (ASET) to modify the stiffness of the hybrid composite and for shape recovery purposes, respectively [Bhaskar et al. (2020)]. APT is a method of modifying the effective stiffness of the composite using SMA residual and high actuation stresses. Some work has been done by Hua et al. (2011), experimenting with the effective negative coefficient of thermal expansion (ECTE) of fibers like carbon fiber or Kevlar to attain structural stability over a given temperature range. A similar strategy which was earlier explored using the negative ECTE of SMA by Baz and Chen (1993) was utilised to improve the overall performance of drive shafts embedded with SMA. The shape morphing behaviour without compromising the structural stiffness is realised through the continuous embedding of SMA [Baz et al. (1990), Pfaeffle et al. (1993), Paine et al. (1995)] in polymer composites. Similarly, active and passive vibration control is also obtained through the strategic embedding of SMA in various composite structures [Schetky et al. (1994), Bidaux, J.-E. et al. (1995), Epps and Chandra (1997)]. For example, Lau (2002) investigate the frequency response of SMA embedded composites over a temperature range and introduce a theoretical model to capture this behavior. Damping is another reason for vibration control-based studies, Baburaj and Matsuzaki (1996) discuss their findings on numerical studies of specific damping capacity (SPC) of SMA laminated composite plates.

Apart from property tuning and shape morphing applications, SMA embedded composites are also used for damage suppression, self-healing, and health monitoring purposes. Kuang and Cantwell (2003) obtained localized SMA actuation detecting impact damage in CFRP, and Saeedi and Shokrieh (2017) experimentally studied the effect of pre-strained SMA on fracture behavior of the polymer at different temperatures and with varying SMA diameter. Similarly, SMA-based composites are also under a great deal of attention due to their self-healing characteristics. Kirkby et al. (2009), in their work, demonstrated this behaviour by combining microencapsulated liquid healing agent and SMA wires wherein the SMA is actuated to pull the crack together and bind it using the healing agent. In a more recent work by Karimi et al. (2019), the thermomechanical response of SMA is converted to traction-separation response, thus presenting a numerical model for self-healing behavior of SMA embedded composites. Finding the utility of SMA as a sensor has opened new doors of exploration in the field of structural health monitoring. Nagai and Oishi (2006) find a correlation between the strain in their composite and the variation of electrical resistance in the embedded SMA wire, thus estimating the material damage indirectly. Soon after this experimental work, Cui et al. (2010) proposed a mathematical model capturing the sensing function of the embedded SMA for structural health monitoring.

In our work, we majorly explore the Active Property Tuning through vibration response behavior of the SMAHCs and the Active Strain Energy Tuning through the shape morphing behavior of embedded pre-strained SMA wires. In the next section, we will discuss Auxetic structures, which are further explored in this thesis.

1.4 Auxetic Structures

Auxetic structures are solid structures with negative Poissons ratio (ν), which in practice implies that when the structure is stretched along one direction, it also expands along all the other directions. Similarly, the structure upon compression, instead of its usual behavior of expanding laterally, compresses [Figure 1.10]. Auxetic materials are of rapidly increasing interest because of their unique behavior upon loading and also due to the scope to tailor and enhance other material properties using auxeticity.

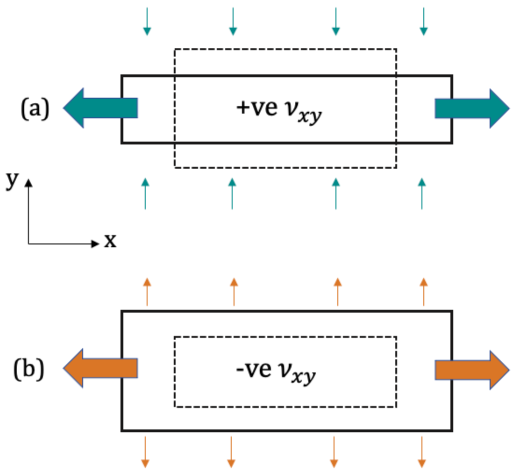

Figure 1.10: Schematic diagram of positive and negative Poisson's ratio upon tensile loading applied to an undeformed bar (dashed line) in the longitudinal (x) direction. a) Non-auxetic behavior- lateral contraction and longitudinal extension (solid line). b) Auxetic behavior- longitudinal as well as lateral extension (solid line).

One such example is the enhancement of indentation resistance. As we know, the indentation resistance of an isotropic material is proportional to its Poissons ratio and Youngs modulus by the formula- $[(1-\nu^2)/E]^{-1}$, assuming a uniform pressure distribution by the indentor Evans and Alderson (2000). From this, we can see that the indentation resistance of an auxetic material increases with increasing auxeticity or negative ν. Another example of improved material property behavior of auxetic materials over non-auxetic materials is the shear modulus. The shear modulus of an isotropic material is defined as $G = 3K(1-2\nu)/[1(1+\nu)]$, where K is the bulk modulus of the material. Given the extreme versatility of the auxetic materials, their domain of applications has been increasing continuously, from their use in smart wearables to reentrant honeycomb plies as a sandwich core in composites and structural applications.

Even though the major ongoing research in the field is on artificial auxetic materials and structures, there are some instances of auxeticity observed in naturally occurring materials such as single-crystal materials like arsenic [Gunton and Saunders (1972)] and cadmium [Li (1976)]. Negative Poissons ratio is theoretically permissible with an allowable range of -1.0 to +0.5 based on thermodynamic considerations of strain energy in the theory of elasticity. The existence of auxeticity in naturally occurring materials depends on the high degree of anisotropy and is dominated by the coupling between stretching and shear deformation. Since there is no law of conservation of volume, all auxetic materials obey the law of conservation of energy Lakes (1987).

Some work has been initiated towards combining the properties of SMAs with auxetic structures. Most of these works have been done in manufacturing auxetic structures from SMAs and studying their load-bearing capacity, stiffness tunability, deployability, and morphing qualities [Hassan et al. (2004), Hassan et al. (2008), Michailidis et al. (2009), Hassan et al. (2009), Rossiter et al. (2014), Neville et al. (2017), Kwon and Roh (2019)]. Limited work has been carried out demonstrating the behavior of SMA reinforced composite with honeycomb or reentrant-honeycomb (auxetic) core. Ghaznavi and Shariyat (2017) have developed an analytical model to determine the non-linear dynamic response of soft auxetic core sandwich plates with embedded SMA wires to generate active damping, which has given the foundation to the latter part of the work in this thesis.

1.5 Constitutive Modelling and Optmization

The literature surrounding the modeling of the shape memory alloys and auxetic structures is exponential in number; however, there are gaps explaining the behaviour of SMA embedded composites with honeycomb and reentrant honeycomb core. Some work done with SMA embedded composites and SMA embedded composites with auxetic core is discussed in Sections 1.3 and 1.4 respectively. One of the initial work done by Jia and Rogers (1989) gives a mathematical model for SMA embedded composites by incorporating the recovery force in the composite constitutive relation as a temperature-dependent resultant force. This method was further advanced by Turner et al. (1994) and the constitutive relations were defined for two separate temperature zones, when the temperature was below Austenite start temperature ($T < A_s$) and when above Austenite start temperature ($T > A_s$). These aforementioned works have formed the basis for the analysis of SMA embedded composites for both analytical and numerical methods. More recently, the study of SMA embedded composites has advanced to complex problems with impact loading, thin-walled composite shells, double curved sandwich panels, and under hygro-thermal loading.

The buckling and post-buckling responses of doubly curved SMA-based composites were carried out by Karimiasl et al. (2019) where the structure was under hygro-thermal loading. The shell considered here is assumed to be embedded in a distributed hygro-thermal load in the x-y plane. The SMA-based composite problem has also been solved through rigorous finite element analysis. In the buckling analysis done by Akbari and Khalili (2019), a UMAT subroutine is integrated with ABAQUS wherein the properties of the SMA fibers/wires are calculated using the Brinson (1993) model (discussed in Chapter 5). Apart from the loading conditions and method of solving the constitutive equations, plenty of work is done in analysing SMA-based composites of various shapes and sizes. From tapered to curved beam, to plate, and to shell, the growing utility of SMA-based composites has attracted a handsome amount of work in this emerging field. One such interesting study by Lin et al. (2020) presents an analytical model for the non-linear aeroelastic, flutter, and the random response of an SMA-based composite panel, wherein the structure is subjected to the thermal-aero-acoustic coupled field.

Given the immense engineering opportunities opened up by these composites, it became crucial to optimize the required applications structures. One of the earliest works in this domain was done by Schmit and Farshi (1973), where they used the inscribed hyper-spheres optimization algorithm to achieve minimum weight optimum design of laminated fiber composite plates, subject to multiple in-plane loading conditions. Using Genetic Algorithm (GA), Riche and Haftkat (1993) optimized the laminate stacking sequence for buckling load maximization considering the contiguity and strain constraints. Several optimization problems have been approached for adaptive composites and especially SMA-based composites and/or SMA actuation-based morphing structures. Haghdoust et al. (2017) optimized the shape profile of an SMA sheet in hybrid layered composite structures designed for passive attenuation of flexural vibrations. In another work byLeal et al. (2017), a continuous morphing aircraft wing is studied, and the design is optimized to obtain a Pareto frontier to simultaneously minimize cruise airfoil average camber and minimize shape difference between morphed outer mold line and the landing shape. In order to determine the optimal locations in truss structures, optimization techniques such as genetic algorithms (GAs) and simulated annealing (SA) have been used for the corrections of static deformations. Silva et al. (2004) used single objective binary-coded GAs and determined optimum voltages needed to apply to the piezoelectric actuators for achieving the desired shape.

1.6 Research Methodology and Organisation

As discussed in section 1.2, a novel method for the inflation/rigidisation of a toroidal structure is proposed in this dissertation, using a group of shape memory alloy reinforced composites. The earlier part of the thesis includes:

- Material characterisation of NiTiNOL, E-glass fiber, and Silicone matrix reinforced E-glass fiber.
- Design and fabrication of the single-layer SMA reinforced composite, and two-layered SMA reinforced composite.
- The experimental thermoelastic bending and vibration response analysis of the SMA composites.

Figure 1.11 gives a brief overview of Part I of the dissertation.

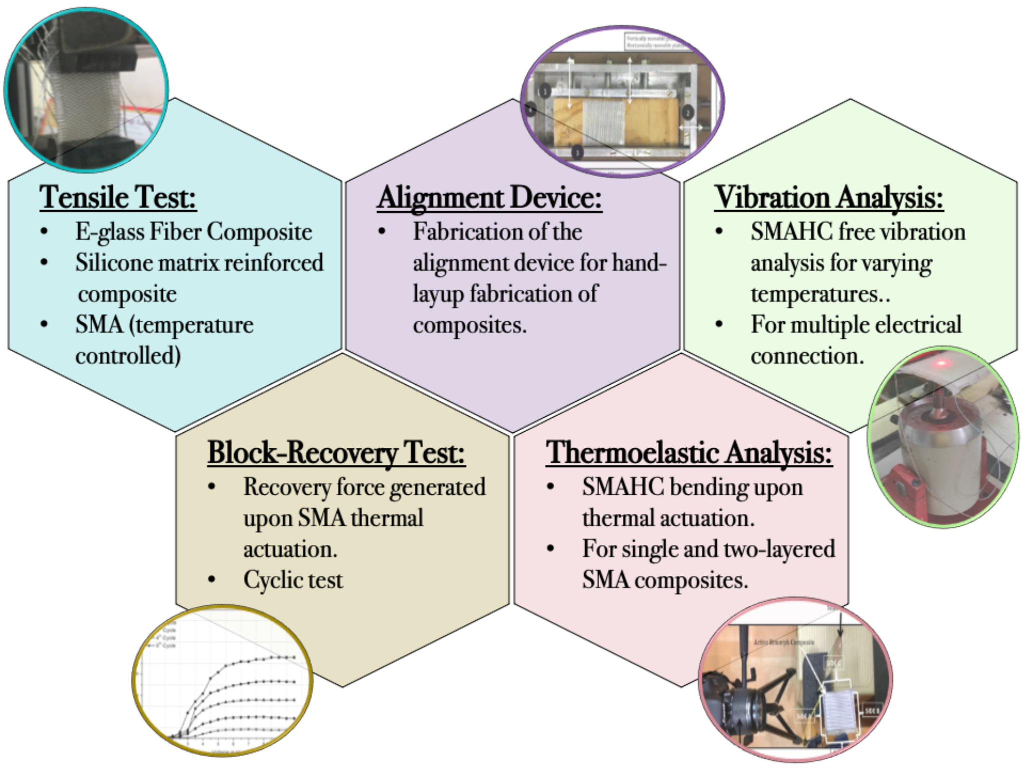

Figure 1.11: Summary of *'Part I: Experimental analysis of SMA embedded composites'*.

Once the material characterisation and the experimental analysis of the fabricated Shape Memory Alloy-reinforced Hybrid Composites (SMAHCs) is complete, we move to the numerical modeling of the same and validate the model. Hence, the middle part of the thesis comprises of:

- Mathematical model of the SMA reinforced group of composites as well as the SMA models such as Brinson [Brinson (1993)] and Turners Model [Turner (2000),Turner et al. (1994)].
- The numerical modeling of the single and two-layer SMA reinforced composite as well as the honeycomb and auxetic core SMA embedded composites.
- Parametric study of the change in SMA volume fraction on the bending and vibration response, and the effect of change in reentrant angle of the honeycomb and reentrant honeycomb core on the effective material properties of the core, thereby affecting the bending and vibration response.

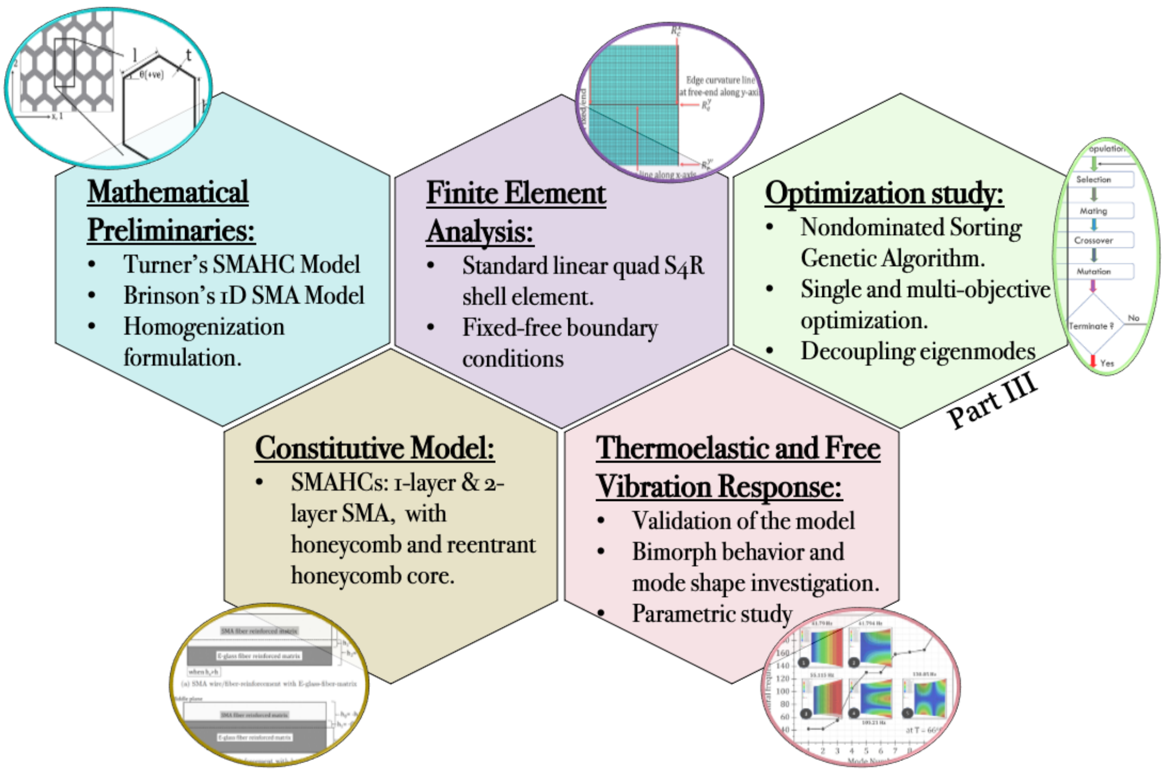

Figure 1.12: Summary of *'Part II: Numerical analysis of SMA embedded composites'*, and *'Part III: Structural Optmization of SMA embedded composites'*.

Finally, we present the multi-objective optimization study of the group of composites using the Non-dominated Sorting Genetic Algorithm (NSGA-II) [Deb et al. (2002)].

Figure 1.12 gives a graphical representation of Part II and Part III of the thesis.

1.7 Closure

Due to the existing issues with the inflation technology and a gap in successfully utilising it for space structures, as earlier discussed in this chapter, we explore the proposed method of ‘inflation and rigidisation using SMA embedded composites to obtain the three major Gaussian curvatures in a toroidal Gossamer structure. The main objectives of the thesis are:

1. Material characterisation of SMA and parameter identification to be used as an input in the numerical study.

2. To understand the thermoelastic and vibration response of the unimorph and bimorph SMA composites and to establish a proof-of-concept for the proposed idea.

3. Extend the work to obtain the essential negative and positive Gaussian curvatures to complete the requirement of the proposal.

4. Optimize the problem to discard structures that do not satisfy the precondition and drive the focus on the feasible and realizable structures.

In the present thesis, the SMAHCs are employed for the purpose of obtaining various Gaussian curvatures of the torus, as shown in Figure 1.13. The single-layer SMAHC gives a zero Gaussian curvature upon thermal actuation of SMA (embedded at an offset) by Joule heating, the SMAHC with honeycomb core gives a negative Gaussian curvature or anticlastic/saddle-shape, and the SMAHC with reentrant-honeycomb or auxetic core gives a positive Gaussian curvature or synclastic/dome-shape behavior. Hence, combining the three elements will help us form a complete toroidal structure after SMA actuated deployment and rigidisation.

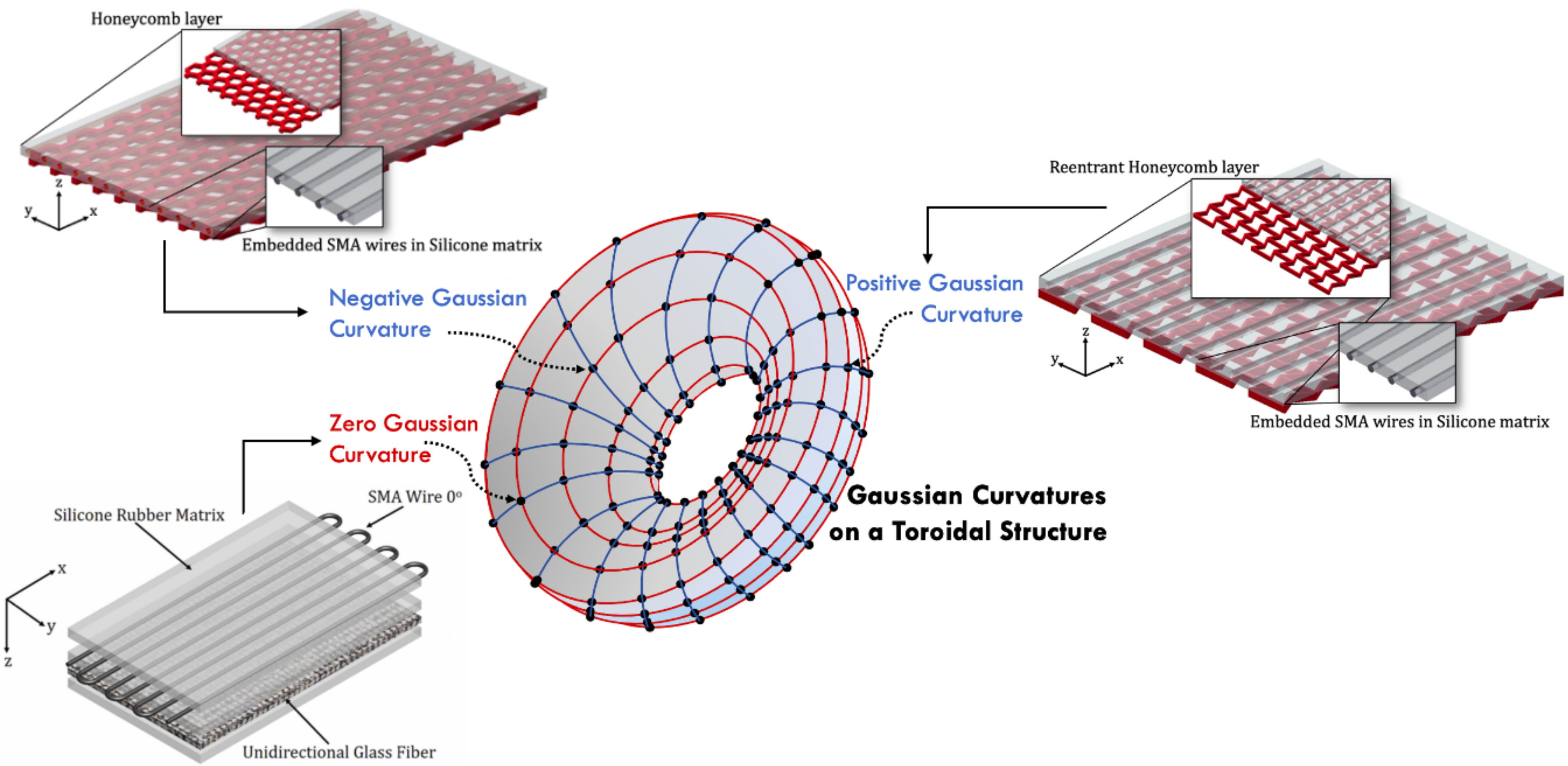

Figure 1.13: SMA reinforced single layered, honeycomb, and reentrant honeycomb core composites to obtain the three Gaussian curvatures of a toroidal structure- zero, negative, and positive respectively.

Part I- Experimental analysis of Unimorph and Bimorph SMA Hybrid Composites (SMAHCs)

Chapter 2

Mechanical Testing and Material Characterisation

This chapter explores the material properties of the shape memory alloy and the composite constituents- E-glass fiber and Silicone matrix. We find the Elastic modulus of the SMA through temperature-controlled tensile testing and the recovery force through block recovery test. SMA wires used in this study were procured from Dynalloy Inc. Since Dynalloy had limited SMA wire properties data, we carried out material characterisation aligning to the Turners Effective Coefficient of Thermal Expansion (ECTE) model. The characterisation based on other material models is beyond the scope of this work, hence, not included in the material characterisation.

2.1 Parameters required for the ECTE Model

In order to construct Turners Effective Coefficient of Thermal Expansion Model for SMA embedded composites, we only require two fundamental temperature-dependent material properties of SMA: 1) Recovery Stress and 2) Youngs Modulus. In the following subsections, we will discuss the experimental setup we employ in this study to obtain the temperature-dependent properties of SMA as well as the other composite constituents.

2.1.1 Block Recovery Test [σ_r]

With the help of National Aerospace Laboratories(NAL), Bangalore, we conducted the Block Recovery Test of the NiTiNOL HT375 wire. A prestrain (initial strain) of 4.5% was set in the wire before conducting the block recovery test. It has been reported by Turner (2000) that with an increase in prestrain and mechanical constraint, the Austenite finish temperature[1], A_f, also increases which were further observed during the experiment. In other words, a higher temperature was required for completely recovering the strain.

The SMA wire was constrained in the crossheads of the tensile testing machine allowing no deformation. Next, the voltage across the wire was increased using a voltage amplifier from 0 V to 10 V with increments of 0.5 V and at each interval, the reading of the load cell was noted down. After 10V is reached, the amplifier was turned off, and the crossheads of the tensile testing machine were calibrated for the load cell zero reading. The tests were repeated for cyclic analysis and with varying gauge lengths of 50mm and 100mm. At this point, we observed that with an increase in prestrain and mechanical constraint, the Austenite finish temperature kept moving further. We use the obtained data to calculate the ECTE, α, from Turners model, discussed in Chapter 5. Figure 2.2b shows the ECTE vs. temperature data, wherein complete phase transformation was observed at 66°C.

2.1.2 Temperature controlled Tensile test [E_a]

The elastic or Youngs modulus (E_a) of shape memory alloys is a function of temperature as the alloy transforms from its martensite phase to Austenite phase upon thermal actuation, Youngs modulus increases. Hence, a temperature-controlled tensile test is required to obtain the varying modulus of elasticity of the SMA. Since the phase transformation was observed at 66°C, Figure 2.2b shows the change in elastic modulus in the defined temperature range.

[1] The temperature at which the alloy has transformed completely from its martensite (or R-phase) to its Austenite phase upon heating. At and beyond this temperature, the alloy has zero martensite volume fraction and is purely Austenitetenite.

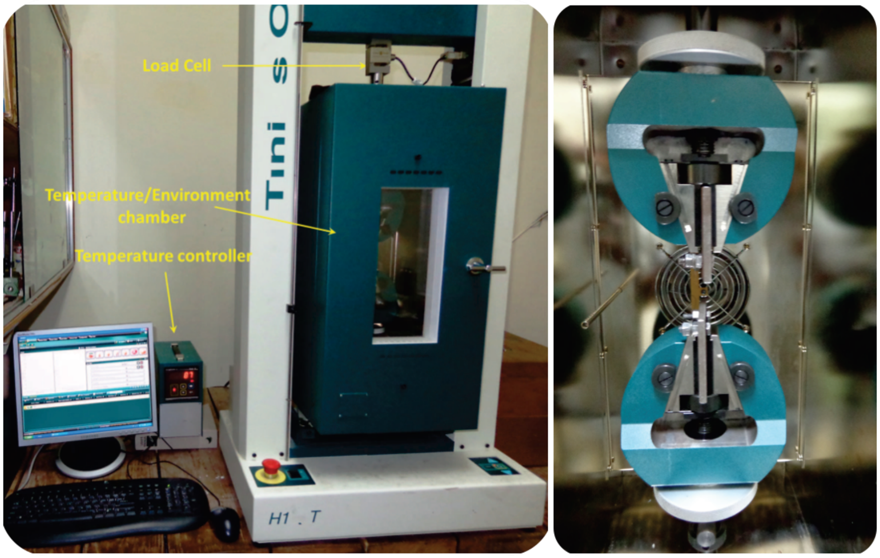

Figure 2.1: Tensile testing machine used for conducting temperature controlled stress-strain analysis (left), and inside view of the temperature chamber showing grippers holding a fixture mounted with NiTiNOL HT375 wire (right).

Tensile tests were conducted in a controllable environment in the Tinius Olsen machine, as shown in Figure 2.1, with a temperature controlling chamber with a capacity of 10KN load cell. The data from the machine is extracted via an integrated computer that records the readings [Figure 2.2a]. As per the Standard Test Methods for Tension Testing of Metallic Materials E8/E8M-11, the area of the material within its gage length could not be reduced, which can cause the gripping forces to affect the test. To avoid this, a pair of simple fixtures were fabricated to tighten the wire and then fixed in the crossheads, thus reducing the influence of screw tightening loads on tensile test results.

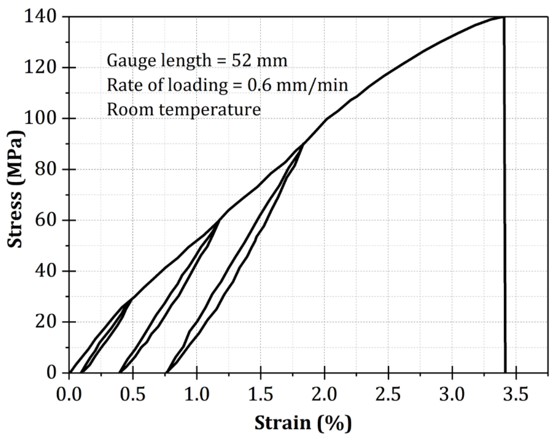

(a) Stress-strain curve of HT375 SMA wire, at 30°C

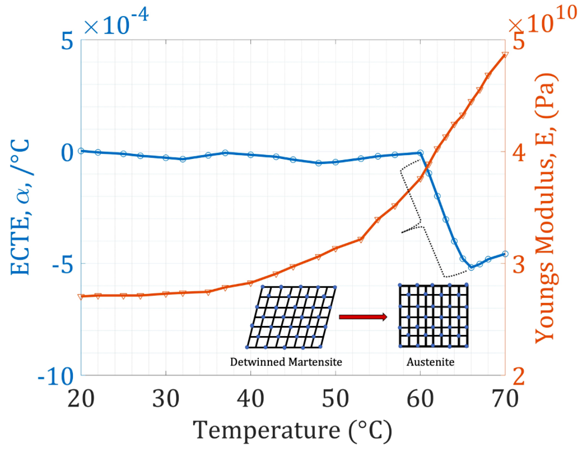

(b) Experimental data for temperature dependent effective coefficient of thermal expansion and Youngs modulus of SMA.

Figure 2.2: Experimental data requierd for Turner's Model. The sudden drop in the graph at 66°C is attributed to the phase transformation from Martensite to Austenite

The loading rate was 0.6 mm/min, and the heating rate of the temperature chamber was 9°C/min. At room temperature, the specimen was loaded up to 30 N and unloaded to 0 N. In the 2nd cycle, the specimen was loaded to 60 N, and in the third cycle, it was loaded to 90 N before unloading. Finally, the specimen was loaded till failure, which was found to be at 140 N, as shown in Figure 2.2a. The same set of steps were repeated for varying temperatures. In Figure 2.2 we can see the cyclic loading-unloading data for SMA at room temperature and the temperature dependant Youngs modulus. The recovery stress and Youngs modulus values were obtained at discrete temperature points and solved for ECTE[2] through numerical differentiation (refer to Chapter 5). Here, T corresponds to temperature, α to ECTE, and E_a is the temperature-dependent Youngs Modulus of the SMA.

[2]The following equation from Turners model (Turner (2000)) is employed to calculate the effective coefficient of thermal expansion for NiTiNOL. The discrete values of the recovery stress data are solved using the *cumtrapz* function in Matlab to get the ECTE curve as shown in Figure 2.2b:

$$\sigma_r = -E_a \int_{T_0}^{T} \alpha_{1a}(\tau) d\tau \tag{2.1}$$

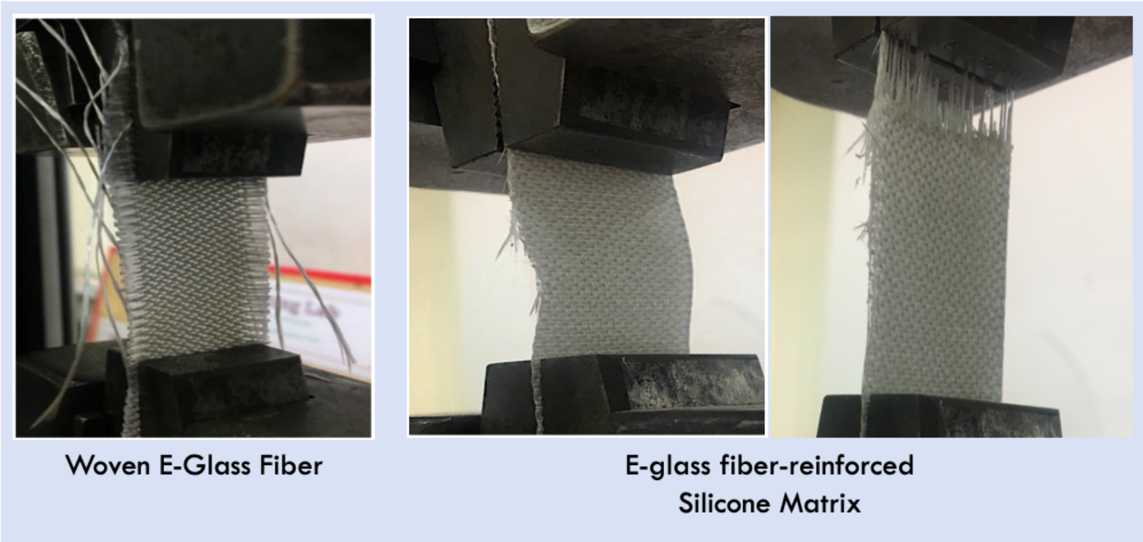

Figure 2.3: Woven E-glass fiber (left) and E-glass fiber-reinforced Silicone matrix (right) constrained in the Instron 1195 Universal Testing Machine. In the case of Silicone matrix reinforced with glass fibers, the matrix is yielding and deforming plastically while the fibers are continuing to stretch elastically.

2.2 Composite Mechanical Properties

To obtain the material properties of the woven E-glass fiber and its composite with silicone laminate, a uniaxial tensile test was carried out on the Instron 1195 Universal Testing Machine. The bi-axially woven E-glass fiber sample was of an area of $23.34mm^2$, and loaded axially at a strain rate of $2mm/min$ at room temperature, as shown in Figure 2.3. The same test was carried out for a silicone laminated woven E-glass fiber specimen of $25mm^2$ area and at a strain rate of $5mm/min$. The strain rate was increased considering the tensile properties of silicone. The results for the latter are compared against the non-laminated fiber in the same Figure 2.4.

Initially, the glass fiber specimen is tested, attaining the peak stress of 10.71 MPa. This is followed by subjecting the silicone laminated woven E-glass fiber to the tensile test achieving peak stress of 28.38 MPa. Thus there has been about 165% increase in peak stress capability as shown in Figure 2.4. This is due to the fact that the matrix is yielding and deforming plastically while the fibers are continuing to stretch elastically since the yield strength of the matrix is significantly lower than the tensile strength of the fiber.

Since there is always considerable variation in the fracture strength of brittle fiber materials, all fibers do not fracture simultaneously. Additionally, even after fiber failure, the matrix still remains intact, and the fractured fibers, which are shorter than the non-fractured ones, are still embedded inside the intact matrix and are hence capable of sustaining a diminished load as the matrix continues to deform plastically. In the Silicone laminated E-glass fiber composite, the volume fraction of glass fiber in the composite, V_f, is 0.35, whereas for the matrix, V_m, is silicone, is 0.65. Since the sample was vacuum degassed hence it is assumed that there are no voids. The results of the test are tabulated in Table 2.1.

Parameter	E-glass fiber	Composite (E-glass fiber with silicone matrix)
Peak stress (MPa)	10.71	28.38
Peak load (kN)	0.25	0.71
Yield load (kN)	0.203	0.321

Table 2.1: Mechanical testing results for the woven E-glass fiber and E-glass fiber reinforced silicone matrix

Material Property	**Silicone rubber Dragon Skin 20**
Young's Modulus (kPa)	3.38×10^2
Poisson's ratio	0.49
Coefficient of Thermal Expansion (10^{-6}/°C)	250
Density (kg/m^3)	1081.25
Service temperature range (°C)	-53 to +232
Curing temperature	Room temperature (23°C)
Cure time (hrs)	4
Specific gravity (gm/cm^3)	1.08
Specific volume (cm^3/gm)	0.925
Tensile strength (MPa)	3.8
Material Property	**E-Glass fiber (Woven)**
Young's Modulus (kPa)	72×10^6
Poisson's Ratio	0.21
Coefficient of Thermal Expansion (10^{-6}/°C)	4.9
Density (kg/m^3)	2600
Variety	13 MIL fiber glass fabric
Type of weave	4-H Satin
Thickness (mm)	0.35
Width (mm)	150
Construction	Warp: 48 threads/inch Weft: 32 threads/inch
Weight per sq. mtr. (gms)	442.5
Breaking strength per 50mm	Warp: 336 kgs Weft: 242 kgs
Material Property	**SMA wire**
SMA Diameter	$300\mu m$
Resistance (Ω/m)	12.2
Recommended Pull Force (N)	12.55

Table 2.2: Manufacturer provided material properties of E-glass fiber (Azo Materials, Asia), Silicone rubber (Dragon Skin^{TM} 30, Smooth-On, Pennsylvania, USA), and NiTiNOL wire (Dynalloy Inc.)

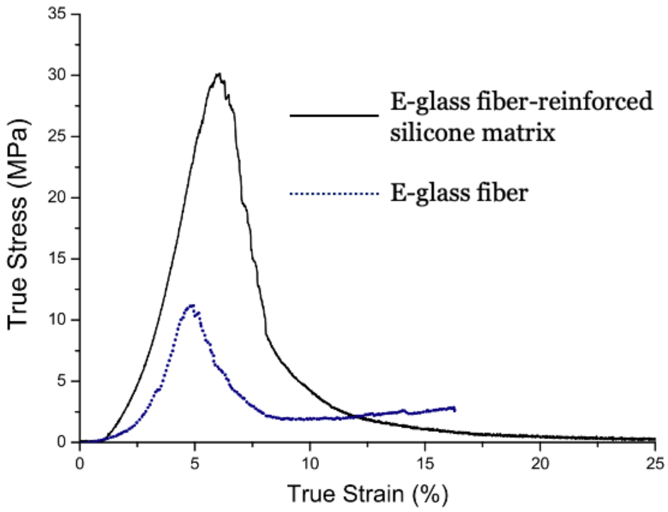

Figure 2.4: True stress-strain curves for woven E-Glass fiber and Silicone laminated E-glass fiber. A 165% increase in peak stress capability is observed.

The properties of the E-glass fiber and the Silicone rubber used in the simulation are specified in Table 2.2. The E-glass fiber was procured from Azo Materials, Asia, and the Silicone rubber, Dragon Skin^{TM} 30, from Smooth-On, Pennsylvania, USA. Using these properties, we compute the equivalent orthotropic properties of the lamina. The requirements to define the behaviour of a composite are- volume fraction of the fiber (V_f), volume fraction of the matrix (V_m), Youngs Modulus of the fiber (E_f) and the matrix (E_m), Poissons ratio of both fiber(ν_f) and matrix (ν_m), density ρ_f and ρ_m, and finally, the coefficient of thermal expansion α_f and α_m. We assume that through vacuum degassing, any voids created due to air entrapment are removed.

2.3 Summary

In this chapter, we have summarised all the necessary characterisation of NiTiNOL, a shape memory alloy used for rigidisation of flexible structures. The obtained experimental values were used to calculate the negative ECTE of SMA required for the modeling of the SMAHC using Turners model. Since the material properties of SMA are temperature dependent hence, the block recovery and the tensile test were carried out in a temperature-controlled environment. Next, the tensile tests of the woven E-glass fiber composite and the woven E-glass fiber-reinforced silicone matrix are carried out on the Instron 1195 UTM. In the case of laminated composite, the fracture fibers remained embedded in the plastically deforming silicone matrix, thus providing a diminished strength to the composite. The material characterisation in this chapter forms the essential foundation for all the analyses that follow in this thesis. The interesting behavior of fiber-reinforced silicone and the sudden drop in the coefficient of thermal expansion upon phase transformation of SMA are the characteristic finds of this chapter. In the coming chapters, we will use these experimental values to calculate the effective longitudinal and transverse composite properties using the rule-of-mixtures and Halpin-Tsai formulations. Further, we will also discuss other related mathematical preliminaries required for the mathematical formulation and numerical modeling of the same.

Chapter 3

Thermoelastic Response Analysis

Overview

For the evaluation of zero and negative Gaussian curvatures of the inflatable toroidal structure, we fabricate two SMA embedded E-glass fiber-Room Temperature Vulcanising (RTV) Silicone Rubber Silicone matrix composites- (1) single layer SMA fiber-reinforced hybrid composite (unimorph SMAHC), and (2) a two-layer (cross-ply) SMA fiber-reinforced hybrid composite (bimorph SMAHC). In this chapter, we report the fabrication and analysis of these active composite structures by evaluating the variation of the curvature and the tip-displacement of the top fiber layer with respect to the change in applied voltage to the SMA embedded at an offset. The composite showing the bi-directional bending behaviour was fabricated by embedding NiTiNOL Shape Memory Alloy wires in two layers, at 0°and 90°orthogonally. The study of the deflection[1] motion of the SMAHCs shows that with an increase in temperature of the SMA wire, the bending curvature initially increases almost proportionally and finally reaches a constant steady

[1]Schematic illustration describing the deflection principle of the SMAHC:

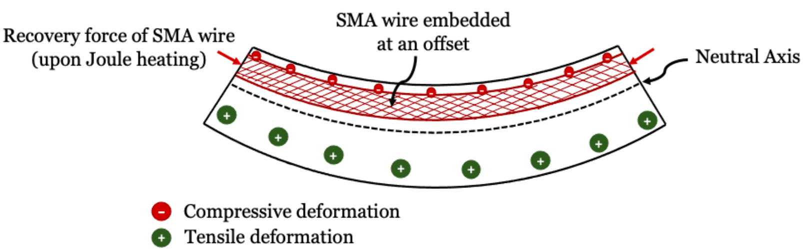

curvature, and the experimental results satisfy this condition. The second layer of the active bimorph structure (ABS) system when actuated gives the composite a bi-directional bending behaviour. The analysis was done using a single-point laser sensor in the case of single-layer SMAHC and through image processing in the case of two-layer SMAHC.

3.1 Specimen Fabrication

An alignment frame device made of aluminium as shown in Figure 3.1 was designed using AutoCAD, a Computer-Aided Designing (CAD) software, and fabricated to ensure that during the curing of the composite, the wires stayed straight, aligned longitudinally, with the desired spacing between them. The design consists of an enclosure with movable plates inside to grip and strain the wires. This novel design is capable of embedding NiTiNOL wires bidirectionally and orthogonally in separate layers of a composite. The CAD model was submitted in the Central Workshop of the institute for its fabrication from aluminum plates. The plates were cut using water-jet, and holes of recommended sizes were drilled, followed by thread cutting. Finally, the entire model was assembled as shown in Figure 3.2.

The wire is kept between the vertically movable (and detachable) plates and fixed. Then the horizontal slider plates are pulled back until the wire is taut and their motion is constrained. M4 bolts are used for this purpose, and the thread length and grip length are different in both directions and chosen to maintain the movable distance without interference. A sample with a maximum dimension of 185mmx60mm can be fabricated using this fixture; however, the size can be reduced by moving the adjustable plates. Since the wire procured from the manufacturer was already pre-strained hence no memory training was required.

For the first sample, as shown in Figure 3.3(a) of the glass-silicone host, one ply of multi-axial fiber orientation (weave) E-glass fiber was laminated with silicone. The sample was of the dimension of 60.61mm x 54.77mm x 1mm. The SMA wires were placed at a distance of 3mm from each other on the top of the sample, strained using the moving plates of the fixture. The straining is done to keep the wires taut, and it is made sure that no further stretching is imparted to the pre-strained wire as discussed in Chapter

2 the straining affects the Austenite finish temperature. The SMA wire is 1m in length embedded continuously in a digitated pattern.

The fixture with the sample was then placed in a vacuum degassing chamber and left to cure for four hours at room temperature. No external load was applied during the curing process, and the sample was cured under the vacuum pressure of 30mmHg. The final thickness obtained was 1.04mm. The manufacture provided material properties of SMA wire, silicone, and glass fiber are collated in Table 2.2. The same procedure was then followed for the sample with two layers of SMA wire reinforcements. The SMA wire embedded 3mm apart in this sample was of 300μm diameter. The ply configuration for this sample was [SMA 0^0/E Glass/SMA 90^0/E Glass] in silicone matrix as shown in Figure 3.3(b). The sample, when removed from the vacuum degassing chamber, was cleaned of extra silicone rubber displaced due to high degassing pressure. Finally, the loose ends of the wire were cleaned and crimped to the wire connecting it to a 30V-2A DC supply. The sample dimensions for the sample with two layers of SMA wire reinforcement were 62.28mm x 60.64mm x 2.24mm.

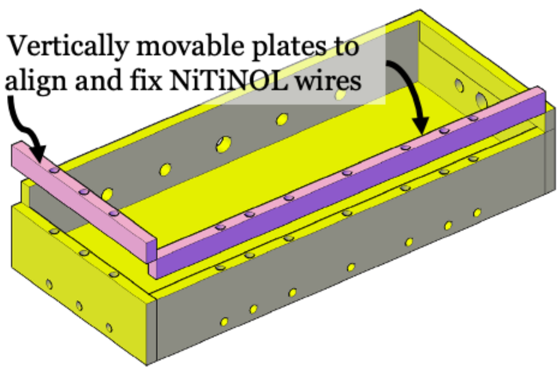

Isometric view of the CAD model of the alignment frame.

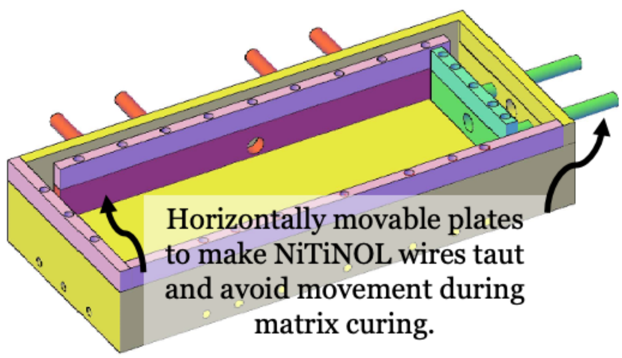

Figure 3.1: Computer-Aided Design (CAD) model of the alignment frame device for the manufacturing of the unidirectionally and bidirectionally embedded NiTiNOL wires in soft composites. A set of vertically and horizontally movable plates are used to fix, align, and make the wires taut during the hand lay-up manufacturing of the SMAHCs.

Figure 3.2: Manufacture fixture/alignment frame for the SMAHC fabrication. Top view (a) of fixture with embedded composite and front view (b) of fixture. The fixtures has two horizontally movable and four vertically movable and detachable plates for the constraining of the SMA wires.

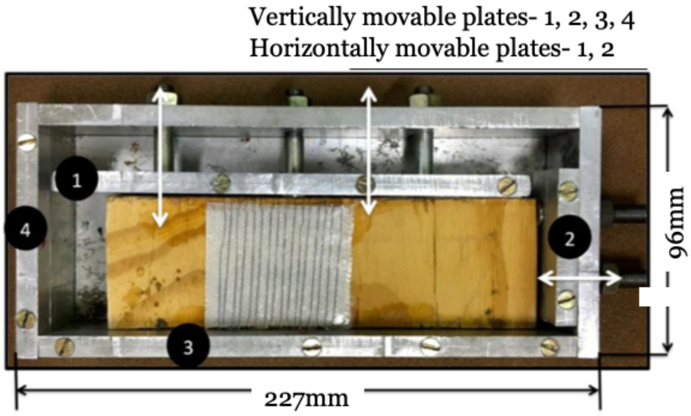

(a) Top view of fixture with embedded composite

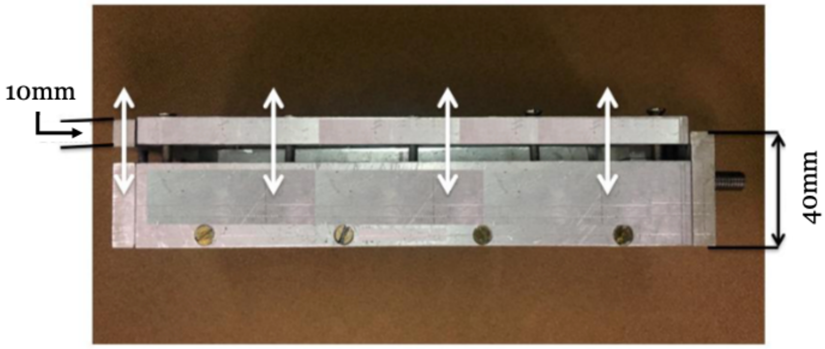

(b) Front view of fixture

The entire setup to measure the voltage dependency of deflection of the sample is shown in Figure 3.4. The sample was fixed on one side, and a single point laser displacement sensor ILD1420 was focussed at the center of the sample tip to measure the vertical displacement. The ILD1420 from Micro-Epsilon is a high measurement accuracy triangulation sensor with measuring rates of up to 4kHz. The Active Surface Compensation (ASC) characteristic confirms stable measurement results independent of the effects of surface colors or brightness, thus giving an intelligent surface regulation attribute. Its optical system generates a tiny light spot which enables it to detect small components accurately. It has a 500mm range and comes with a RS422 interface. The voltage data from the DC supply was acquired using a single channel from dSpace CLP1103 and saved using its inbuilt software dSpace Control Desk. The data acquisition of the sensor output was done from its inbuilt software. A voltage splitter was used before sending the data directly into dSpace and V_{in} was calculated[2] from the recorded V_{out}.

Four tests for the same sample were done, and the averaged result showed a linear relationship between the voltage increase and the deflection obtained. The tests were repeated for each set of five to prevent miscalculation and enhance the sensitivity of the results. The results obtained from these experiments are discussed in the next section. The same test was again conducted afterward, and through image processing (as shown in Figure 3.5), the maximum deflection of the composite tip was calculated, which came to be the same as obtained from the single-point-laser sensor data.

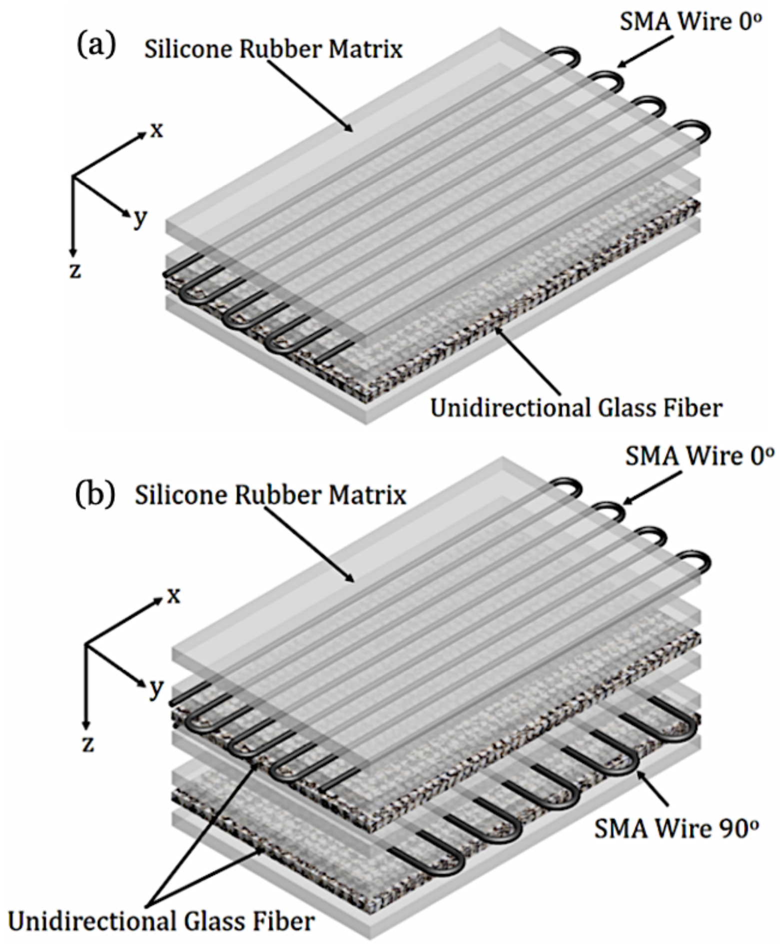

Figure 3.3: Schematic diagram of single-layer [(a)] and two-layer [(b)] SMAHC. The NiTiNOL wires are embedded in a digitated pattern and actuated through Joule heating. The offset embedding causes the composite bending upon SMA thermal actuation (thereby its contraction).

[2] $V_{out} = (\frac{R_1}{R_1+R_2})V_{in}$

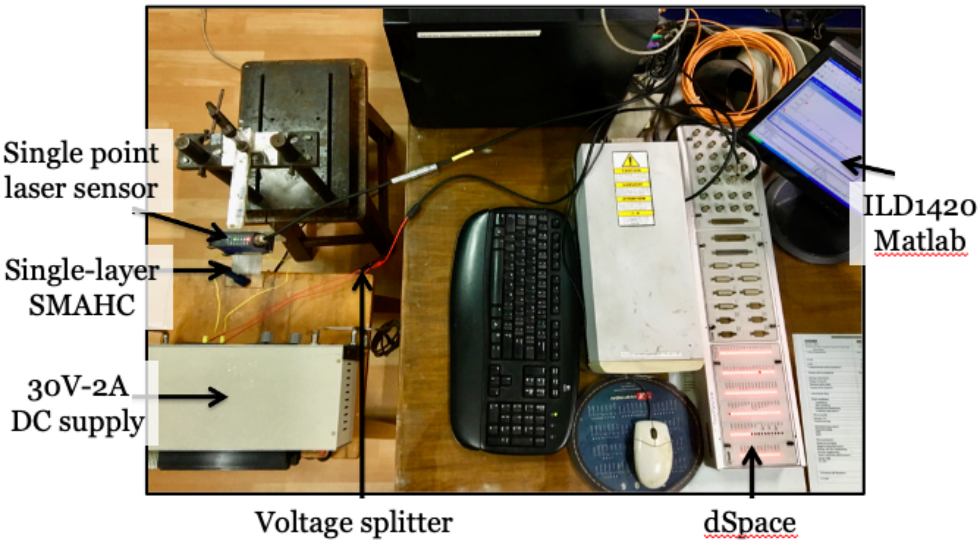

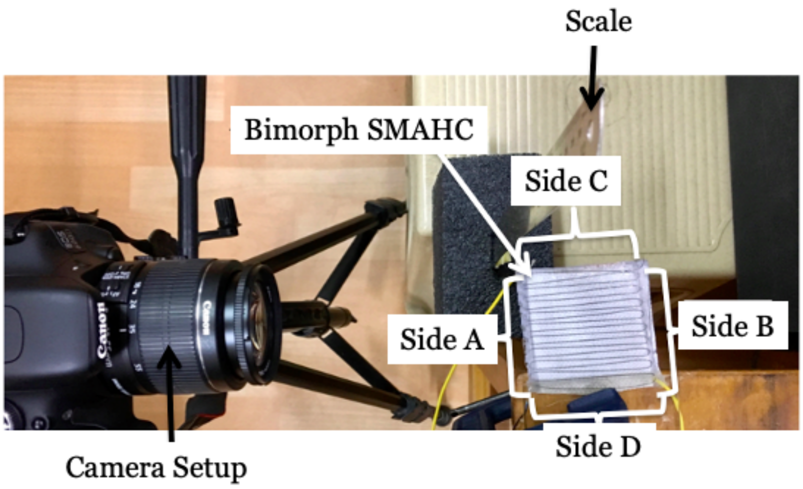

Figure 3.4: Experimental setup for the thermoelastic response analysis of the single-layer SMAHC (left), and two-layer bimorph SMAHC (right). The deflection of single-layer SMAHC upon SMA thermal actuation by Joule heating was observed using a sinle point laser sensor, whereas for the bimorph SMAHC was investugated through image processing method.

Wire Diameter(μm)	250	300	375
Resistance(Ω/m)	18.5	12.2	8.3
Recommended Pull Force (N)	8.74	12.55	22.06

Table 3.1: Flexinol HT90 SMA Wire properties for 1m wire with 3-5% deformation

We next conducted the tests on a silicone-glass composite embedded with two layers of SMA wires as shown in Figure 3.3. On giving current to either of the SMA layer, the composite showed a bidirectional bending but with a different amount of deflection depending on which layer was actuated. To understand this behaviour, we used image processing, capturing images from the three free sides of the sample at a time for fixed voltage points. The sample was fixed on one side perpendicular to the orientation of the wire, which was being actuated.

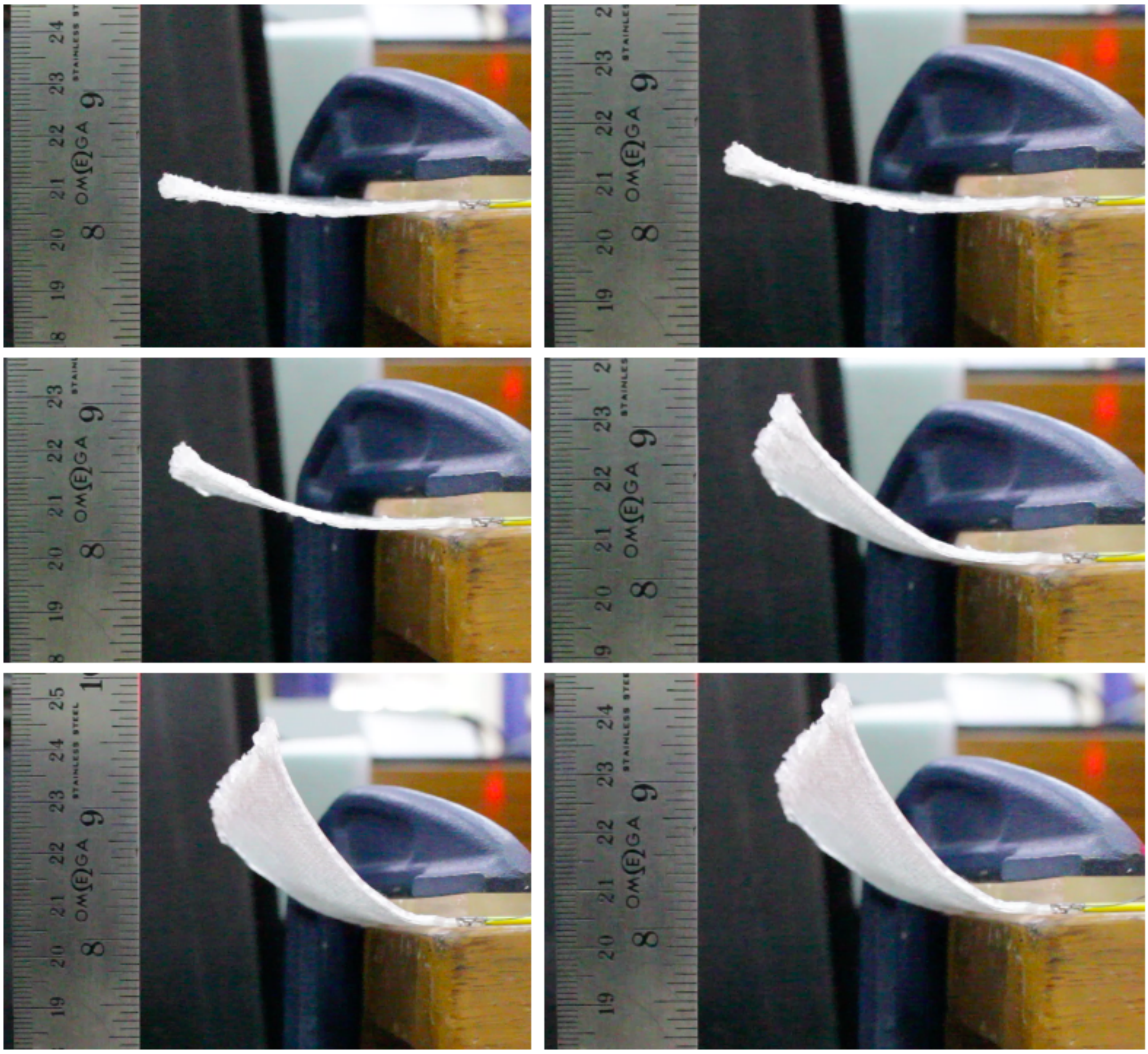

Figure 3.5: Deflection profile of single layer SMA composite. Since the SMA wire is embedded at an offset, its thermal actuation by Joule heating causes the composite to bend. As SMA contracts, the compression and tensile forces at either end of the thickness cause the bending. The SMAHC goes from the initial position with no deflection(a) to a maximum of 45mm (f) (average) deflection.

The experiment was set up as shown in Figure 3.4, where the images were captured from side[3] A, B, and C when the second layer of embedded SMA was actuated, and side D was fixed; also from the side B, C, and D when the first layer of embedded SMA was actuated and side A was fixed. Due to the bi-directional bending of the sample, it was not possible to record this behaviour using one or multiple single-point-laser sensors as the data was inconsistent; the results obtained through image processing are discussed in the next section.

3.2 Results and Discussion

3.2.1 Single layer SMA embedded smart composite

E-glass/silicone beam with low flexural rigidity was expected to show substantially high deflection. Due to this fact, it was expected to also give a curvature hence forming a half-cylindrical shape. An averaged deflection summary of all the tests is shown in Figure 3.6. Figure 3.6a shows a typical tip-deflection time curve and the voltage-time curve for the sample with single layer SMA wire. A reverse phase transformation was complete in 25-28 seconds, and the maximum deflection obtained was an average of 45mm. The cooling was allowed to happen naturally at room temperature. Since the service temperature range of the silicone used as matrix is -53^0C to $+232^0C$ hence, the actuation of wire at 90^0C did not affect the properties of the material. The shortest duration for the sample to achieve an asymptote was around 21s. The voltage (V) and sample tip displacement (d) relation is shown in Figure 3.6b and an equation defining the relation is obtained by fitting the experimental data using the polynomial curve-fit in the Matlab curve fit app plug-in. The equation corresponding to the deflection (in mm) behavior with respect to

[3]Schematic showing the details of the sides along the longitudinal and transverse direction:

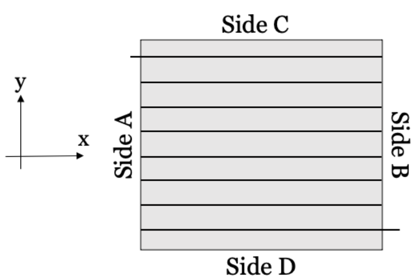

increasing temperature (as shown in Figure 3.6b), and $\frac{1}{5}$ curvature is found as:

$$d = 0.089122 + 1.74709V + 0.09419V^2 - 0.02985V^3 + 0.00197V^4 \tag{3.1}$$

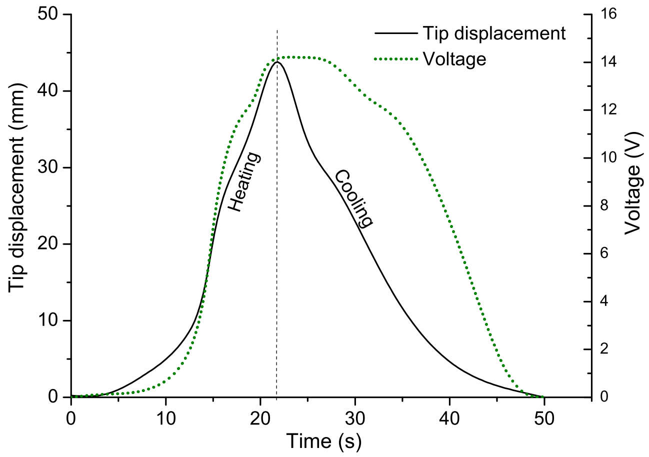

(a) End tip deflection of single-layer SMAHC upon SMA Joule heating.

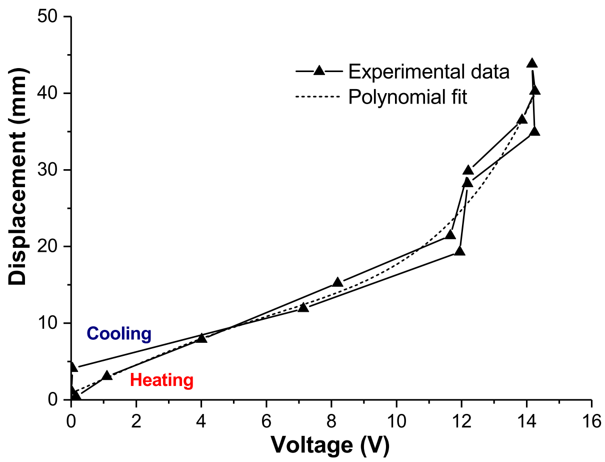

(b) Single-layer SMAHC deflection with respect to voltage.

Figure 3.6: Top fiber tip deflection of single-layer SMA embedded composite. A maximum curvature obtained was 0.2 corresponding to 14V and an average of 45mm deflection was observed in this case. A residual displacement of 5mm was observed in the composite upon return with no external cooling caused due to the stiffness of the E-glass fiber.

The voltage was increased linearly with two pauses at 12V and 14.3V. These pauses were to verify the possibility of shape control in future work by controlling the voltage source and hence the current flow. The displacement shows a linear behaviour with respect to voltage variation. An average of 4mm of residual displacement of the tip is observed and is caused due to factors as sample rigidity, deformation of sample due to heating and wire-composite debonding after multiple test cycles. Figure 3.7 shows the results obtained from the image processing of the same sample. A set of pre-defined points were marked along the edge of the sample and were tracked on the images in Matlab to measure their displacements with respect to their initial position at multiple voltage points. A total of 5 different tip deflections of the sample were recorded, and a maximum of 45mm of tip deflection was observed, which matched the results obtained from the single-point laser sensor. The maximum voltage to which the wires were actuated was 14V, at which the sample would maintain a constant deflection and curvature. The curvature calculated for maximum deflection along x-direction comes out to be $\frac{1}{5}$ corresponding to 14V.

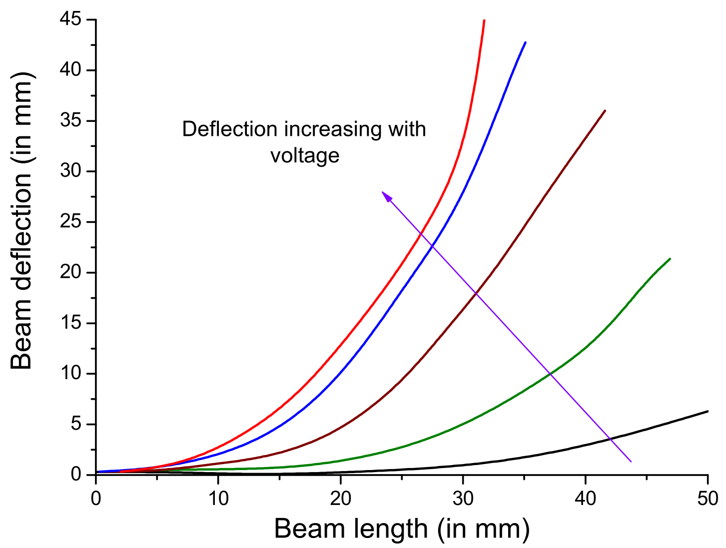

Figure 3.7: Beam deflection profile with increasing volatge for single-layer SMA reinforcement.

3.2.2 Two layers SMA embedded smart composite

The experimental setup for capturing the deflection behaviour of the sample shown in Figure 3.4 is discussed in the previous section. The images were taken for seven different voltages when the first layer of embedded SMA wire was actuated and for eight different voltages when the second layer of embedded SMA wire was actuated in the composite. The final value was chosen upon observing that the deflection and curvature of the sample were constant and did not change thereafter.

Material	Thermal Conductivity (W/m-K)
NiTiNOL (Austenite Phase)	18
Silicone rubber matrix	2.55
E-glass fiber	1.35

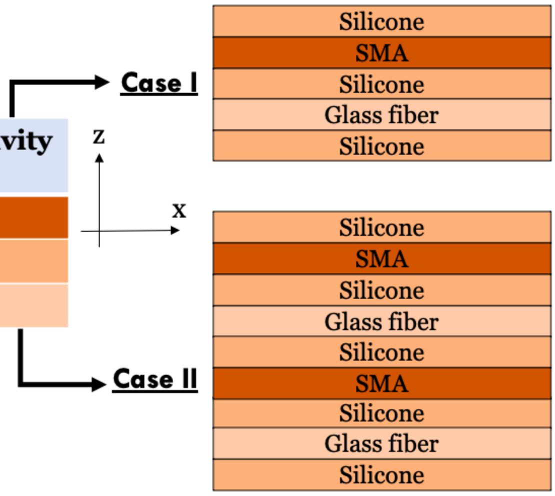

Figure 3.8: Schematic showing the thermal conductivities of the constituents materials. In Case II, when the top SMA ply is actuated, the heat is dissipated along the z-direction. This leads to losing heat to the surroundings, and the second SMA ply is not actuated. However, when the second ply is actuated, the trapped heat actuates the first SMA ply as well. Since the SMA wires are embedded orthogonally, the motion is highly constrained, and hence a diminished bimorph behavior is obtained.

The behaviour of the bi-directional SMA wire reinforced composite was interesting since actuating the first layer of embedded SMA wire, which is laminated on the top and could dissipate heat to the surroundings, led to lesser heat reaching the second layer of embedded SMA wire, whereas when the second layer of embedded SMA wire was actuated more heat was dissipated towards the first layer, it being embedded between glass fibers on both sides and unable to dissipate heat to the surrounding (as shown in Figure 3.8). This cause led to the behaviour change of the composite depending upon which layer of embedded SMA was actuated. The sample showed a considerable bidirectional bending and curving when the second layer of embedded SMA was actuated, hence Figure 3.10(f) is of importance to us.

Figures 3.10(a) , 3.10(b), and 3.10(c) , show the top fiber tip deflection of the composite when the first layer of embedded SMA is actuated and the result is captured from side B, C, and D respectively (refer Figure 3.4). The trend of this result is very similar to the results obtained from the first sample consisting of single-layer embedded SMA. On side B a maximum of 22.7mm of deflection was observed, whereas on side D it is reduced to 20mm, which is caused due to partial excitation of the second layer of embedded SMA and hence pulling down of top fiber tip on side D in the process. But since the deflection is only of 2.7mm hence the bi-directional behaviour observed in this case was not very significant.

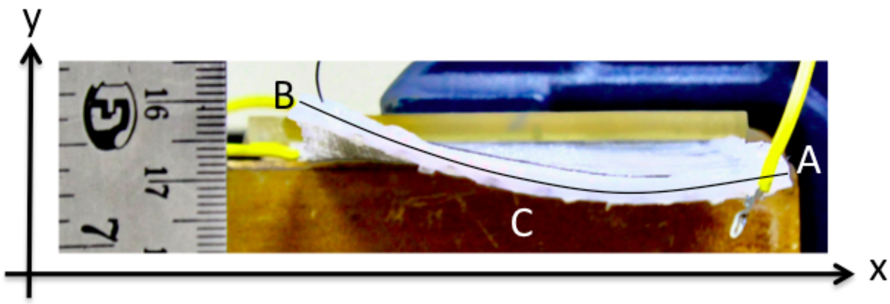

Figure 3.9: Bidirectional bending of the two-layer active bimorph SMAHC

Figures 3.10(d) , 3.10(e) , and 3.10(f) give the top fiber tip deflection of the composite when the second layer of embedded SMA in the composite is actuated. As we can observe in Figure 3.10(d) the maximum tip deflection obtained is of negative value, -8.8mm (in the negative x-direction) when recorded from side A, but interestingly as the current flow increases leading to an increase in the temperature of the embedded SMA wire the deflection starts in the opposite direction due to the activation of the first layer of embedded SMA wire as well. The final deflection observed is 3.3mm in the opposite direction.

Figure 3.10(f) shows this bidirectional behaviour clearly, where the top fiber tip on side A shows a deflection in negative x-direction whereas the top fiber tip on side B shows a deflection in the positive x-direction. This is caused due to bending of the top layer upon actuation of the first layer of embedded SMA as shown in Figure 3.9. Hence the sample is first curved about its x-axis and then about the z-axis giving us an Active Bimorph Composite Structure.

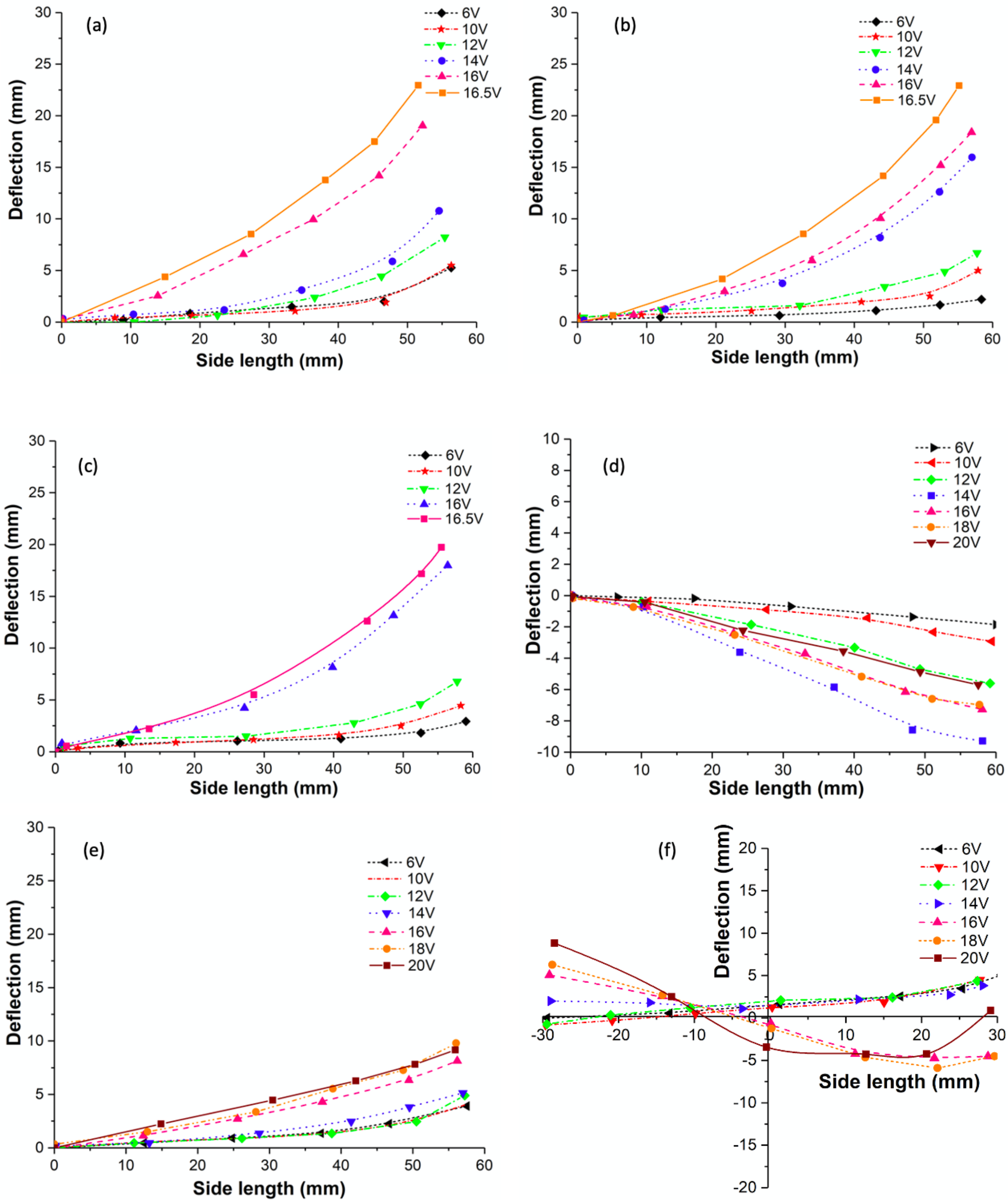

Figure 3.10: Deflection profile of Active Bimorph Composite with two layers of SMA reinforcement. (a) First layer (actuated) side B (image processing data), (b) First layer side C, (c) First layer side D, (d) Second layer side A, (e) Second layer side B, and (f) Second layer side C.

3.3 Summary

The fabrication and the thermoelastic behaviour of single-layer SMAHC and two-layer SMAHC active bimorphs are discussed in this chapter. The results of unidirectional and bidirectional bending have been observed and recorded. The zero Gaussian curvature was conveniently obtained from the active composite; however, the bidirectional bending behavior shows considerably less bimorph behavior; hence, the negative Gaussian curvature obtained is of a small value. The voltage control of the SMAHCs verifies the shape control possibility of the active composites, thus allowing us a defined control over the deployment and rigidisation of the toroidal element. The limitations of this structure are in the continuous and optimum requirement of current based on varying resistance of the wire, multi-layer insulation for space applications. Due to this reason, from the design and commercialisation perspective of the SMAHCs, cyclic deployment and regidisation are not suggested, and the proposed SMAHCs are suggested for single-time use. In this chapter, we present the idea of bidirectional bending of SMA embedded composite. The utilisation of orthogonal SMA embedding has not been explored for bimorph shape control yet in the literature. Hence, this novel work provides a proof-of-concept for SMA embedded smart bimorph composites. In the next chapter, we analyse the effect of change in voltage or the SMA wire temperature on the natural frequency of the structure. We will also investigate the effect of the electrical connection of the two-layer SMAHC's SMA wires on the natural frequency of the system.

Chapter 4

Free Vibration Response Analysis

Overview

The control of stiffness and hence the dynamic response of deployable structures can also be achieved through smart material-based actuation mechanisms such as the proposed SMAHCs. Selection of appropriate smart material hinges on the requirements of the speed of actuation, actuator bandwidth, and force requirement. This chapter presents the study of the vibration modes of the bimorph SMAHC with controlled current input. The SMAHC consists of two layers of SMA reinforcements with 0°and 90°orientation angles placed orthogonally in alternate plies. The temperatures of these layers are raised through Joule heating, first individually and then followed by combined actuation, where the current supply is controlled using a programmable DC supply. As the material properties of SMA are temperature dependent, we observe thermal contraction and a resulting increase in laminate stiffness. The change of compliance at multiple step-input currents contributes to variation in the natural frequency, which is recorded using a 3D laser Doppler vibrometer (LDV). This study gives us a deep insight into the application of SMA-based bimorph composites for active damping and vibration control subject to varying temperatures.

4.1 Experimental setup

The experimental setup for the modal analysis of the bimorph SMAHC (Case II) is schematically illustrated in Figure 4.1. The specimen was excited using the pseudorandom signal due to its high signal-to-noise ratio, controlled frequency content, and short test measurement time. The excitation signal was transferred to the function generator (PCI-6111) and then to the power amplifier (PA25E-CE, BRUEL & KJAER). This signal is then passed into the electromagnetic shaker (LDS-V201) for vibration actuation of the bimorph SMAHC. The shaft tip of the shaker is attached to a force transducer (11- Honeywell) to minimize interference and have a point excitation unidirectionally. The force transducer is glued to the SMAHC so that there is minimum loss of the input signal due to leakage. The dynamic response is then captured by the 3D-Laser Doppler Vibrometer (LDV- PSV-400, Polytec).

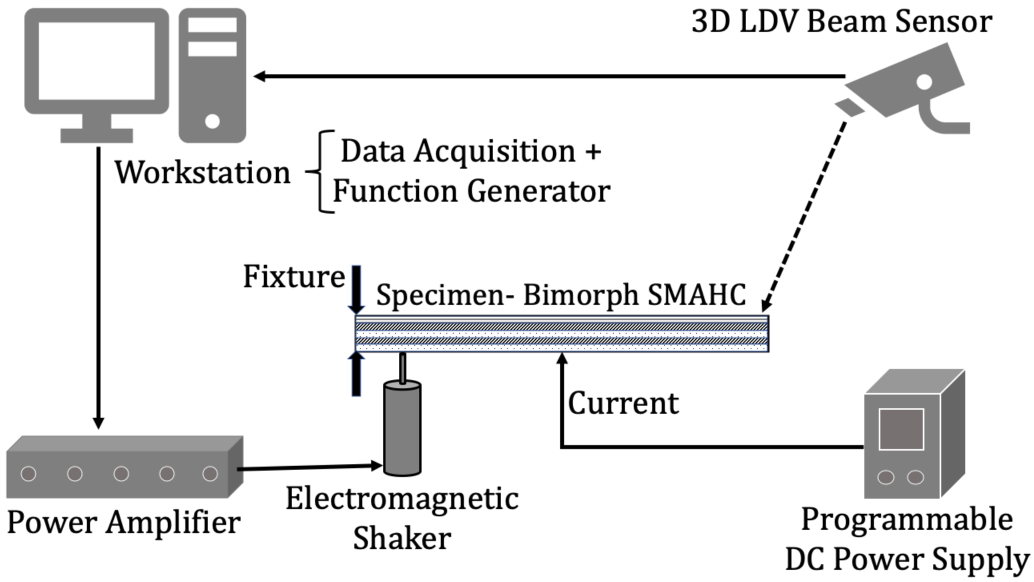

Figure 4.1: Block diagram for bimorph SMAHC modal analysis along with the actuation setup and sensing mechanism.

LDV is used for vibration measurement and works on the principle of the Doppler effect and interferometry. It detects the frequency change of the light scattered back from a vibrating object. It sends a monochromatic Helium-Neon laser beam of wavelength 633nm towards the target and receives the reflected beam. According to the Doppler effect, the change in the observed wavelength of the received beam is dependent on the relative velocity of the targeted object. Then, using the formula $\Delta f/f = v/c$, we calculate the velocity of the vibrating surface. Here, f is the frequency of the beam incident on the surface, Δf is the observed change in reflected frequency, c is the speed of light, and v is the velocity of the vibrating surface which can now be calculated. Using the velocity

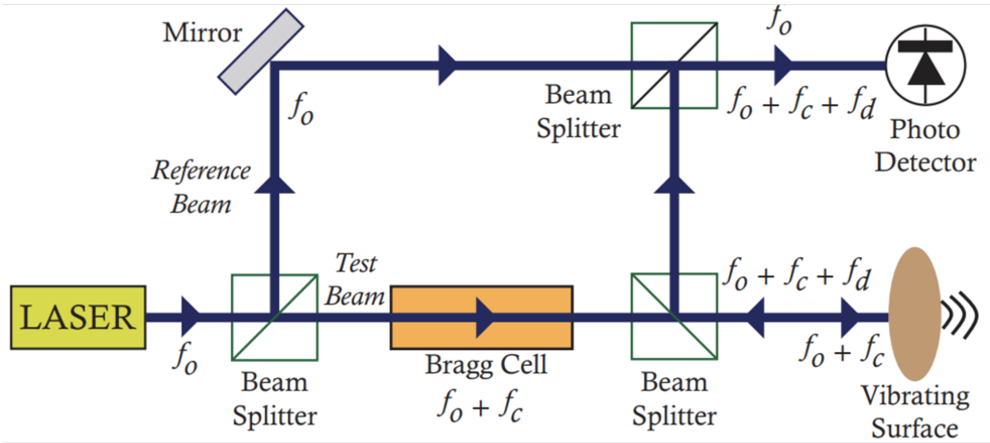

Figure 4.2: Schematic of basic components of LDV scanning head. Source-Wikipedia Public Domain- no copyright image.

and the wavelength ($v = f.\lambda$) of the beam, we calculate the frequency of the specimen. A beam splitter splits the initial laser beam of frequency f_o into a test and reference beam. The test beam passes via the Bragg cell that utilizes the acoustic-optic modulation effect to diffract and provide the required high-frequency carrier signals ($f_c > f_o$). Next, the frequency-shifted beam ($f_c + f_o$) is incident on a pulsating surface, adding a Doppler shift to the beam that can be expressed as:

$$f_d = 2v(t)cos(\beta) = \lambda \tag{4.1}$$

where, v(t): vibrating surface velocity as a time-function; β: angle between the laser beam and the velocity direction; and λ: wavelength of the laser beam. After hitting the target location, the light gets scattered in all directions, which allows the LDV to collect a portion of it, and the beam splitter directs the same to a photodetector. This frequency of light ($f_o + f_b + f_d$) interferes with f_o- the reference beam, in the photo-detector. When the path difference is an integral multiple of the beam wavelength, constructive interference happens, and when the path difference is an odd multiplier of $\lambda = 2$, destructive interference occurs. Hence, the motion of the vibrating surface generates a dark-bright fringe pattern on the detector signifying the displacement of the test location as exactly half the laser wavelength. The signal is demodulated to obtain the variation in velocity with time.

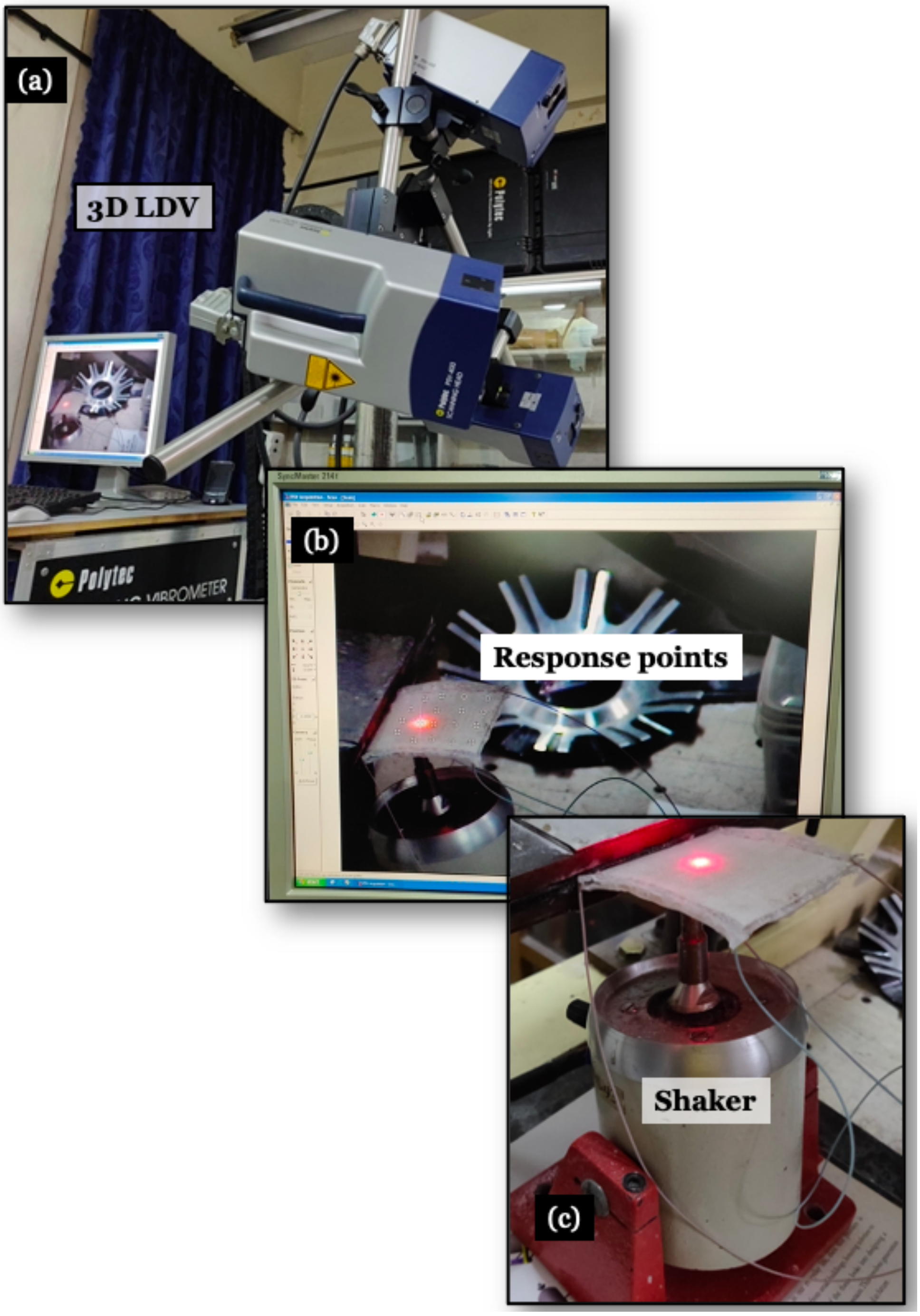

Figure 4.3: Experimental setup- (a) 3D Laser Doppler Vibrometer, (b) LDV software showing the assigned response points, (c) Bimorph SMAHC specimen placed horizontally on the electromagnetic shaker, and the incident laser beam.

A fine layer of developer is sprayed over the top surface of the bimorph SMAHC to reflect the laser beam incident at the predefined response points. The aligned 3D LDV, the selected multiple response points in the LDV software, and the specimen-shaker setup are shown in Figure 4.3. Finally, the specimen is connected to a programmable DC supply (PSW 80-27, GWINSTEK), with a maximum 80V - 20A supply of voltage and current, respectively. A step-function is defined and generated in .cvs format and supplied to the programmable DC through USB input.

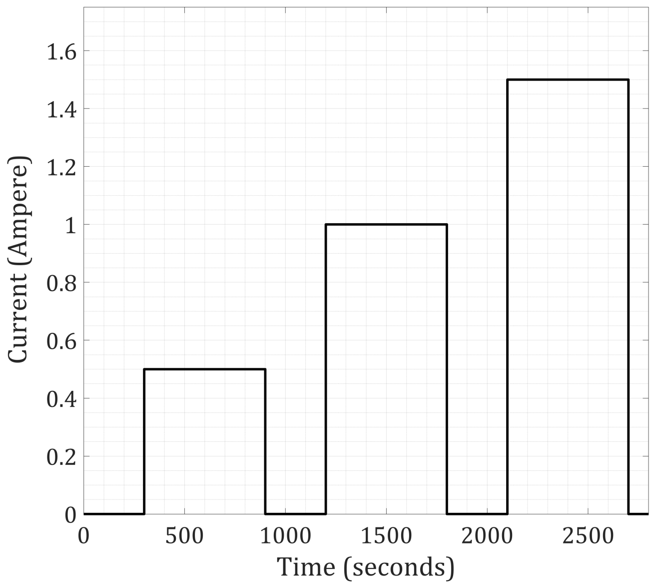

Figure 4.4: Current input function generated using the programmable DC supply.

The results were recorded by thermally actuating the SMA layers through Joule heating, separately and individually, and then together. The cases for which the natural frequency of the bimorph is recorded are (1) thermal actuation of SMA layer with 0°fiber orientation angle, (2) thermal actuation of SMA layer with 90°fiber orientation angle, (3) thermal actuation of both the SMA layers when SMA wires are connected through series connection, (4) thermal actuation of both the SMA layers when SMA wires are connected through parallel connection.

4.2 Results and Discussion

The natural frequencies for the cases as shown in Figure 4.5 are recorded and discussed in this section. We consider the aforementioned four cases for the analysis of the natural frequency of our bimorph SMAHC. All the cases are, however actuated using the same current input function.

Figure 4.4 shows the variation of input current with respect to time. The highs in the graph indicate the actuation cycle or the heating cycle of the SMA wire, while the lows indicate the cooling cycle. The heating of the embedded SMA wires causes contraction in the wire due to its characteristic negative coefficient of thermal expansion.

This contraction, in turn, bends the composite with it when its motion is restricted since it is placed at an offset, which causes bending of the composite. The purpose of cooling is to bring the composite back to its initial position. The processed data from LDV is taken at the constant current line, and the total time duration for each case is 50 minutes.

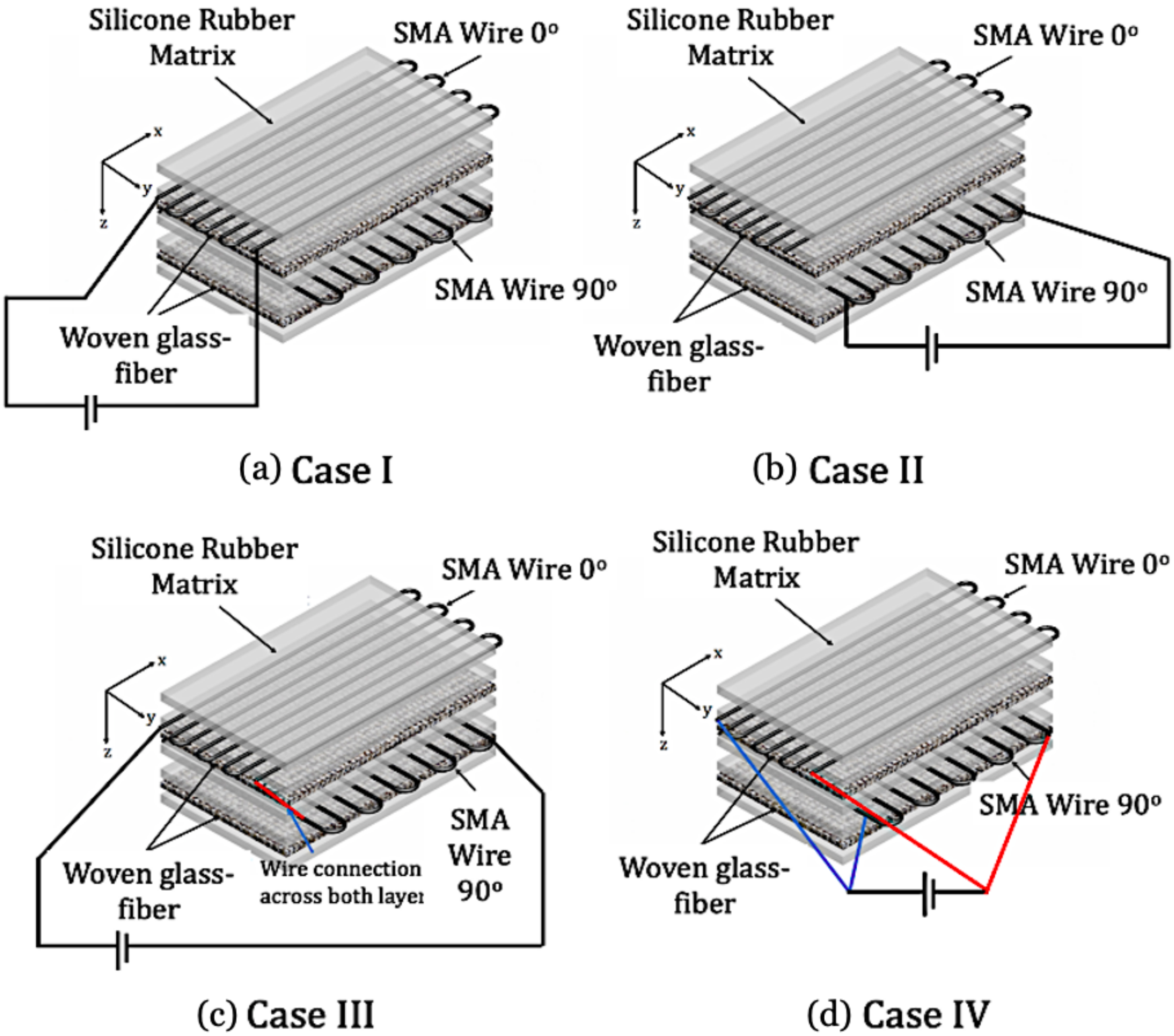

Figure 4.5: Schematic of SMA layer actuation cases: thermal actuation of- (I) SMA layer with 0°fiber orientation angle, (II) SMA layer with 90°fiber orientation angle, (III) both the SMA layers when SMA wires are connected through series connection, and (IV) both the SMA layers when SMA wires are connected through parallel connection.

Figure 3.9 shows the maximum bimorph bending of the specimen observed experimentally when the SMA wires embedded at 90° are actuated and maintained at the current corresponding to maximum deflection, which was recorded as 1.5A. A more detailed analysis of the deflection behavior and the deflection-temperature relation for both a unimorph and a bimorph has been discussed in Chapter 3.

4.2.1 Case I: Thermal actuation of SMA layer with 0°orientation angle

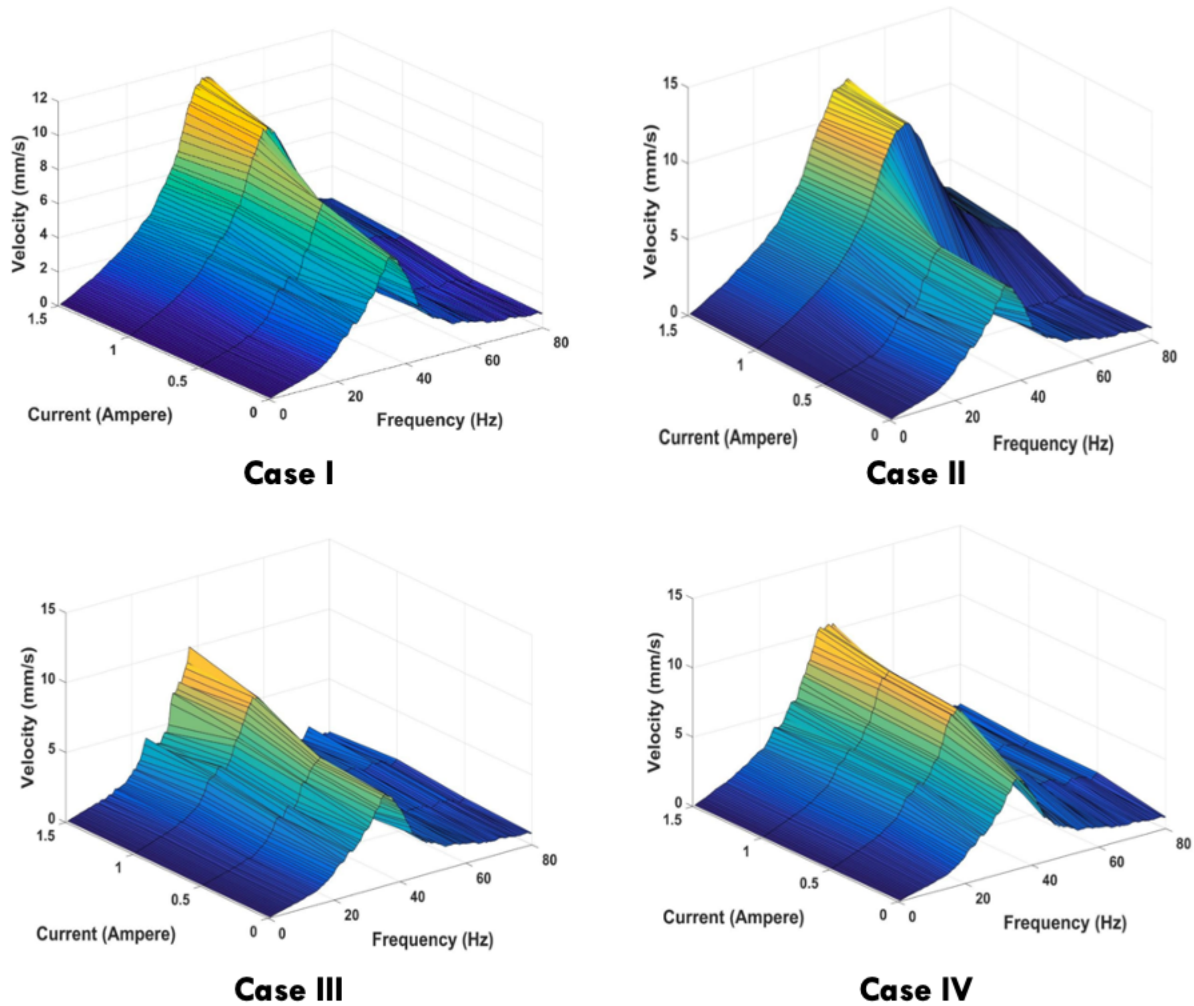

Figure 4.6: Natural frequency of the bimorph SMAHC with varying SMA layer actuation and series/parallel connection. Case I- when SMA layer with 0°orientation angle is actuated, Case II- when SMA layer with 90°orientation angle is actuated, Case III- when both SMA layers are actuated with series connection, and Case IV- when both SMA layers are actuated with parallel connection. The dependence of the ferquency is also plotted against the velocity of the structure; thus a minimum value of zero is shown in the figure.

The average change in the natural frequency of the structure with respect to the increase in current input is shown in Figure 4.6- Case I. The experimental results indicate that with the increase in current in the SMA wire, the natural frequency of the composite increases. This is because as the current value increases, the phase transformation from martensite to Austenite begins, causing an increase in the elastic modulus of the wire.

Rise in temperature and the elastic modulus increase the overall stiffness of the structure, thus increasing the natural frequency. The elastic modulus of the SMA wire is inversely proportional to the martensite fraction, which is a function of temperature. This inverse relationship can be understood by plotting elastic modulus vs. martensite fraction, as shown in Figure 4.7. There is no direct relation showing this inverse relation, hence this plot is obtained using the Brinson model Brinson (1993), which gives an iterative solution for the stress-strain relationship:

$$\sigma = \sigma_0 + E(\xi).\epsilon - E_0(\xi).\epsilon_0 + \Omega(\xi).\xi_s - \Omega_0(\xi_0).\xi_{s_0} + \Theta.(T - T_0) \tag{4.2}$$

Here, the subscript 0 denotes initial conditions, σ, is the stress, $E(\xi)$ is Youngs modulus, ϵ is the strain, $\Omega(\xi)$ is transformation tensor, Θ is the thermal coefficient of expansion, and ξ_s is the stress-induced martensite fraction. The algorithm to obtain Figure 4.7 and the material properties used by Brinson model are given in Chapter 5 and Table 5.1 respectively.

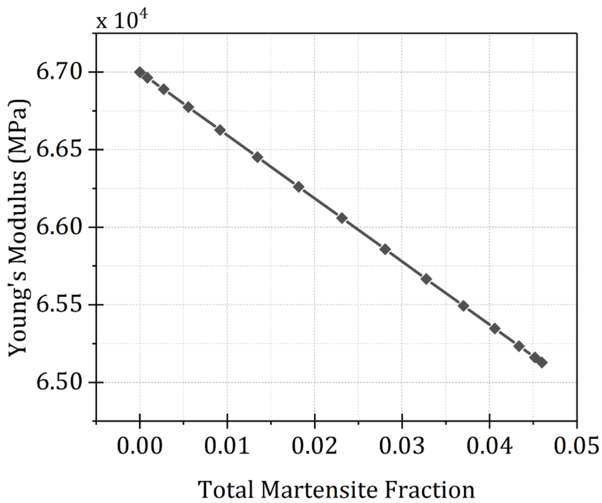

Figure 4.7: Young's modulus as a function of total martensite fraction (stress-induced + temperature-induced), plotted from Brinson's model Brinson (1993).

4.2.2 Case II: Thermal actuation of SMA layer with 90°orientation angle

The test results of the 90°orientation angle SMA layer actuation is shown in Figure 4.6-Case II. As compared to Case I, higher natural frequencies are observed in this case. The layer actuated in this case is sandwiched between other layers, unlike the previous case where the top layer is actuated, this gives a larger resistance to the movement of the embedded wire. Hence the overall stiffness is increased since very little energy is lost in the bending motion of the composite (a considerably small bending is observed in this case as previously reported in Chapter 3. Another observation we made in this test is when the top layer (Case I) is actuated, the heat is either utilised in SMA wire actuation or dissipated to the environment; hence, little to no actuation of the second layer happens. However, in this case (Case II), since the heat is trapped between layers, the heat is dissipated to the top layer, causing it to actuate as well. This results in bidirectional bending, and hence, a higher natural frequency is observed.

4.2.3 Case III: Thermal actuation of both the SMA layers when connected in series

The test results of the actuation of two SMA layers in series connection are shown in Figure 4.6- Case III. As we can see, the natural frequency of the bimorph SMAHC has considerably reduced and remains constant for 0A and 0.5A and then again for 1A and 1.5A. This behavior is caused due to simultaneous excessive heating of the composite, which softens the polymer matrix, thus reducing the overall compliance of the structure. The silicone matrix loses its stiffness with increasing temperature caused due to increased resistance due to its viscoelastic behavior. Also, excessive heating is causing the structure to bend in two orthogonal directions by actuation of both the SMA layers simultaneously; thus, an interfering bending in orthogonal directions is causing the natural frequencies to be closely distributed. Since the resistance of the wire increases every 1m (refer to Table 2.2) and each layer consists of 1m of wire, connecting them in series increases the total resistance and contributes to lower overall deflection.

4.2.4 Case IV: Thermal actuation of both the SMA layers when connected in parallel

The results for the parallel connection are shown in Figure 4.6- Case IV. Due to the distribution of the current, lesser heating due to lesser resistance for the same current value is obtained. The results for the natural frequency from this case agree with the previous trend observed in cases- I and II. A higher natural frequency is observed as compared to a series connection case, and a continuous rise is also observed. However, the natural frequencies are still quite closely separated. Thus, there are two competing actions taking place in the composite- one is an increase in stiffness due to the contraction of SMA wires, while the other is a decrease in stiffness due to excessive heating and increase in viscous behavior of the polymer matrix. Clearly, from the results, in the actuation of SMA wires in series and parallel, the latter is overriding the effect of the former.

A compilation of the average natural frequencies (average of five sets of experiments) obtained through all the cases is graphically compared in Figure 4.8a and also collated in Table 4.1. A percentage increase in the average natural frequency, with an increase in current input, is shown in Figure 4.8b. The maximum rise in average natural frequency is observed in case II, wherein the SMA layer with 90°orientation angle is thermally actuated. The large difference in average natural frequencies, in this case, causes decoupling, and hence the structure can be utilised for wider frequency range applications.

Current (Ampere)	**Frequency** (Hz)			
	0° SMA **Case 1**	90° SMA **Case 2**	Series SMA **Case 3**	Parallel SMA **Case 4**
0	35.63	35.63	35.63	35.63
0.5	36.88	36.25	35.63	37.50
1	40.63	45.63	36.25	39.38
1.5	43.13	48.75	36.25	40.63

Table 4.1: Input current vs natural frequency result for all the four cases. Case I: 0 SMA actuation, Case II: 90 SMA actuation, Case III: Series SMA actuation, Case IV: Parallel SMA actuation.

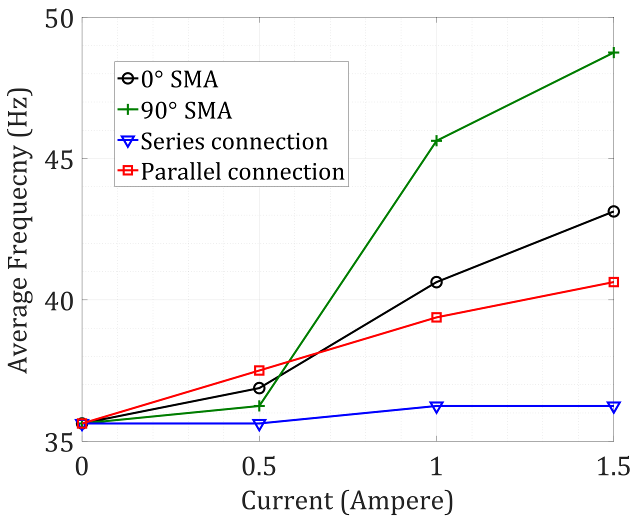

(a) Change in natural frequency with respect to current input- a comparison of all considered cases.

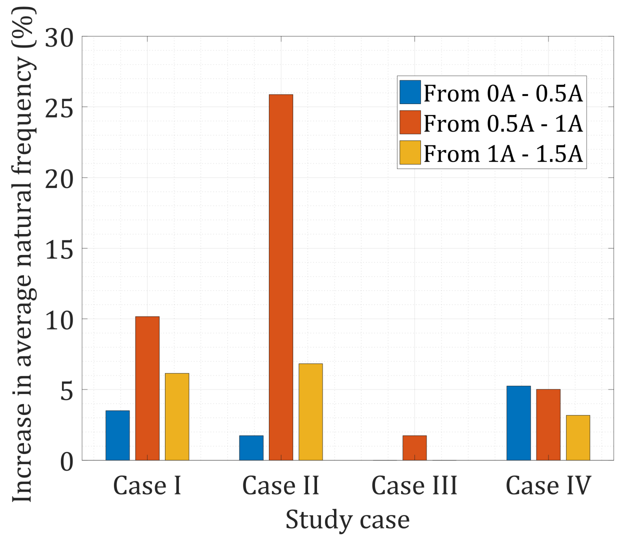

(b) Percentage increase in the average natural frequency of the bimorph SMAHC with increase in current input.

Figure 4.8: Summarising the change in natural frequency with increase in SMA temperature. Case I: 0°SMA, Case II: 90°SMA, Case III: Series connection, Case IV: Parallel connection. Note- Each frequency shown is an average of five sets of experiments with error within 5%.

4.3 Summary

The fabrication and the modal analysis of the active bimorph composite structure are presented in this chapter. Changes in the natural frequencies of the composite for four cases of actuation have been listed for different current input values. A common trend can be seen across all four cases in which an increase in the natural frequency of the composite is observed with an increase in the value of supplied current. This is caused due to a subsequent increase in the elastic modulus of the embedded SMA wire due to Joule heating. Also, the pre-strained SMA wires induce high tensile stress into the bimorph SMAHC and contribute to the increase in the natural frequency upon thermal actuation. At higher thermal input to the composite (when both the SMA layers are simultaneously heated), which is typical to series and parallel connection, a competing factor of simultaneous excessive heating of the composite also comes into play to influence the natural frequencies. Utilising these observations, we develop structures embedded with multiple layers of SMA plies, varying but optimising the SMA fiber orientation angles. Depending upon the requirement of the condition, an individual, a pair, or multiple plies, when actuated, will result in an active shift in the natural frequency and the eigenmodes of the structure. The optimisation study of the same is shown in Chapter 7. The unique contribution that we make in this chapter is finding the dependency of the natural frequency of the SMA bimorph on the voltage input, selection of SMA ply actuation, and the SMA wire connection of both layers. This observation gives a vital insight into the vibration control of these structures and further widens the field of SMA bimorph composites through vibration control and variable natural frequency.

Part II- Numerical analysis of Unimorph and Bimorph SMA Hybrid Composites (SMAHCs)

Chapter 5

Constitutive Models and Mathematical Formulation

Overview

In this chapter, we discuss the constitutive models describing the thermoelastic behavior of shape memory alloys and shape memory alloy-based hybrid composites. We also discuss the mathematical formulation of the previously discussed SMAHCs and SMAHCs with honeycomb and reentrant honeycomb core. Some mathematical preliminaries such as the rule-of-mixtures, the Halpin-Tsai equations, and the homogenization of honeycomb and reentrant honeycomb lattice structures are also discussed. The Brinson model [Brinson (1993)] is presented for the constitutive modeling of the shape memory alloy and the Turners model [Turner et al. (1994), Turner (2000)] for the SMAHCs. The mathematical formulation is based on the classical laminated plate theory, and no shear lag is assumed for the proposed cases.

5.1 Brinson 1D Constitutive Model

Several quasi-static and uniaxial constitutive models for the one-way shape memory effect exist to understand the thermomechanical behavior of shape memory alloys. These models are majorly classified into three categories: phenomenological macromechanics models, thermodynamics-based micromechanics models, and micromechanics-based hybrid macromechanics models. One of the most popular quasi-static macroscopic phenomenological constitutive models is the Brinson 1D model [Brinson (1993)][1]. In this model, strain, martensite volume fraction, and temperature are assumed to be the only state variables and the material in thermodynamic equilibrium at each instant. The stress-induced martensite at all temperatures is captured and is divided into two components-stress-induced and temperature-induced martensite fractions.

$$\xi = \xi_s + \xi_t \tag{5.1}$$

The temperature induced (ξ_t) and the stress induced (ξ_s) martensite volume fractions give the amount of detwinned martensite (single variant) caused due to loading, and the amount of martensite (all variants) occuring from the reversible phase transformation from Austenite present in the wire respectively. The sum of the both components is always $\leq$1. The SMA constitutive equation for non-constant material functions can be written as:

$$\sigma_r - \sigma_{ro} = E(\xi)\epsilon - E(\xi_o)\epsilon_o + \Omega(\xi)\xi_s - \Omega(\xi_o)\xi_{so} + \Theta(T - T_o) \tag{5.2}$$

Where, subscript 'o' denoted the initial condition, Ω, ϵ, and Θ are the phase transformation tensor, strain, and thermoelastic tensor, respectively, and 'r' subscript denotes recovery.

For Austenite to Martensite (A-M) transformation the equations that give the martensite fraction are [Chopra and Sirohi (2013)]:

[1] Schematic of phase transformation and detwinning in shape memory alloys. (a) twinned pure martensite, (b), (c) detwinned martensite, (d) pure Austenitetenite.

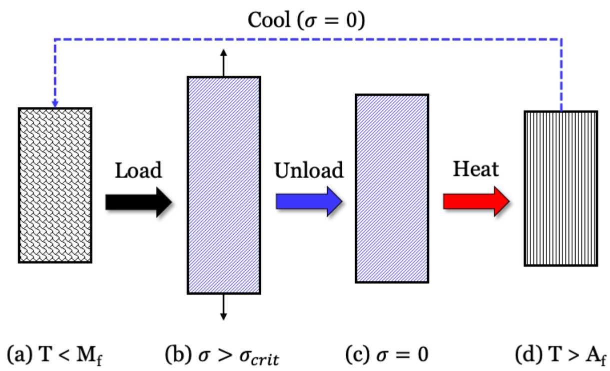

For $T > M_s$ and $\sigma_s^{cr} + C_M(T - M_s) < \sigma < \sigma_f^{cr} + C_M(T - M_s)$,

$$\xi_s = \frac{(1-\xi_{so})}{2}\cos\left[\frac{\pi}{\sigma_s^{cr} - \sigma_f^{cr}}(\sigma - \sigma_f^{cr} - C_M(T - M_s))\right] + \frac{(1+\xi_{so})}{2} \tag{5.3a}$$

$$\xi_t = \xi_{to} - \frac{\xi_{to}}{1-\xi_{so}}(\xi_s - \xi_{so}) \tag{5.3b}$$

And, for $T < M_s$ and $\sigma_s^{cr} < \sigma < \sigma_f^{cr}$,

$$\xi_s = \frac{(1-\xi_{so})}{2}\cos\left[\frac{\pi}{\sigma_s^{cr} - \sigma_f^{cr}}(\sigma - \sigma_f^{cr})\right] + \frac{(1+\xi_{so})}{2} \tag{5.4a}$$

$$\xi_t = \xi_{to} - \frac{\xi_{to}}{1-\xi_{so}}(\xi_s - \xi_{so}) + \Delta_{T\xi} \tag{5.4b}$$

Here, if $M_f < T < M_s$ and $T < T_o$ $\Delta_{T\xi} = \frac{1-\xi_{to}}{2}[\cos(a_M(T - M_f)) + 1]$, else $\Delta_{T\xi} = 0$. Now, for Martensite to Austenite(M-A) transforamtion the equation that give the martensite fraction are:

For $T > A_s$ and $C_A(T - A_f) < \sigma < C_A(T - A_s)$

$$\xi = \frac{\xi_o}{2}\cos\left[\frac{\pi}{(A_f - A_s)}\left(T - A_s - \frac{\sigma}{C_A}\right) + 1\right] \tag{5.5a}$$

$$\xi_s = \xi_{so} - \frac{\xi_{so}}{\xi_o}(\xi_o - \xi) \tag{5.5b}$$

$$\xi_t = \xi_{to} - \frac{\xi_{to}}{\xi_o}(\xi_o - \xi) \tag{5.5c}$$

Where, M_s: martensite start temperature, M_f: martensite finish temperature,A_s: Austenite start temperature, A_f: Austenite finish temperatures, σ_s^{cr}: critical stress start, σ_f^{cr}: critical stress finish (transformation from twinned to detwinned martensite), C_M: stress influence coefficient for the martensite phase, C_A: stress influence coefficient for the Austenite phase. In this model the Young's modulus of the SMA is taken the same as given by Tanaka (1986):

$$E(\xi) = E_A + \xi(E_M - E_A) \tag{5.6}$$

Here, E_M and E_A are the Young's modulus of the SMA in the Martensite and the Austenite phases respectively. Also, the phase transformation tensor at a fixed value of ξ, ξ_0 is written as:

$$\Omega(\xi) = -\epsilon_L E(\xi) \tag{5.7}$$

To verify that the recovery stress satisfies the Brinson Model, we reproduced major plots from the Brinson model using the material properties as given by Brinson (1993), and are added here:

Moduli
$E_A = 67$ x 10^3 MPa
$E_M = 26.3$ x10^3 MPa
$\Theta = 0.55$ MPa/°C
Transformation Temperatures
$M_f = 9$°C
$M_s = 18.4$°C
$A_s = 4.5$°C
$A_f = 49$°C
Transformation Constants
$C_M = 8$ MPa/° C
$C_A = 13.8$ MPa/°C
$\sigma_s^{cr} = 100$ MPa
$\sigma_f^{cr} = 170$ MPa
Maximum Residual Strain
$\epsilon_L = 0.067$

Table 5.1: SMA material properties used for the Brinson (1993) model.

Figure 5.1 shows the stress-strain relationship we get through the reproduced model plotted against Brinsons result, Figure 5.2(a) gives the martensite fraction v/s stress relation, Figure 5.2(b) gives the change in residual strain when the temperature is increased.

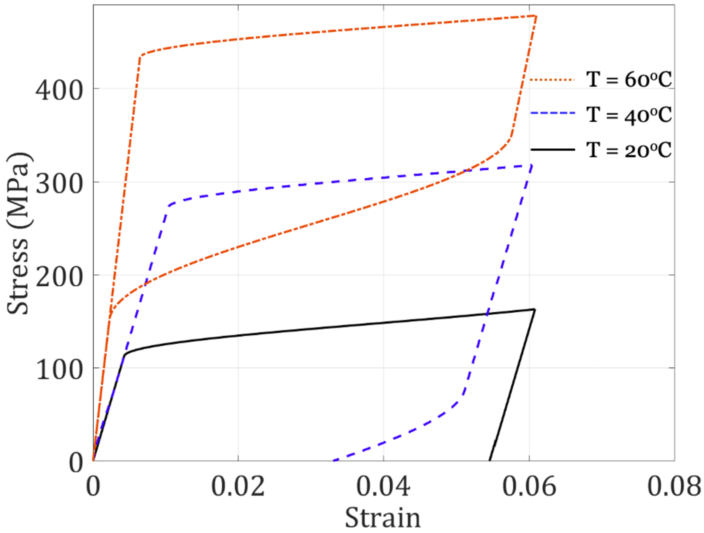

Figure 5.1: Stress-strain curves for varying temperatures obtained plotted against Brinson Model

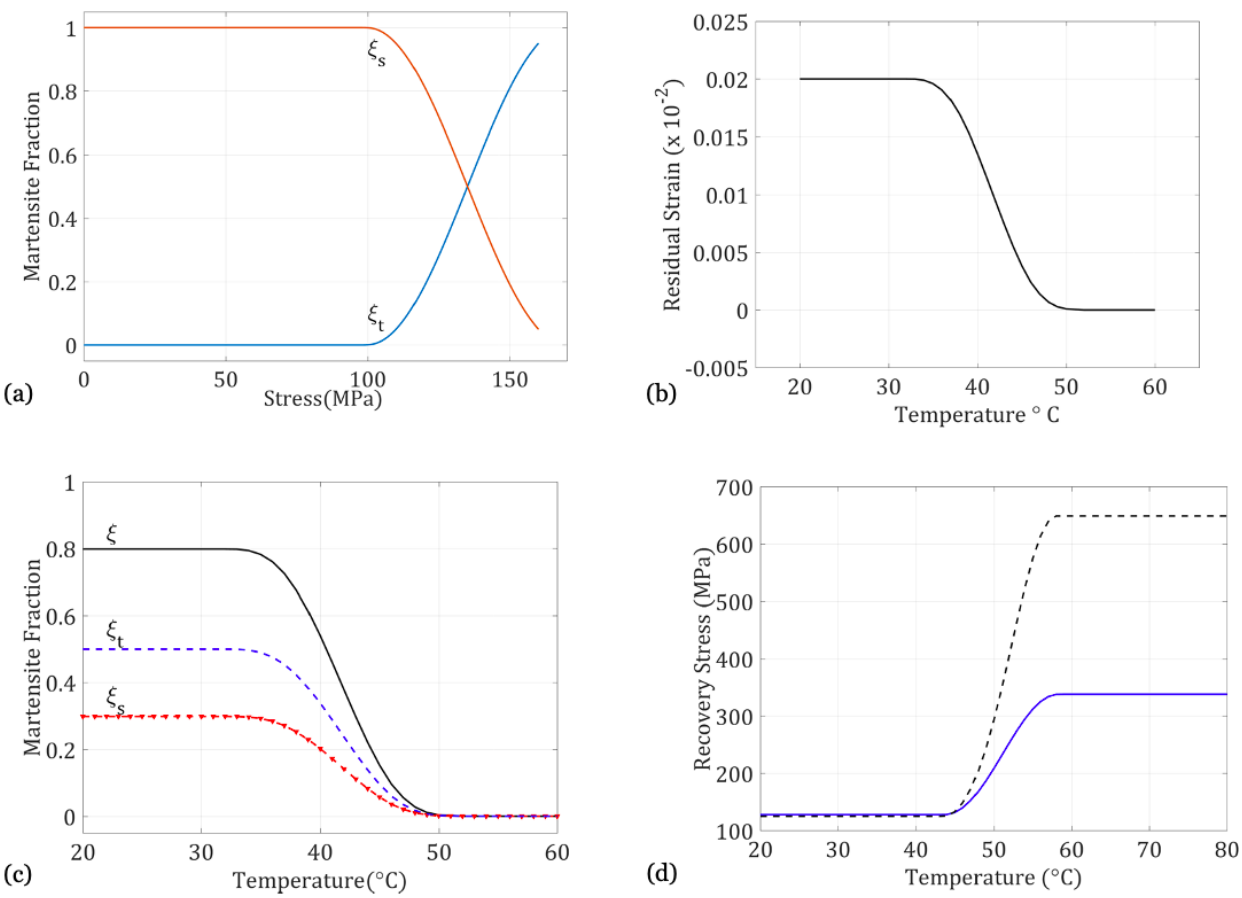

Figure 5.2: Brinson 1D Model for shape memory alloys. (a) Martensite Fraction vs Temperature. ξ_{so} = 0, ξ_{to} = 1, T = 5°C from stress-strain analysis with $\sigma_o = \epsilon_o$. (b) Residual Strain vs Temperature. $\xi_{so} = 0.02/\epsilon_L$, ξ_{to} = 0.5, (c) Martensite Fraction vs Temperature. $\xi_{so} = 0.02/\epsilon_L$, ξ_{to} = 0.5, (d) Recovery Stress vs Temperature. ϵ_o = 0.5% & 0.9%, ξ_{so} = 0.046 & 0.073, ξ_{to} = 0 & 0.92, σ_o = 128

In Figure 5.2(c) we can see the variation of martensite fraction with temperature compared against the reproduced Brinson model for 2% strain and for 1% strain. Finally, Figure 5.2(d) shows the recovery stress v/s temperature result plotted against the data plotted in Turners thermoelastic model Turner (2000).

5.2 Turners Effective Coefficient of Thermal Expansion Model (ECTE)

Turners ECTE model gives the constitutive equations for the thermomechanical response prediction of SMA embedded composites undergoing both mechanical loads and thermal loads [Turner (2000)]. The model is applicable for free recovery, constrained, as well as restrained behavior of SMA, given that we possess data for basic SMA material properties. The material nonlinearity of SMA as a function of temperature and the embedded composite mechanics can be captured through this model as well. A representative volume element employed in Turners model is shown in Figure 5.3. This element is considered in the plane of the plate, the principal material directions are 1 and 2, wherein the SMA wire is embedded along 1-direction.

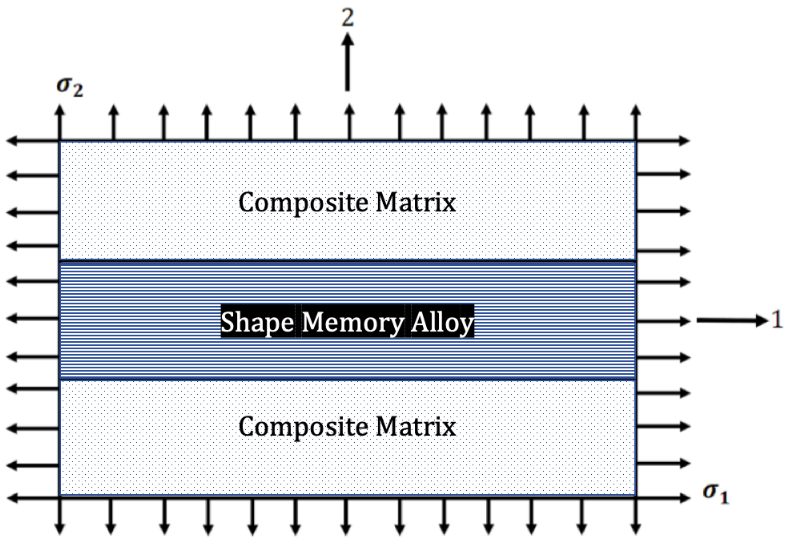

Figure 5.3: Volume element of the SMAHC lamina [Turner (2000)].

For a SMAHC lamina of Glass-Epoxy embedded with NiTiNOL wires, adding the thermal expansion behavior of NiTiNOL from Turner, Zhong, and Mei [Turner et al.

(1994)] to the 1D uniaxial thermoelastic constitutive relation by Jia and Rogers (1989):

$$\sigma_{1a} = E_a \epsilon_1 + \sigma_r \qquad T \geq A_s \tag{5.8a}$$

$$\sigma_{1a} = E_a(\epsilon_1 - \alpha_{1a}\Delta T) \qquad T < A_s \tag{5.8b}$$

Here, E_a is the Youngs Modulus of the SMA, ϵ_1 is the strain in 1-direction (longitudinal), α_{1a} is the coefficient of thermal expansion for SMA along 1-direction at temperature, T less than the Austenite start temperature, A_s, and σ_r is the recovery stress of the SMA when $T \geq A_s$.

The thermoelastic constitutive relation for uniaxial conditions is written in terms of Effective Coefficient of Thermal Expansion (ECTE):

$$\sigma_{1a} = E_a \left[\epsilon_1 - \int_{T_0}^{T} \alpha_{1a}(\tau) d\tau \right] \tag{5.9}$$

From equations (5.8a), (5.8b) and (5.9) we see that at temperature below Austenite start temperature,

$$\int_{T_0}^{T} \alpha_{1a}(\tau) d\tau = \alpha_{1a}\Delta T \tag{5.10}$$

and at temperatures above Austenite start temperature,

$$\begin{aligned} \sigma_r &= -E_a \int_{T_0}^{T} \alpha_{1a}(\tau) d\tau \\ or, \int_{T_0}^{T} \alpha_{1a}(\tau) d\tau &= -\frac{\sigma_r}{E_a} \end{aligned} \tag{5.11}$$

Using the above equations we can capture the non-linear thermoelastic behavior of the SMA. Similarly, the constitutive equation for the transverse direction is:

$$\sigma_{2a} = E_a \left[\epsilon_2 - \int_{T_0}^{T} \alpha_{2a}(\tau) d\tau \right] \tag{5.12}$$

In the case of SMA wires reinforced unidirectionally along 1-direction α_{2a} is not related to recovery stress but is linear due to change in martensite fraction. Thus, the thermoelastic constitutive relations for an orthotropic lamina under plane stress becomes:

$$\begin{pmatrix} \sigma_1 \\ \sigma_2 \\ \tau_{12} \end{pmatrix} = \begin{bmatrix} Q_{11} & Q_{12} & 0 \\ Q_{12} & Q_{22} & 0 \\ 0 & 0 & Q_{66} \end{bmatrix} \begin{pmatrix} \epsilon_1 \\ \epsilon_2 \\ \gamma_{12} \end{pmatrix} - \begin{bmatrix} Q_{11} & Q_{12} & 0 \\ Q_{12} & Q_{22} & 0 \\ 0 & 0 & Q_{66} \end{bmatrix} \int_{T_0}^{T} \begin{pmatrix} \alpha_1 \\ \alpha_2 \\ 0 \end{pmatrix} d\tau \tag{5.13}$$

Here $[Q]$ is the reduced stiffness matrix or the compliance matrix. The above constitutive relation is the ECTEM model- effective coefficient of thermal expansion model. The relation between the reduced stiffness matrix and the engineering constants, Rule-of-Mixtures, and Halpin-Tsai equations are discussed in Section 5.3.

We employed ECTEM in our work due to the following main reasons:

- We do not require the superelastic effect for constrained recovery analysis; this model suitably predicts the required Shape Memory Effect.

- The model requires only four parameters- Austenite Start Temperature, Austenite Finish Temperature, Recovery Stress, and Youngs Modulus, and we had resources available to calculate the same.

5.3 Reduced Stiffness Matrix and Rule-of-Mixtures

The composite material properties depend upon its constituents, their distribution, and physical and chemical interaction between the constituents. The conventional method used to determine the properties of composites is through experimental measurements; however, the properties of only a fixed fiber matrix system fabricated by a specific method can be determined. Hence, theoretical and semiempirical methods are used to predict the effects of multiple system variables on the effective mechanical properties of the composites. The formulae for the longitudinal properties such as Youngs modulus, Poissons ratio, and shear modulus of a composite are discussed here. For the modeling of unidirectional composites, the continuous fibers are assumed to be uniform in mechanical properties and dimensions, aligned parallel throughout the composite, are perfectly bonded with the matrix, and no interface slippage occurs due to any external loads, and lastly, the strains in the fibers, matrix and the composite are exactly the same.

$$
\begin{aligned}
E_1 = E_a V_a + E_m V_m \quad E_2 &= \frac{E_a E_m}{E_a V_m + E_m V_a} \\
\nu_{12} = \nu_a V_a + \nu_m V_m \quad G_{12} &= \frac{G_a G_m}{G_a V_m + G_m V_a} \\
\int_{T_o}^{T} \alpha_1(\tau) d\tau &= \frac{E_a V_a \int_{T_o}^{T} \alpha_a(\tau) d\tau + E_m V_m \int_{T_o}^{T} \alpha_m(\tau) d\tau}{E_a V_a + E_m V_m} \\
sgn(\alpha_a) &= \begin{cases} +1 & \mathrm{T} < A_s \\ -1 & \mathrm{T} \geq A_s \end{cases} \\
\int_{T_o}^{T} \alpha_2(\tau) d\tau &= \int_{T_o}^{T} [\alpha_a(\tau) V_a + \alpha_m(\tau) V_m] d\tau
\end{aligned}
\tag{5.14}
$$

Where the subscripts 'a, and 'm denote the SMA/fiber and matrix respectively, E, ν, G, α are Youngs modulus, Poissons ratio, shear modulus, and effective coefficient of thermal expansion respectively, V_a and V_m are the SMA/fiber and matrix volume fraction respectively. From the above equations, we can observe that the contribution of the mechanical properties of the fibers and the matrix are proportional to their volume fractions in the composite. The above relations are called *rule of mixtures*. The author suggests Werber (1980) for detailed information on the origin and derivation of these equations.

From the mechanics point of view, reinforced fiber composites fall under the class of orthotropic materials, and their behavior lies between anisotropic materials and isotropic materials. The deformation response of an orthotropic material is similar to an anisotropic material since it is dependent on the direction and normal, and shear stresses generate normal and shear strains. However, in unique cases, when the loads are applied in certain directions, the material responds as an isotropic material. The composite laminates are loaded in the plane of the laminate in structural applications, called a plane-stress condition, and all out-of-plane stress components are negated. The following equation gives us the stress-strain relationship for specially orthotropic lamina under the plane-stress condition:

$$\begin{pmatrix} \sigma_1 \\ \sigma_2 \\ \tau_{12} \end{pmatrix} = \begin{bmatrix} Q_{11} & Q_{12} & 0 \\ Q_{12} & Q_{22} & 0 \\ 0 & 0 & Q_{66} \end{bmatrix} \begin{pmatrix} \epsilon_1 \\ \epsilon_2 \\ \gamma_{12} \end{pmatrix} \tag{5.15}$$

Where, *[Q]* is the compliance matrix and its elements are defined as:

$$\begin{gathered} Q_{11} = \frac{E_1}{1 - \nu_{12}\nu_{21}} \qquad Q_{12} = \frac{\nu_{12}E_2}{1 - \nu_{12}\nu_{21}} \\ Q_{22} = \frac{E_2}{1 - \nu_{12}\nu_{21}} \qquad Q_{66} = G_{12} \end{gathered} \tag{5.16}$$

For a detailed explanation of the derivation of the compliance matrix from a general isotropic material using Hookes law to transversely isotropic material, leading to the aforementioned case of specially orthotropic material under plane stress, the author suggests Werber (1980).

5.4 Homogenization formulation for Periodic Honeycomb layer

The equivalent mechanical properties of a honeycomb lattice cell can be obtained using the beam theory. For this, the material constants of the honeycomb material such as the mass density, ρ_s, Youngs modulus, E_s, Poissons ratio, ν_s, and the shear modulus which can be obtained from $G_s = E_s/2(1 - \nu_s)$ is required. In the present case, we assume our honeycomb layer to be fabricated from the same constituent materials as in the case of conventional woven E-glass fiber composite.

The relative density of the honeycomb cell is given by Gibson and Ashby (1999):

$$\frac{\rho_h}{\rho_s} = \frac{(\frac{t}{l})(\frac{h}{l} + 2)}{2(\frac{h}{l} + \sin\theta)\cos\theta} \tag{5.17}$$

Here, ρ_h denotes the density of the honeycomb cell, h, l, and t, denote the height, the strut length, and the thickness of the strut respectively; and θ is positive as shown, for the case of auxetic θ becomes negative. In our case, we assume symmetric and homogenous lattice cell wherein $h = 2.5 * l$ and calculate the equivalent in-plane and out-of-plane mechanical properties. The in-plane and out-of-plane mechanical properties of a honeycomb cell are compiled by Sorohan et al. (2019):

$$E_1^h = k_1.E_s \left(\frac{t}{l}\right)^3 \frac{\cos\theta}{\left(\frac{h}{l} + \sin\theta\right)\sin^2\theta} \tag{5.18a}$$

$$E_2^h = k_2.E_s \left(\frac{t}{l}\right)^3 \frac{\left(\frac{h}{l} + \sin\theta\right)}{\cos^3\theta} \tag{5.18b}$$

Where, k_1 and k_2 are calculated as:

$$k_1 = \frac{1}{1 + \left(\frac{t}{l}\right)^2 (2.4 + 1.5\nu_s + cot^2\theta)} \tag{5.19}$$

$$k_2 = \frac{1}{1 + \left(\frac{t}{l}\right)^2 (2.4 + 1.5\nu_s + tan^2\theta)} \tag{5.20}$$

The in-plane Poissons ratios can be calculated using:

$$\nu_{12}^h = c_{12} \frac{\cos^2\theta}{\left(\frac{h}{l} + \sin\theta\right)\sin\theta} \tag{5.21a}$$

$$\nu_{21}^h = c_{21} \frac{\left(\frac{h}{l} + \sin\theta\right)\sin\theta}{\cos^2\theta} \tag{5.21b}$$

where,

$$c_{12} = \frac{1 + \left(\frac{t}{l}\right)^2 (1.4 + 1.5\nu_s)}{1 + \left(\frac{t}{l}\right)^2 (2.4 + 1.5\nu_s + cot^2\theta)} \tag{5.22a}$$

$$c_{21} = \frac{1 + \left(\frac{t}{l}\right)^2 (1.4 + 1.5\nu_s)}{1 + \left(\frac{t}{l}\right)^2 \left(2.4 + 1.5\nu_s + tan^2\theta + 2\frac{h}{l\cos^2\theta}\right)} \tag{5.22b}$$

The in-plane shear modulus for commercial honeycombs is [Sorohan et al. (2019)]:

$$G_{12}^h = E_s \left(\frac{t}{l}\right)^3 \frac{\frac{h}{l} + \sin\theta}{\left(\frac{h}{l}\right)^2 \left(1 + \frac{h}{4l}\right)\cos\theta} \tag{5.23}$$

If the axial and shearing force contributions to the total strain energy are neglected, the coefficients, or the correction factors, k_1, k_2, c_{12}, and c_{21}, become equal to 1.

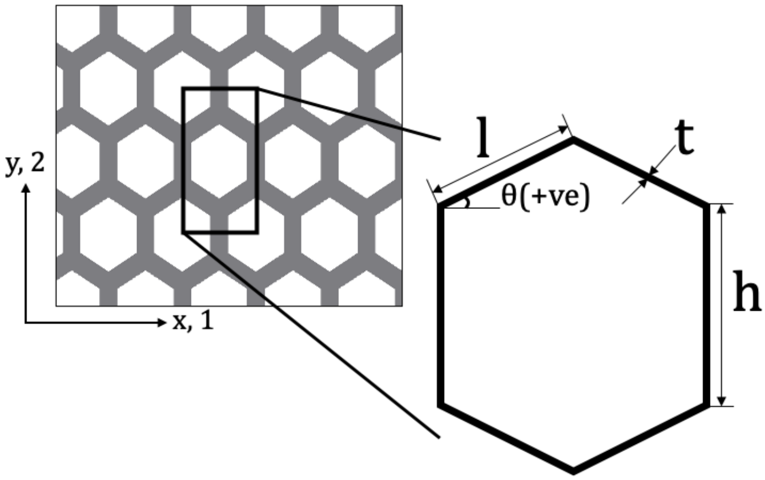

Figure 5.4: Representative volume element of the honeycomb lamina; l, h are the inclined and the vertical honeycomb struts respectively, t is the thickness of the strut; h= 2.5 x l.

The out-of-plane properties for the honeycomb layer are:

$$E_3^h = E_s \frac{\rho_h}{\rho_s}; \quad \nu_{13}^h = \nu_s \frac{E_1}{E_3}; \quad \nu_{23}^h = \nu_s \frac{E_2}{E_3}; \quad \nu_{31}^h = \nu_{32}^h = \nu_s \tag{5.24}$$

These relationships are applicable only for $t << l$ and the height of the ply, $b << l$ because the shear stresses are uniform within the cell walls. The out-of-plane shear moduli can be obtained from:

$$G_{13}^h = G_s \left(\frac{t}{l}\right) \frac{\cos\theta}{\frac{h}{l} + \sin\theta} \tag{5.25a}$$

$$G_{23}^h = G_{23}^L + \alpha \left(\frac{l}{b}\right) \left(G_{23}^U - G_{23}^L)\right) \tag{5.25b}$$

where,

$$G_{23}^U = G_s \left(\frac{t}{l}\right) \frac{\frac{h}{l} + \sin^2\theta}{\left(\frac{h}{l} + \sin\theta\right) \cos\theta} \tag{5.26a}$$

$$G_{23}^L = G_s \left(\frac{t}{l}\right) \frac{\frac{h}{l} + \sin\theta}{\left(\frac{h}{l} + 1\right) \cos\theta} \tag{5.26b}$$

and,

$$\alpha = \begin{cases} 0.787, & \theta \geq 0^\circ \\ 1.342, & \theta < 0^\circ \end{cases}$$

Here, G_{23}^U and G_{23}^L are the upper and lower bounds of the out-of-plane G_{23} shear modulus and α for a honeycomb ($\theta \geq 0$) is deduced by Grediac (1993) by analysing multiple aspect ratios vs. shear modulus data, and for reentrant honeycomb (negative Poissons ratio, $\theta < 0$) by Scarpa and Tomlin (2000). For the auxetic, we take the θ as negative, and the rest of the calculations remain the same. For the model considered in the thesis, we take t= 0.5mm, l= 5mm, h= 2.5 x l= 12.5 mm (to avoid failure of structure by collapsing on itself when $\theta < 0^\circ$), and b= 2.5mm, the collated material properties are given in Table 6.2. Mukhopadhyay and Adhikari (2016) in their work give a collated behaviour of the effective elastic modulus along the longitudinal (E_1) and transverse (E_2) direction, shear modulus (G_{12}), and the Poissons ratio (ν_{12}). We reproduce the graph to verify the validity of our code [Figure 5.5].

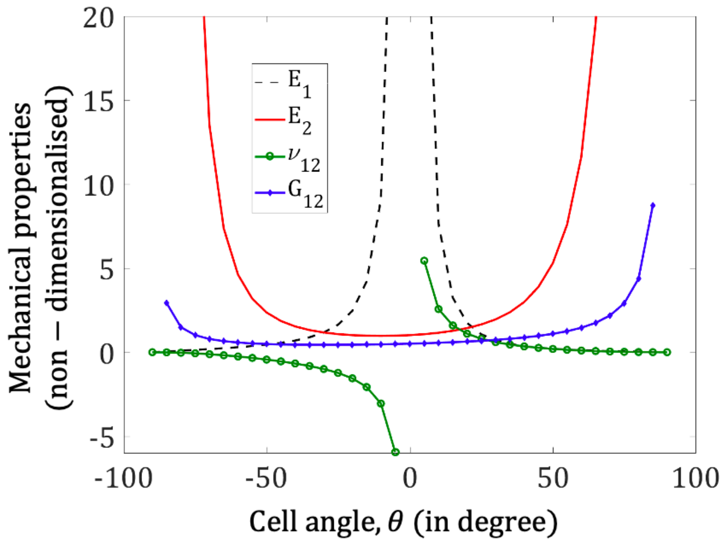

Figure 5.5: Variation of different non-dimensionalised mechanical properties with cell angle θ for honeycomb ($\theta > 0^\circ$) and reentrant honeycomb ($\theta < 0^\circ$) lattices for $h/l = 2$

5.5 Governing equations of SMA Hybrid Composite (SMAHC) plate

A simply-supported orthotropic square plate subjected to thermal load is considered. It is assumed that the thin plate has a uniform thickness $\overline{h}$, and the thickness is in the range of $1/20 \sim 1/100$ approximately of its span. Following are the assumptions made upon which the deflections and stresses are based:

1. The plate holds the *hypothesis of straight normals*, and the Classical Laminated Plate Theory (CLPT).

2. Due to thin plate, the stress normal to the middle plane, σ_z, is small compared to other stress components hence neglected.

3. Turners Recovery Stress Model is employed for the lamina embedded with SMA wires [Turner et al. (1994), Turner (2000)].

4. The material properties of the SMA wires reinforced lamina are a function of martensite fraction, which is a function of temperature.

5. The homogenization of the periodic honeycomb/auxetic layer is done using Sorohan *et al.* work and the equivalent mechanical properties are used as input [Sorohan et al. (2015)].

5.5.1 The stress field

Consider a section of the laminate which undergoes deformation in $x-z$ plane as shown in Figure 5.6. Following the CLPT, the edge $ABCD$ remains straight and perpendicular to the mid-plane even in the deformed state. As is apparent, point B is located at the geometric mid-plane and undergoes displacements, u_o, v_o, and w_o along x, y, and z directions respectively. Therefore, for point C (refer Figure 5.6) the displacements in x and y direction are given as:

$$u = u_o - z\alpha; v = v_o - z\alpha \tag{5.27}$$

Where α is the slope of the mid-plane in the x direction,

$$\alpha = \frac{\partial w_o}{\partial x} \tag{5.28}$$

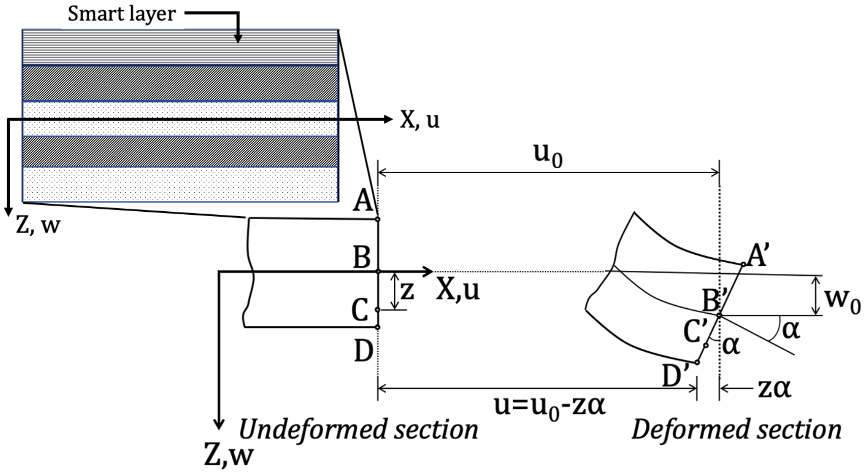

Figure 5.6: Bending of an element of the smart composite in X-Z plane showing both mid-plane deformation as well as pure bending. Shear deformation is neglected in this model.

As per the first assumption, the stretching/shortening of the normal $ABCD$ is insignificant as compared to the displacement, w_o, thus the normal strain, ϵ_z is neglected. This reduces the laminate strains in x, y, and z directions to:

$$\begin{aligned} \epsilon_x &= \frac{\partial u}{\partial x} = \frac{\partial u_o}{\partial x} - z\frac{\partial^2 w_o}{\partial x^2} = \epsilon_x^o - z\kappa_x \\ \epsilon_y &= \frac{\partial v}{\partial y} = \frac{\partial v_o}{\partial y} - z\frac{\partial^2 w_o}{\partial y^2} = \epsilon_y^o - z\kappa_y \\ \gamma_{xy} &= \frac{\partial u}{\partial y} + \frac{\partial v}{\partial x} = \frac{\partial u_o}{\partial y} + \frac{\partial v_o}{\partial x} - 2z\frac{\partial^2 w_o}{\partial x \partial y} = \gamma_{xy}^o - z\kappa_{xy} \end{aligned} \tag{5.29}$$

Here, $\epsilon_x^o, \epsilon_y^o$, and γ_{xy}^o the mid-plane strains, whereas, κ_x, κ_y, and κ_{xy} are the plate curvatures respectively. Due to the slenderness ratio assumption as discussed before, the transverse shear deformations are negligible, and as indicated by Shames and Dym (1985), the classical theory of plates holds good.

Based on the assumptions 2, and 3 the stress-strain relations for plane stress for lamina embedded with SMA wires, and a conventional fiber-reinforced lamina respectively are:

$$\begin{Bmatrix} \sigma_x \\ \sigma_y \\ \tau_{xy} \end{Bmatrix}^s = \begin{bmatrix} \bar{Q}^*_{11} & \bar{Q}^*_{12} & 0 \\ \bar{Q}^*_{12} & \bar{Q}^*_{22} & 0 \\ 0 & 0 & Q^*_{66} \end{bmatrix} \left(\begin{Bmatrix} \epsilon^o_x \\ \epsilon^o_y \\ \gamma^o_{xy} \end{Bmatrix} + z \begin{Bmatrix} \kappa_x \\ \kappa_y \\ \kappa_{xy} \end{Bmatrix} \right) + \begin{Bmatrix} \sigma^*_r \\ 0 \\ 0 \end{Bmatrix} V_s$$
$$- \begin{bmatrix} \bar{Q}_{11} & \bar{Q}_{12} & 0 \\ \bar{Q}_{12} & \bar{Q}_{22} & 0 \\ 0 & 0 & Q_{66} \end{bmatrix}^m \begin{Bmatrix} \alpha_x \\ \alpha_y \\ 0 \end{Bmatrix}^m V_m \Delta T \tag{5.30}$$

$$\begin{Bmatrix} \sigma_x \\ \sigma_y \\ \tau_{xy} \end{Bmatrix}^{f/h/a} = \begin{bmatrix} \bar{Q}_{11} & \bar{Q}_{12} & 0 \\ \bar{Q}_{12} & \bar{Q}_{22} & 0 \\ 0 & 0 & Q_{66} \end{bmatrix}^{f/h/a} \left(\begin{Bmatrix} \epsilon^o_x \\ \epsilon^o_y \\ \gamma^o_{xy} \end{Bmatrix} + z \begin{Bmatrix} \kappa_x \\ \kappa_y \\ \kappa_{xy} \end{Bmatrix} - \begin{Bmatrix} \alpha_x \\ \alpha_y \\ 0 \end{Bmatrix}^{f/h/a} \Delta T \right) \tag{5.31}$$

Where, the superscripts, $s, m, f, h,$ and a denote the SMA wire embedded in matrix layer, matrix, conventional fiber-reinforced lamina, honeycomb ply, and auxetic, respectively. Here, Q^*_{ij}, Q^m_{ij}, and $Q^{f/h/a}_{ij}$ matrices are the stiffness matrices corresponding to SMA fiber-matrix, the matrix in which SMA is embedded, and of E-glass fiber-matrix/honeycomb/auxetic honeycomb, respectively.

5.5.2 The axial forces, shear forces, and the bending moment

Since the stresses in the laminate vary in each layer, the equivalent system of forces and moments acting on the cross-section of the laminate are defined. These equivalent system of forces or stress resultants per unit length of the middle surface are calculated by integrating stresses through the thickness:

$$N_x = \int_{-h}^{h} \sigma_x dz, \qquad N_y = \int_{-h}^{h} \sigma_y dz, \qquad N_{xy} = \int_{-h}^{h} \tau_{xy} dz \tag{5.32}$$

Similarly, the equivalent moments per unit length are defined as:

$$M_x = \int_{-h}^{h} \sigma_x \, z \, dz, \qquad M_y = \int_{-h}^{h} \sigma_y \, z \, dz, \qquad M_{xy} = \int_{-h}^{h} \tau_{xy} \, z \, dz \tag{5.33}$$

The positive sense of the resultant forces and moments are consistent with the sign convention of the stresses and are shown in Figure 5.7:

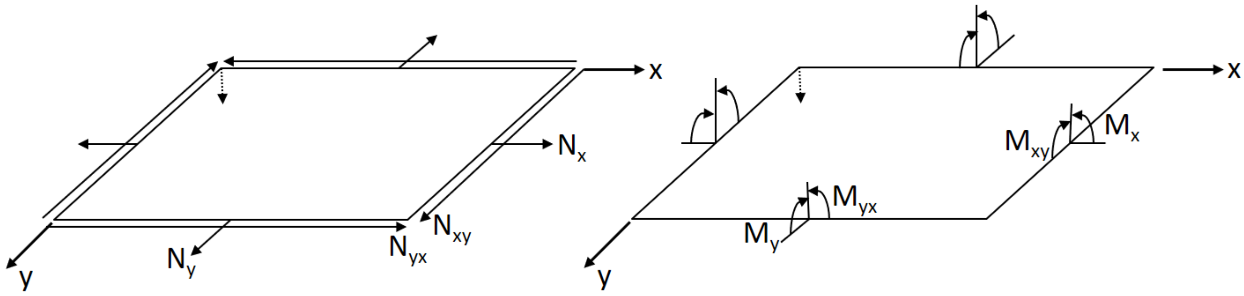

Figure 5.7: Stress resultant and moments in SMAHC plate mid-plane.

The force-moment system acting at the mid-plane of the laminate can be obtained by summing the integrals representing the contribution of each layer, giving us:

$$\begin{Bmatrix} N_x \\ N_y \\ N_{xy} \end{Bmatrix} = \sum_{k=1}^{n} \int_{h_{k-1}}^{h_k} \begin{Bmatrix} \sigma_x \\ \sigma_y \\ \tau_{xy} \end{Bmatrix} dz \tag{5.34}$$

$$\begin{Bmatrix} M_x \\ M_y \\ M_{xy} \end{Bmatrix} = \sum_{k=1}^{n} \int_{h_{k-1}}^{h_k} \begin{Bmatrix} \sigma_x \\ \sigma_y \\ \tau_{xy} \end{Bmatrix} zdz \tag{5.35}$$

The stresses in equations 5.34 can also be written in terms of mid-plane strains and plate curvatures. Upon substituting equations 5.30 in equations 5.34, we obtain the resultant axial forces and moments as:

$$\begin{Bmatrix} N_x \\ N_y \\ N_{xy} \end{Bmatrix} = \begin{bmatrix} A^*_{11} & A^*_{12} & A^*_{16} \\ A^*_{12} & A^*_{22} & A^*_{26} \\ A^*_{16} & A^*_{26} & A^*_{66} \end{bmatrix} \begin{Bmatrix} \epsilon^o_x \\ \epsilon^o_y \\ \gamma^o_{xy} \end{Bmatrix} + \begin{bmatrix} B^*_{11} & B^*_{12} & B^*_{16} \\ B^*_{12} & B^*_{22} & B^*_{26} \\ B^*_{16} & B^*_{26} & B^*_{66} \end{bmatrix} \begin{Bmatrix} \kappa_x \\ \kappa_y \\ \kappa_{xy} \end{Bmatrix} - \begin{Bmatrix} N^{T^*}_x \\ N^{T^*}_y \\ N^{T^*}_{xy} \end{Bmatrix} \tag{5.36}$$

$$\begin{Bmatrix} M_x \\ M_y \\ M_{xy} \end{Bmatrix} = \begin{bmatrix} B_{11}^* & B_{12}^* & B_{16}^* \\ B_{12}^* & B_{22}^* & B_{26}^* \\ B_{16}^* & B_{26}^* & B_{66}^* \end{bmatrix} \begin{Bmatrix} \epsilon_x^o \\ \epsilon_y^o \\ \epsilon_{xy}^o \end{Bmatrix} + \begin{bmatrix} D_{11}^* & D_{12}^* & D_{16}^* \\ D_{12}^* & D_{22}^* & D_{26}^* \\ D_{16}^* & D_{26}^* & D_{66}^* \end{bmatrix} \begin{Bmatrix} \kappa_x \\ \kappa_y \\ \kappa_{xy} \end{Bmatrix} - \begin{Bmatrix} M_x^{T^*} \\ M_y^{T^*} \\ M_{xy}^{T^*} \end{Bmatrix} \tag{5.37}$$

Here, the superscript $'*'$ indicates the properties to be temperature dependent.

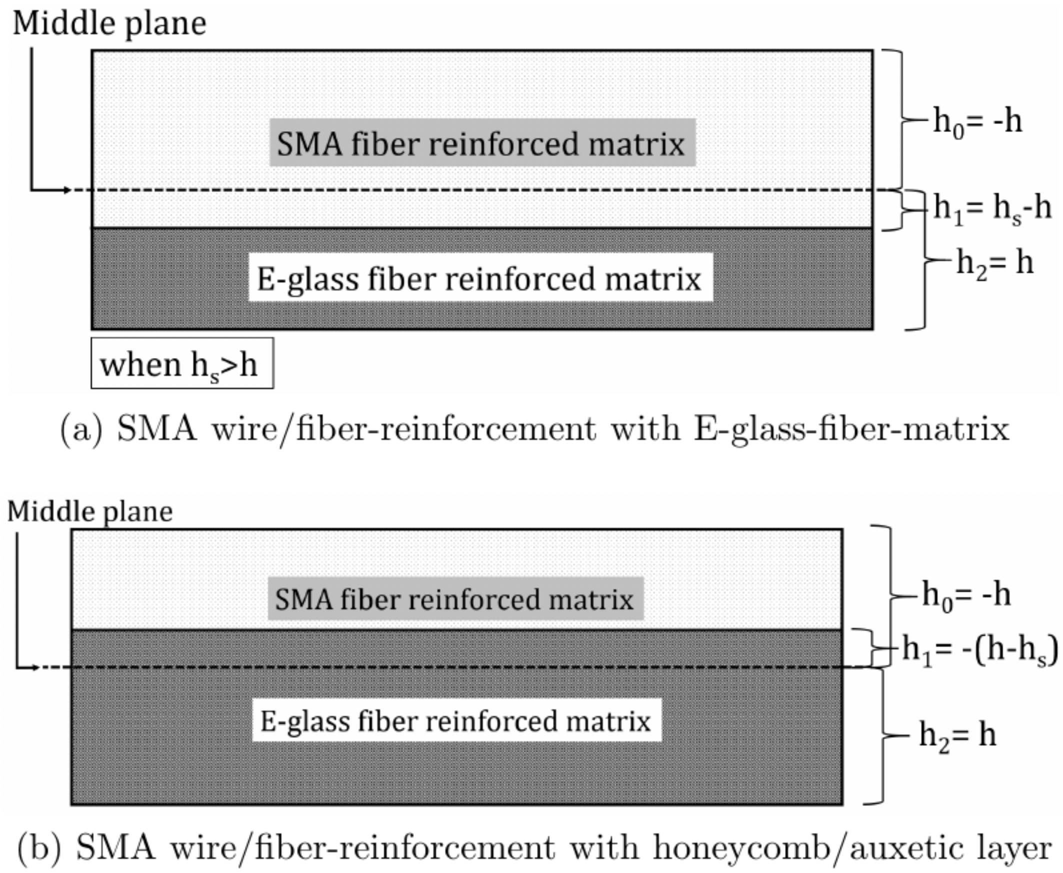

Figure 5.8: Schematic of ply lay-up of SMA wire embedded unimorph composite.

The coefficients A_{ij}^*, B_{ij}^*, and D_{ij}^* when one layer of SMA reinforcement is present and $h_s > h$ are:

$A_{ij}^* = \left(\bar{Q}_{ij}^* h_s + \bar{Q}_{ij}^{f,h,r}(\overline{h} - h_s)\right)$

$$B^*_{ij} = \frac{1}{2}\left(\bar{Q}^*_{ij}(h_s^2 - \overline{h}h_s) + \bar{Q}^{f,h,r}_{ij}(\overline{h}h_s - h_s^2)\right)$$
$$D^*_{ij} = \frac{1}{3}\left(\bar{Q}^*_{ij}(h_s^3 - 3h_s^2 h + 3h_s h^2) + \bar{Q}^{f,h,r}_{ij}(2h^3 - h_s^3 + 3h_s^2 h - 3h_s h^2)\right)$$

Where, $\overline{h} = 2h$, h_s is the thickness of the SMA layer, and $\bar{h}$ is the total height of the laminate, h is the distance of top and bottom ply from the midplane. It may be noted, the values of these coefficients, whether we consider honeycomb or auxetic ply as the second lamina, remain the same. However, a change in the ABD matrices is observed if the fiber orientation angle is changed.

We can see that equations 5.36 and 5.37 are essentially:

$$\begin{Bmatrix} N \\ M \end{Bmatrix} = \begin{bmatrix} A^* & B^* \\ B^* & D^* \end{bmatrix} \begin{Bmatrix} \epsilon^o \\ \kappa \end{Bmatrix} - \begin{Bmatrix} N^{T^*} \\ M^{T^*} \end{Bmatrix} \tag{5.38}$$

Which is similar to the Turner's Recovery Stress Model [5.2].

5.6 Summary

This chapter forms the foundation of the SMAHC numerical modeling, which will be used subsequently. We understand the effect of temperature and stress on the martensite volume fraction of the SMA, as well as the recovery force generated for a given set of input parameters. We then move to the understanding of embedding these shape memory alloys in composites and the concept of the effective coefficient of thermal expansion, or as we can say, thermal contraction. Since we have also employed the use of honeycomb and reentrant honeycomb (auxetic) cores in our design for anticlastic and synclastic bending, respectively; hence, we also study homogenisation and calculation of effective mechanical properties of these lattices in this chapter. Finally, we have shown a generalised set of governing equations for all the considered SMAHC cases, wherein shear lag is assumed to be not present. The reproduced Brinson model gives us an analytical basis for the dependency of elastic modulus with varying total martensite fraction (plotted in Figure 4.7), thus further explaining the increase in natural frequency of the structure upon the voltage, thereby temperature increase in Chapter 4. Turners model gives us an insight into the modeling of the SMA wires as fibers in a reinforced composite. This allows us to fairly easily numerically model the SMA embedded structures where zero shear lag is an assumption.

The major contribution of this chapter to the thesis is the analytical model, which is then solved numerically. The distinctive characteristic of the constitutive equation is the temperature-dependent compliance matrix and the ABD matrices. This implies that for varying temperature, the stiffness and the extension-bending coupling of the composites also varies. Through these findings, we obtain temperature-dependent Gaussian curvatures upon thermal actuation, which is envisaged to be utilised for shape control in future studies. In the next chapter, we numerically solve our existing set of constitutive equations, validate our model with our experiment, and build a parametric study thereafter.

Chapter 6

Numerical Modeling and Parametric Study

Overview

In this chapter, we build a numerical study for the thermoelastic and free vibration responses of hybrid Shape Memory Alloy (SMA) and E-glass fiber-reinforced composites investigating it using finite element analysis. We consider four composites for analysis and comparison of performances, (1) single layer SMA fiberreinforced hybrid composite (unimorph SMAHC), (2) a two-layer (cross-ply) SMA fiber-reinforced hybrid composite (bimorph SMAHC), (3) single layer SMA fiber-reinforced with a honeycomb core, and (4) single layer SMA fiber-reinforced with reentrant-honeycomb or auxetic core. We analyze thebending response of all the aforementioned composite structures, focusing on the bimorph anticlastic and synclastic bending with negative and positive Gaussian curvatures, respectively. The uniqueness of this part of the thesis is utilizing the shape memory effect of the SMA fibers to achieve active shape control of low-stiffness and lightweight auxetic composite structures. We investigate the free vibration response and analyzed the effect of the fiber volume fraction and the fiber orientation angle on the natural frequency of the system. Further, the role of the reentrant angle and stiffness of honeycomb struts on the overall effective mechanical properties of the ply is also presented. Results confirm the nonlinearity of the parametric combination and the importance of optimization of these parameters for improved Gaussian curvature. The findings are envisaged to be useful for the design of lightweight rigidizable space structures and tensairity structures.

6.1 Specimen Configuration

The numerical simulation in this chapter has been carried out for four cases of SMA fiber-reinforced composite, SMA-based hybrid composite (SMAHC) with a single layer of SMA fiber embedded and the other with two layers of SMA fiber-reinforcement, and SMA based honeycomb and reentrant honeycomb core composites. The motivation behind this investigation is to analyze the bi-directional bending of a SMAHC caused due to the embedding of SMA fibers in offset and actuated through resistive heating. Upon actuation, the layer which consists of SMA fibers tends to shrink, whereas the one without resists this deformation, causing the structure to deflect. When embedded in two layers, at 0°and 90°, and with honeycomb and reentrant honeycomb core, this produces a bi-directional bending. The experimental study on the active SMAHCs is presented in Chapters 3, and 4, and the numerical result is validated against the experimental observation. Figure (6.1) shows the ply arrangement for the cases without a core.

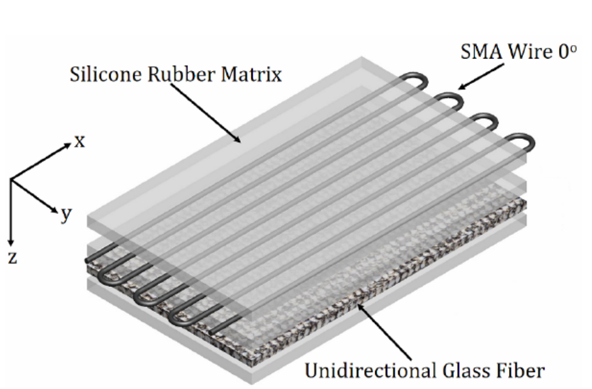

(a) One layer of SMA wire/fiber-reinforcement.

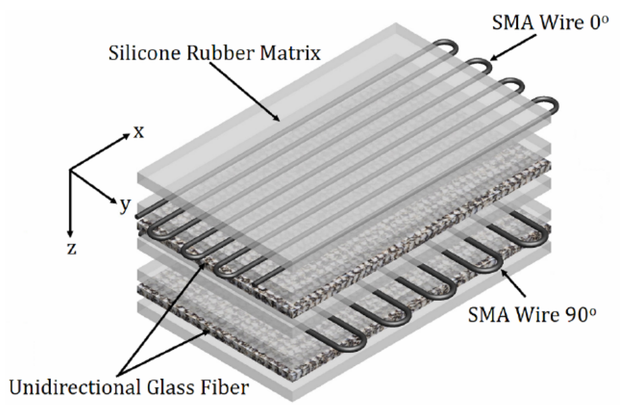

(b) Two layers of SMA wire/fiber-reinforcement.

Figure 6.1: Schematic of SMA wire embedded composite [Srivastava et al. (2018)], SMA is shown digitated as fabricated for experiment.

The properties of the E-glass fiber and the Silicone rubber used in the simulation are specified in Table (2.2). The E-glass fiber was procured from Azo Materials, Asia, and the Silicone rubber, Dragon Skin^{TM} 30, from Smooth-On, Pennsylvania, USA. Using these properties, we compute the equivalent orthotropic properties of the lamina. The requirements to define the behaviour of a composite are- volume fraction of the fiber (V_f), volume fraction of the matrix (V_m), Young's Modulus of the fiber (E_f) and the matrix (E_m), Poisson's ratio of both fiber(ν_f) and matrix (ν_m), density ρ_f and ρ_m, and finally, the coefficient of thermal expansion α_f and α_m. We assume that through vacuum degassing, any voids created due to air entrapment are removed. We calculate the effective mechanical properties of the glass-fiber silicone matrix plies [Table 6.1], honeycomb struts [Table 6.2], and the temperature-dependent SMA-matrix plies [Table 6.3] using rule-of-mixtures and Halpin-Tsai equations as discussed in Chapter 5.

The materials selected are E-glass fiber and Silicone rubber as the matrix. The material selection of the matrix was made considering the elastomeric property allowing large deformation. The fiber volume fraction of E-glass fiber is 0.7, and for the SMA layer volume fraction for SMA fiber is calculated from the previous experiments Srivastava et al. (2018)to be 0.024.

Table 6.1: Equivalent orthotropic material properties for E-glass fiber-Silicone rubber matrix lamina

$E_1(kPa)$	5.04×10^7
$E_2 = E_3(kPa)$	1.126×10^3
$G_{12} = G_{13}(kPa)$	3.77×10^2
$G_{23}(kPa)$	2.8×10^2
$\nu_{12} = \nu_{13}$	0.262
ν_{23}	0.9141
$\alpha_1(/^\circ C)$	4.9×10^{-6}
$\alpha_2 = \alpha_3(/^\circ C)$	7.84×10^{-5}
$\rho(kg/m^3)$	2.14×10^3

Table 6.2: Equivalent material properties for E-glass fiber-Silicone rubber matrix-honeycomb struts

$E_s(kPa)$	6.48×10^7
$G_s(kPa)$	1.13×10^3
ν_s	0.238
$\alpha_s(/^\circ C)$	2.941×10^{-5}
$\rho(kg/m^3)$	2.45×10^3

Table 6.3: Equivalent temperature dependent orthotropic mechanical properties for SMA fiber (NiTiNOL)-Silicone rubber matrix lamina, $E_2 = 3.46 \times 10^2 kPa, G_{12} = G_{13} = 1.162 \times 10^2 kPa, G_{23} = 88 kPa, \nu_{12} = 0.474$**, and** $\rho = 1.2 \times 10^3 kg/m^3$

T (°C)	E_1 **(kPa)**	$\alpha_{11}(/^\circ\mathrm{C})$	$\alpha_{22}(/^\circ\mathrm{C})$
20	6.49×10^5	3.02×10^{-6}	2.44×10^{-4}
22	6.51×10^5	-3.50×10^{-6}	2.43×10^{-4}
25	6.51×10^5	-9.99×10^{-6}	2.43×10^{-4}
27	6.51×10^5	-1.86×10^{-5}	2.43×10^{-4}
30	6.55×10^5	-2.73×10^{-5}	2.43×10^{-4}
32	6.57×10^5	-3.38×10^{-5}	2.43×10^{-4}
35	6.59×10^5	-1.65×10^{-5}	2.43×10^{-4}
37	6.69×10^5	-5.66×10^{-6}	2.44×10^{-4}
40	6.78×10^5	-1.43×10^{-5}	2.43×10^{-4}
43	6.98×10^5	-2.30×10^{-5}	2.43×10^{-4}
45	7.13×10^5	-3.60×10^{-5}	2.43×10^{-4}
48	7.35×10^5	-5.12×10^{-5}	2.43×10^{-4}
50	7.52×10^5	-4.69×10^{-5}	2.43×10^{-4}
53	7.72×10^5	-3.17×10^{-5}	2.43×10^{-4}
55	8.15×10^5	-2.08×10^{-5}	2.43×10^{-4}
57	8.44×10^5	-1.43×10^{-5}	2.43×10^{-4}
60	9.02×10^5	-5.69×10^{-6}	2.43×10^{-4}
61	9.33×10^5	-9.68×10^{-5}	2.43×10^{-4}
62	9.66×10^5	-1.98×10^{-4}	2.39×10^{-4}
63	9.92×10^5	-3.03×10^{-4}	2.36×10^{-4}
64	10.19×10^5	-4.00×10^{-4}	2.34×10^{-4}
65	10.38×10^5	-4.78×10^{-4}	2.32×10^{-4}
66	10.68×10^5	-5.178×10^{-4}	2.31×10^{-4}
67	10.93×10^5	-5.02×10^{-4}	2.31×10^{-4}
68	11.24×10^5	-4.81×10^{-4}	2.32×10^{-4}
70	11.69×10^5	-4.57×10^{-4}	2.33×10^{-4}

Next, we model two bimorphs showing anticlastic and synclastic behavior due to positive and negative Poisson's ratio. The models consist of honeycomb and auxetic cores embedded with SMA fibers at an offset. We calculate the equivalent orthotropic mechanical properties of the honeycomb and auxetic layer using the methods available in the literature [Masters and Evans (1996), Chen and Ozaki (2009)] as explained in Chapter 5. For this analysis we keep the reentrant angle at $+60°$ for honeycomb ply and $-60°$ for auxetic ply. The calculated equivalent mechanical properties of the honeycomb and the auxetic ply are given in Table 6.4.

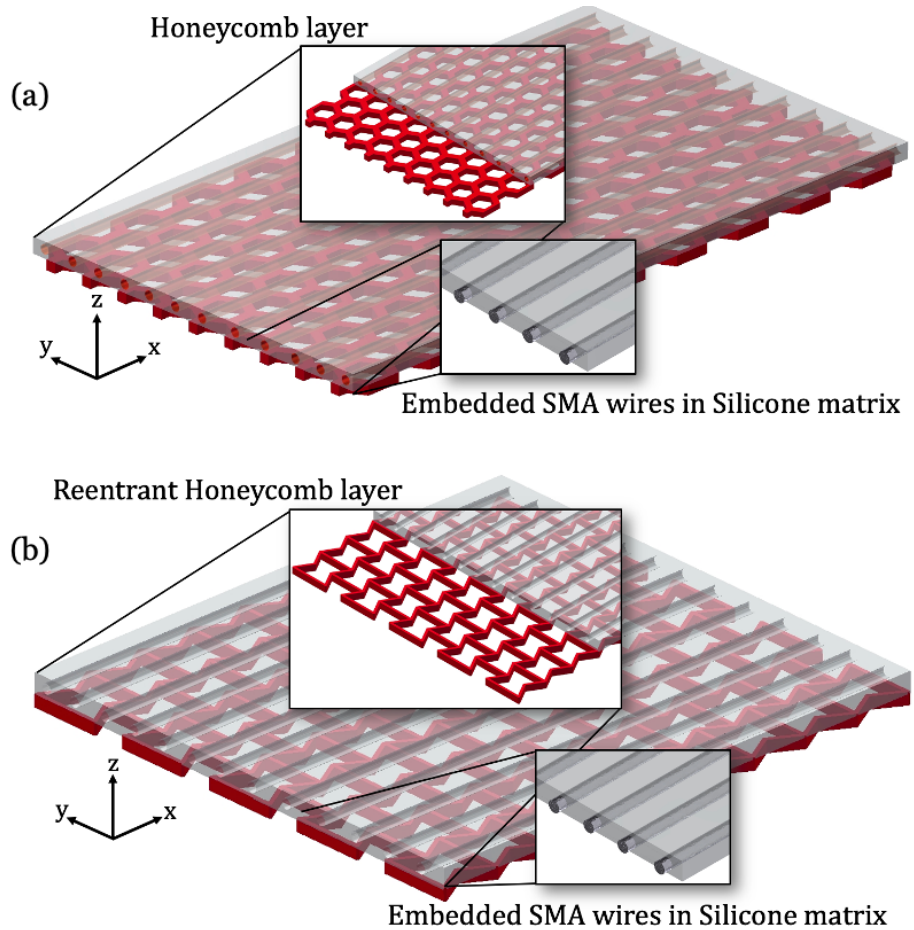

Figure 6.2: Schematic of SMA wire embedded honeycomb ply (positive reentrant angle - positive Poisson's ratio) and auxetic ply (negative reentrant angle - negative Poisson's ratio). (a) Honeycomb layer with SMA wire/fiber-reinforcement, (b) Auxetic layer with SMA wire/fiber-reinforcement; (refer Figure 5.4 for strut details).

The equivalent mechanical properties of the honeycomb and the auxetic layer with respect to varying θ are presented in Section 6.4.1. To maintain a correlation between the constituent materials in the SMAHC and the SMA embedded honeycomb, we consider the material properties of E-glass fiber and Silicone rubber matrix as the constituent materials of the honeycomb struts (as given in Table 2.2), with a fiber volume fraction of 0.9; we also show the effect of volume fraction on the equivalent mechanical properties in the results section. It is assumed that the material properties follow the basic rule-of-mixtures and are as provided in Table 6.2. We let the volume fraction of embedded SMA wires (fibers) be the same as in our experimental work- 0.024.

Property	**Honeycomb Ply**	**Auxetic ply**
$E_1(kPa)$	1.24×10^4	2.56×10^4
$E_2 = E_3(kPa)$	1.38×10^6	6.73×10^5
$G_{12}(kPa)$	4.29×10^2	2.08×10^4
$G_{13}(kPa)$	16.8	34.7
$G_{23}(Pa)$	2.20×10^3	1.03×10^6
ν_{12}	0.084	-0.17
$\alpha_1 = \alpha_2 = \alpha_3(/^\circ C)$	2.94×10^{-5}	2.94×10^{-5}
$\rho(kg/m^3)$	3.27×10^2	6.74×10^2

Table 6.4: Equivalent orthotropic material properties for honeycomb and auxetic ply, strut fiber volume fraction (V_f^h)= 0.9, reentrant angle $\theta^h = 60^\circ$, (refer Figure 5.4 for strut details).

6.2 Finite Element Modeling and Analysis

The static thermoelastic and vibration response analysis for the four sample cases is developed in ABAQUS® with a python command stream. The dimensions of the plate, modeled for numerical analysis, are shown in Figures 6.3(a) and 6.3(b), subjected to fixed-free boundary conditions. We model the SMA wire as fibers, with volume fraction and fiber angle orientation, calculated from our experimental work [Srivastava et al. (2018)]. Using the temperature-dependent attributes, the properties of the plate are defined for both the sample models, a two-ply composite and a four-ply composite. No visible shear in the case of the unimorph despite large deformation (45mm- an average of five) is observed experimentally. This is caused due to the combined binding of the SMA wires and the

E-glass fiber in the matrix, causing the entire structure to behave in a coupled manner. The same fabrication method was repeated in the case of the bimorph with two SMA embedded layers; however, since this case is of small deflection (0.5mm-1mm); thus a rigid body contact between the plies is feasible. Hence, we have not incorporated the failure criteria for capturing delamination in the finite element model and have assumed the perfect interlaminar bond. We have considered rigid-body contact between the adjacent lamina, neglecting delamination and inter-ply shear stresses in the current study. We have previously used woven E-glass fiber for our experimental analysis, and hence, for the FE analysis, we model a woven fabric by aligning two orthogonal unidirectional fiber layers on top of each other, giving the fill and the warp direction 0° and 90° fiber orientation, and sub-dividing the thickness of the woven fabric into two unidirectional layers [Li (1976)].

The standard, linear quad S4R shell element is incorporated to observe the non-linear material response and large deformations, and the meshing is completed through free technique, advancing the front algorithm. S4R element is preferred in modeling sandwich structures wherein through-the-thickness stresses are not necessary to be observed and core crushing is negated. The element size of the fine mesh was controlled to ensure convergence of the solution. Along the longitudinal direction, the plate is fixed at one end and free at the other, and a predefined temperature field is applied in steps- where the steps match with the discrete experimental data points available from the material characterization experiments discussed in Chapter 2. It is also ensured that the results presented are from the martensite-to-Austenite phase transformation region, where the sudden dip in the effective coefficient of thermal expansion is observed- giving it a negative value. The temperature was increased, and the corresponding maximum deflection and natural frequency of the plate in z-direction were recorded. The fiber orientation angle and volume fraction of SMA fiber-reinforcement are varied, and the results are compared.

Since our aim is to attain positive and negative Gaussian curvatures, given the requirement of a torus-shaped structure, hence, next we model the composite with honeycomb and auxetic layer with embedded SMA fibers. We use the equivalent mechanical properties for both the static as well as the temperature-dependent SMA layer, wherein SMA wires are again modeled as fiber reinforcement. We follow the same procedure, and for each temperature increment, we record the deflection and natural frequency of the structure. Since the mechanical properties of the honeycomb layer depend upon the reentrant angle, θ (refer to Chapter 5), hence we conduct this analysis for conventional as well as auxetic, by varying the reentrant angle from $-90°$ to $+90°$. In the second part of the analysis, we apply a linear perturbation to our samples, thus recording the first five natural frequencies for all the sample cases. The complete procedure is shown stepwise in Figure 6.4, and the results are discussed in the subsequent section.

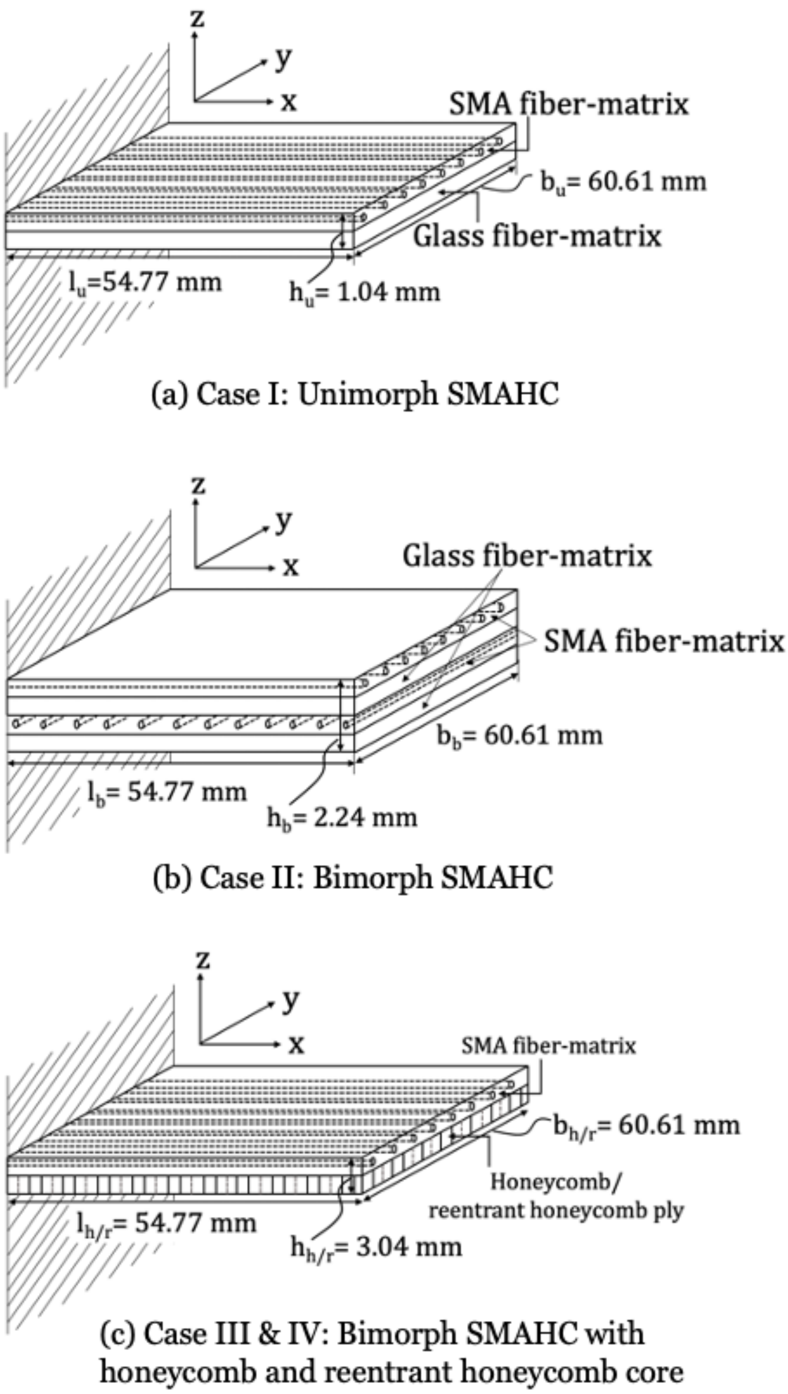

Figure 6.3: Schematic of SMA wire embedded composites- unimorph SMAHC, bimorph SMAHC, and hoeycomb/auxetic plies-laminate configuration and dimensions. (a) A two-ply unimorph with unidirectional SMA, (b) A four-ply bimorph with cross-ply reinforcement of SMA, and (c) A two-ply honeycomb/reeentrant-honeycomb bimorph with unidirectional SMA.

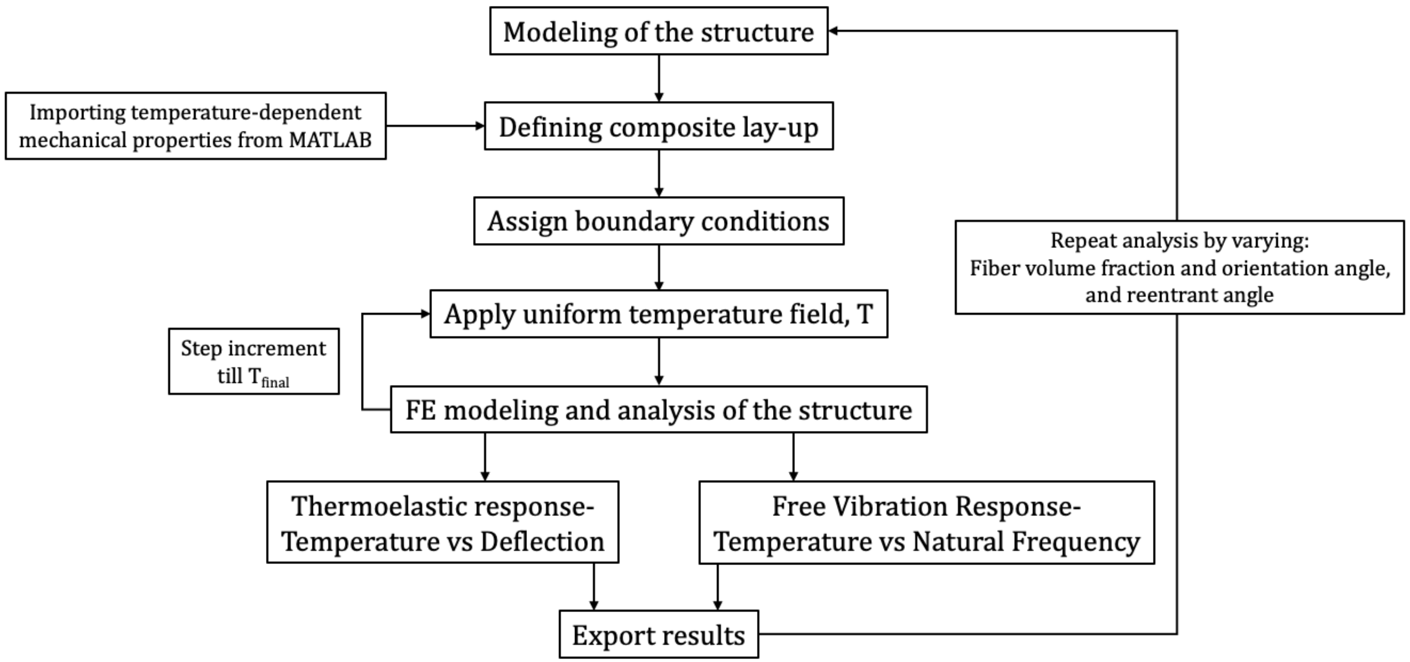

Figure 6.4: Flow-diagram of thermoelastic and vibration response finite element analysis of the SMA embedded unimorph and bimorph SMAHC, and honeycomb & auxetic ply.

6.3 Results and Discussion

6.3.1 Thermoelastic Response

In this section, we present the responses of unimorph and bimorph configurations of SMA reinforced cantilever hybrid composite plates subjected to a pre-set thermal field. Since shape-control is generally a quasi-static process, steady-state is assumed at each thermal state, and deflection of the structures is noted to observe the nature of curvature. Figures 6.5a, 6.5b, and 6.6(a) - 6.6(c) show the nature of deflection corresponding to the applied thermal field. Also, the maximum tip-deflection corresponding to all the cases is noted. We validate our model with the experiment on an SMA embedded unimorph [Srivastava et al. (2018)], the ply layup of the same is shown in 6.3(a). In the experiment, we observe a complete phase transformation and a maximum deflection of an average of 45mm observed over multiple actuation responses. We then model the same in ABAQUS® as discussed in Sections 6.1 and 6.2 and compare the maximum deflection observed upon thermal actuation.

We further build the analysis on our validated model and observe the deflection pattern for bimorphs with positive and negative Gaussian curvatures, as shown in Figure 6.6. It may be observed that upon thermal actuation, the single-layer SMAHC has shown maximum tip deflection (node marked in red), whereas the SMAHC bimorph has shown lower deflection. The addition of a honeycomb reduces the deflection further in comparison to single-layer SMAHC. However, it shows a negative curvature along the longitudinal direction and positive curvature in the transverse direction, giving us a negative Gaussian curvature. On the other hand, the substitution of honeycomb core by auxetic resulted in positive curvature in both directions. A brief summary of all the SMA embedded composites analysed is given in Table 6.5, and the nature of curvature is further analysed in the next section.

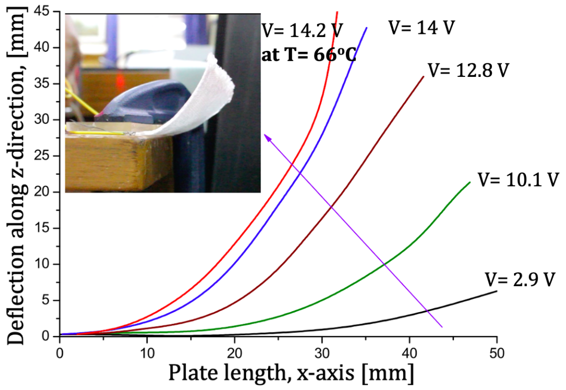

(a) SMAHC unimorph deflection- Experimental observation. The deflection corresponding to voltage, V= 14.2 V at T=66°C is considered for numerical observation.

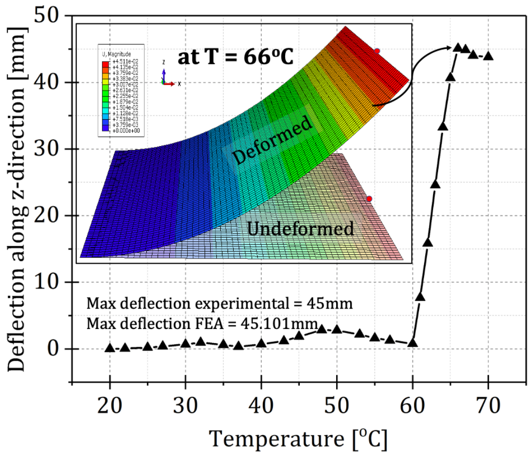

(b) SMAHC unimorph deflection- Numerical observation. The inset image shows the simulated deflection at T= 66°C.

Figure 6.5: Validation of the numerical model against experimental results, SMA fiber volume fraction, (V_f^{SMA})= 0.024, E-glass fiber volume fraction, (V_f^{EGF}) = 0.7, SMA fiber orientation angle, (θ^{SMA})= 0°.

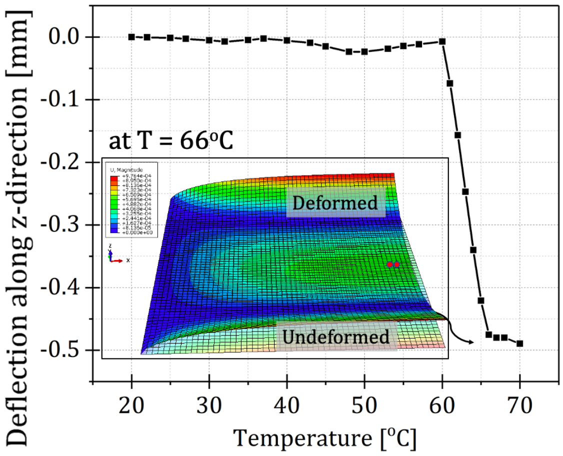

(a) **SMAHC bimorph deflection (two layer SMA reinforcement).**

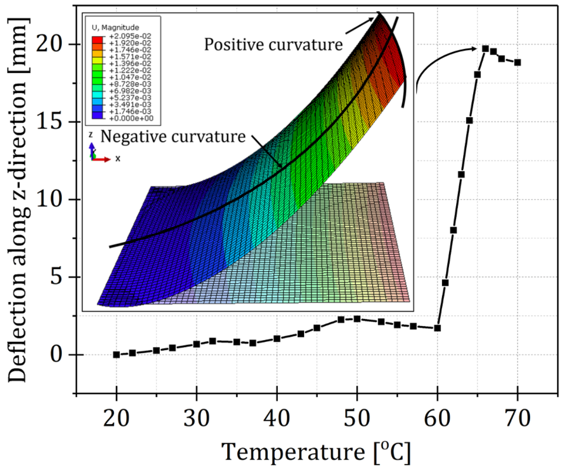

(b) **SMAHC bimorph deflection- SMA embedded honeycomb ply (single layer SMA reinforcement).**

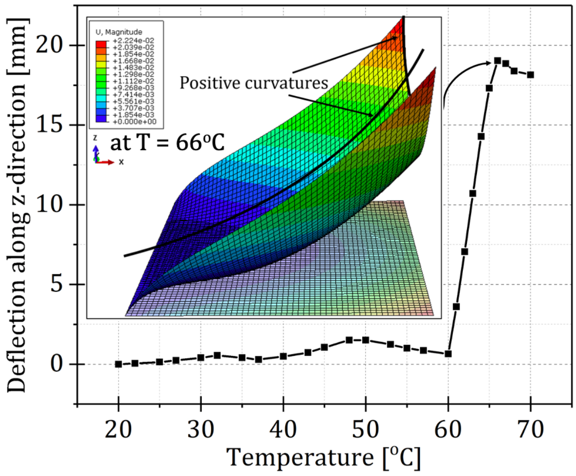

(c) **SMAHC bimorph deflection- SMA embedded honeycomb ply (single layer SMA reinforcement).**

Figure 6.6: Deflection of SMA reinforced bimorph composites upon thermal actuation. $V_f^{EGF} = 0.7$ **(two unidirectional plies orthogonally to model the woven ply),** $V_f^{SMA} = 0.024, \theta^{SMA} = 0°$**, strut fiber volume fraction,** $V_f^h = 0.9, \theta^h = \pm 60°$**.**

6.3.2 Bimorph radius of curvature

To compare the behavior of the three bimorphs studied in this work, it is necessary that we calculate the curvature of the longitudinal and transverse directions of the composite. As can be seen in the previous section that we can achieve a bimorph bending and negative Gaussian curvature through the cross-ply embedding of SMA wires; however, the magnitude of deflection is very low and cannot be utilised for shape morphing and control applications. We utilised honeycomb and reentrant-honeycomb ply to overcome this challenge and noted a manifold increase in the deflection, achieving negative and positive Gaussian curvatures, respectively.

Figure 6.7: Node points for curvature analysis; nodes denote radius of curvature at: $R_c^{x'}$= minimum deflection centerline point, R_c^x= maximum deflection centerline point, $R_e^{y'}$= minimum deflection edge point, R_e^y= maximum deflection edge point.

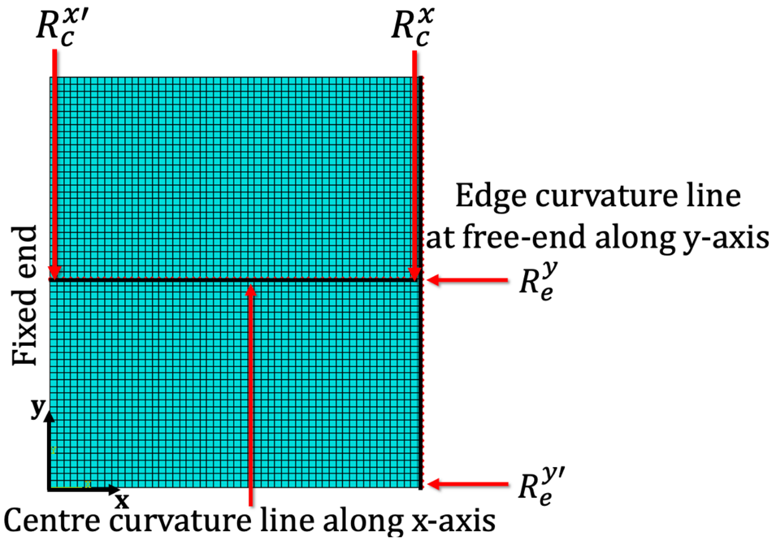

To compare this increased efficiency, we track the deflection of the free end of the cantilever and the centerline along the x-axis for all three cases, as shown in Figure 6.7. The deflections of the nodes are plotted at 66°C where we achieved our maximum tip deflection due to complete phase transformation along with the radius of curvature at the free end and at the maximum dip point of the centerline as shown in Figures 6.8(a) - 6.8(c). The maximum deflection at each node was exported in .xlsx format and plotted in *Origin 2017*. Henceforth, by utilising the *Curvature Radius* application (plug-in to be installed externally) in *Origin 2017*, we can find the radius of curvature at each node selected in the post-processing for analysis. As we can see, the larger the radius of curvature, the lower the deflection of the plate. The curvature lines also give an insight into the synclastic or anticlastic bending of the plates; Figures 6.8(a) and 6.8(c) show the synclastic bending of cross-ply SMA embedded bimorph and unidirectionally SMA embedded in auxetic ply, respectively, whereas Figure 6.8(b) shows the anticlastic bending of unidirectionally SMA embedded in honeycomb ply.

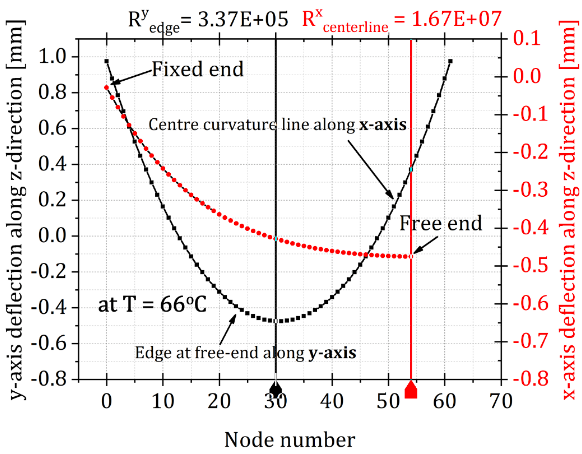

(a) SMAHC bimorph deflection (two layer SMA reinforcement).

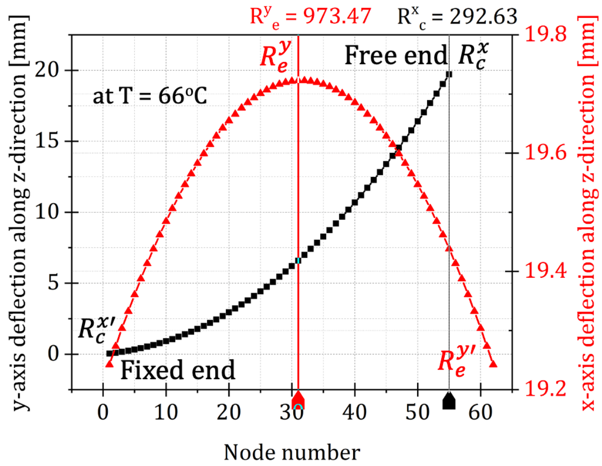

(b) SMAHC bimorph deflection- SMA embedded honeycomb ply (single layer SMA reinforcement).

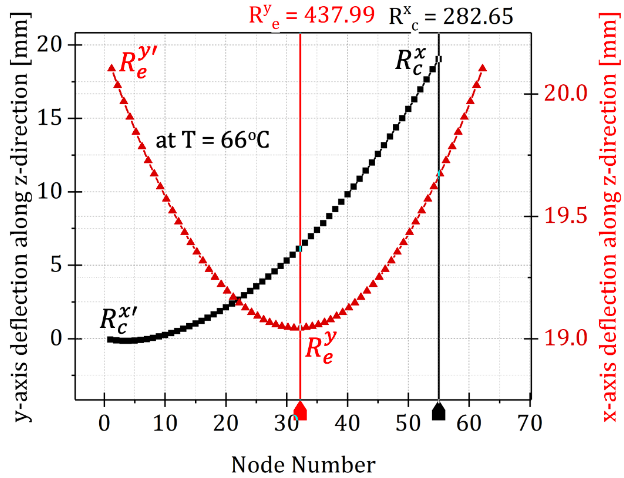

(c) SMAHC bimorph deflection- SMA embedded honeycomb ply (single layer SMA reinforcement).

Figure 6.8: Deflection of SMA reinforced bimorph composites upon thermal actuation. $V_f^{EGF} = 0.7$ **(two unidirectional plies orthogonally to model the woven ply),** $V_f^{SMA} = 0.024, \theta^{SMA} = 0°$**, strut fiber volume fraction,** $V_f^h = 0.9, \theta^h = \pm 60°$**.**

For all the three cases we observed:

$$\left.\frac{R_e^y}{R_e^{y'}}\right|_{GF} = 0.6687\ ;\ \left.\frac{R_c^x}{R_c^{x'}}\right|_{GF} = 10.503;\ \left.\frac{R_e^y}{R_e^{y'}}\right|_{H} = 0.5242;$$
$$\left.\frac{R_c^x}{R_c^{x'}}\right|_{H} = 1.7419;\ \left.\frac{R_e^y}{R_e^{y'}}\right|_{RH} = 0.4922;\ \left.\frac{R_c^x}{R_c^{x'}}\right|_{RH} = 3.2057\ ;$$

where, R_e^y, $R_e^{y'}$, R_c^x, and $R_c^{x'}$ are the radius of curvature of the maximum deflection at the free-end along y-axis, radius of curvature of the minimum deflection at the free-end along y-axis, radius of curvature of the maximum deflection at the free-end along x-axis, and radius of curvature of the minimum deflection at the fixed-end along x-axis, as shown in Figure 6.7. GF, H, and RH denote SMA embedded in cross-ply with glass-fiber-matrix, SMA embedded with honeycomb ply, and SMA embedded in auxetic ply respectively.

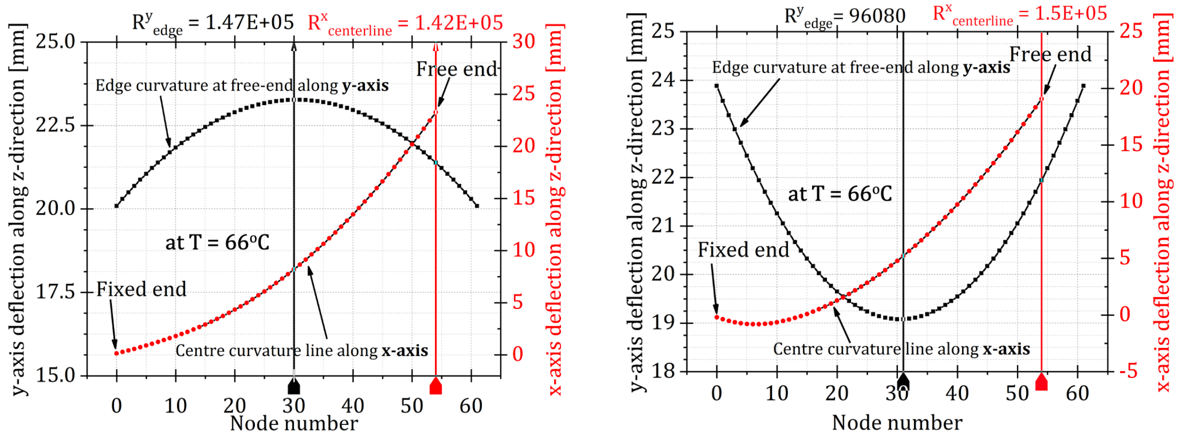

(a) SMAHC bimorph deflection- SMA embedded auxetic ply (single layer SMA reinforcement).

(b) SMAHC bimorph deflection- SMA embedded honeycomb ply (single layer SMA reinforcement).

Figure 6.9: Deflection of SMA reinforced bimorph composites upon thermal actuation. $V_f^{EGF} = 0.7$, $V_f^{SMA} = 0.024, \theta^{SMA} = 0°$, **strut fiber volume fraction,** $V_f^h = 0.7, \theta^h = \pm 30°$.

It was observed that upon varying the volume fraction and the reentrant angle, the curvature response could be enhanced. When considering the fiber volume fraction in the struts to be 0.7 and the reentrant angle to be $\pm 30°$ we achieved a larger edge curvature corresponding to the centerline curvature, as shown in Figures 6.9(a) and 6.9(b). A variation in the radius of curvature ratios was also observed:

$$\left.\frac{R_e^y}{R_e^{y'}}\right|_H = 0.5426; \left.\frac{R_c^x}{R_c^{x'}}\right|_H = 0.4473; \left.\frac{R_e^y}{R_e^{y'}}\right|_{RH} = 0.474; \left.\frac{R_c^x}{R_c^{x'}}\right|_{RH} = 1.875;$$

Laminate configuration	**SMAHC type**	**Max. Tip Deflection**	**Curvature type**
$[0_{SMA}/Woven_{EGF-SM}]$	Unimorph	45.101 mm	Monoclastic
$[0_{SMA}/Woven_{EGF-SM}/90_{SMA}/Woven_{EGF-SM}]$	Bimorph	-0.49 mm	Anticlastic
$[0_{SMA}/60_{H}]$	Bimorph	19.73 mm	Anticlastic
$[0_{SMA}/-60_{R-H}]$	Bimorph	20.11 mm	Synclastic

Table 6.5: Summary of all SMA embedded composites. EGF-SM: E-glass fiber-Silicone matrix, H: Honeycomb ply, RH: Reentrant-honeycomb ply

6.3.3 Free Vibration Response

Next, we carry out the free-vibration analysis of the same set of laminates corresponding to all the four configurations using ABAQUS®. Figures 6.10(a) and 6.10(b) show the modal frequencies for the first ten modes and mode shapes for the first five modes corresponding to the unimorph and bi-morph configurations, respectively. It may be noted that the effect of change in modal stiffness and mass from unimorph to bimorph structure has affected some of the modes significantly. While the mass effect is more predominant in the first two modes and the fifth mode, the third and fourth modes are relatively less affected by the addition of SMA layers. The first four mode-shapes did not change their nature from unimorph to bimorph composition, while the fifth mode is changed from twisting to bending in the case of bimorph structure. The free vibration mode shapes are obtained for 66°C temperature when the SMA is fully transformed. However, the SMA may produce stress-induced phase transformation at this temperature, creating pseudo-elastic damping; we have not considered this in the current analysis.

Another important observation we made was the decoupling of the eigenfrequencies and the corresponding modes in the case of SMA embedded honeycomb ply. The SMAHC unimorph and bimorph and the SMA embedded auxetic ply have their first and second natural frequencies coupled; however, a parametric optimization allows us to decouple the same.

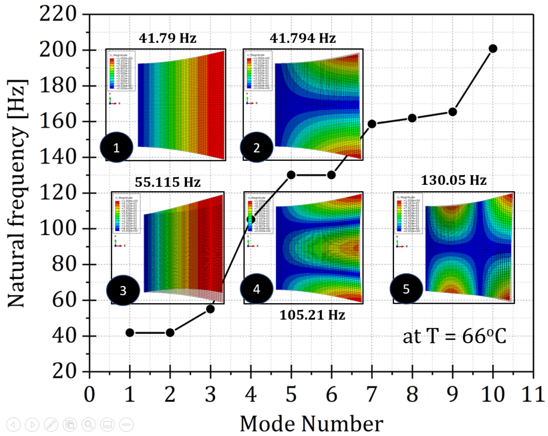

(a) SMAHC unimorph- free vibration response (single layer SMA reinforcement).

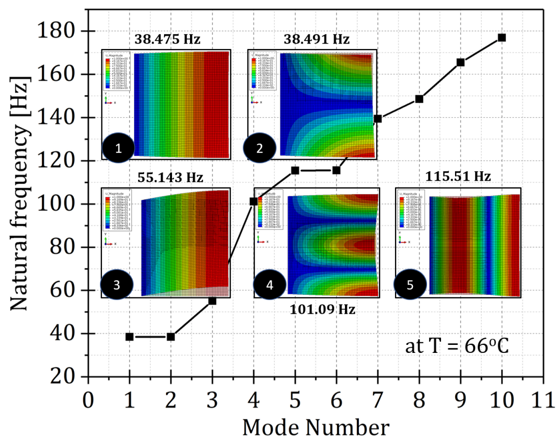

(b) SMAHC bimorph- free vibration response (two layer SMA reinforcement).

Figure 6.10: Free vibration response of unimorph and bimorph SMAHC. Note that the natural frequencies are more widely distributed in the case of unimorph SMAHC (41.79 Hz - 200.916 Hz) in comparison to bimorph SMAHC (38.475 Hz - 176.94 Hz). $V_f^{EGF} = 0.7$, $V_f^{SMA} = 0.024, \theta^{SMA} = 0°$.

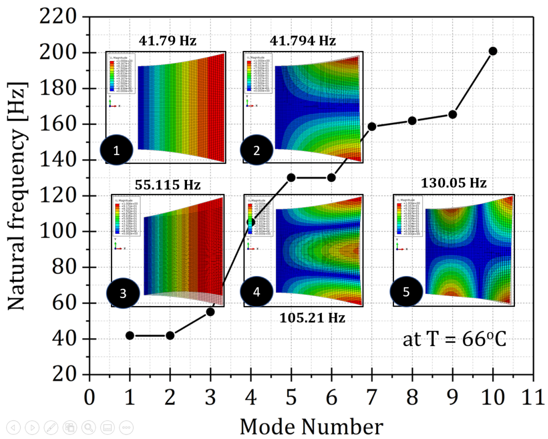

(a) SMAHC embedded honeycomb ply- free vibration response (single layer SMA reinforcement).

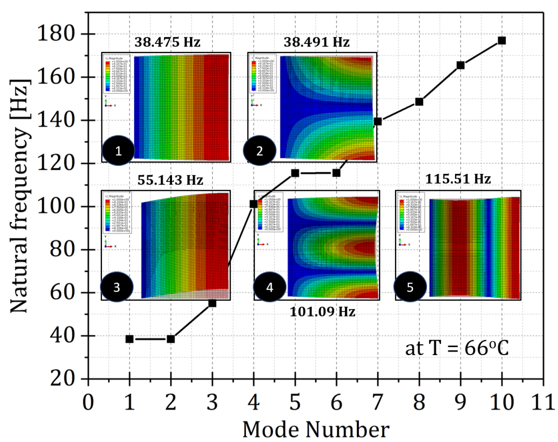

(b) SMAHC embedded auxetic ply- free vibration response (single layer SMA reinforcement).

Figure 6.11: Free vibration response of SMA embedded honeycomb and auxetic ply. Note that for SMA embedded honeycomb and auxetic ply, the first two modes (bending and coupled bending-twisting mode) are widely separated in comparison to all other structures indicating strong decoupling of the fundamental frequencies. $V_f^{EGF} = 0.7$, $V_f^{SMA} = 0.024, \theta^{SMA} = 0°$, **strut fiber volume fraction,** $V_f^h = 0.7, \theta^h = \pm 30°$.

6.4 Parametric study on the Honeycomb/Auxetic core and the SMAHC

6.4.1 Effect of reentrant angle

This section shows the effect of change in various input parameters on the equivalent mechanical properties of the honeycomb ply. As discussed in Section 6.1, each individual strut of the honeycomb lattice cell comprises of unidirectional E-glass fiber-reinforced matrix. The effect of change of fiber volume fraction in the struts, V_f^h, and the reentrant angle, θ^h, on the equivalent in-plane and out-of-plane mechanical properties of the honeycomb ply is given in Figures 6.12 - 6.14.

The in-plane elastic modulus and the in-plane and out-of-plane shear modulus of the honeycomb ply increase with an increase in V_f^h and show almost symmetric behavior about the 0° reentrant angle. However, the curve shows an asymptotic behavior at the reentrant angles- ±90° and 0° for all given V_f^h. We obtained some interesting results when the effect of fiber volume fraction in the strut on the equivalent Poisson's ratio of the honeycomb ply was studied. It can be seen in Figure 6.13 that V_f^h has no effect on the Poisson's ratio, and with the change in the reentrant angle ν_{12} follows a curve resembling hyperbolic cotangent, whereas ν_{21} that of a tangent curve.

6.4.2 Effect of SMA fiber volume fraction and fiber angle orientation

The results showing the effect of change in the volume fraction of the SMA fiber-matrix layer on the maximum deflection along z-direction and the natural frequency of the unimorph SMAHC are discussed in this section. We varied the volume fraction in the vicinity of the experimental SMA fiber volume fraction, which was 0.024. The literature also observed that the volume fraction of SMA wire, when embedded/reinforced in a composite, lies in a similar range. The deflection observed intuitively increases with an increase in SMA fiber volume fraction; however, what we observe here is that the percentage increase in deflection reduces as we go from 0.01 to 0.09 volume fraction as shown in Figure 6.15(a).

Similar behavior is observed in the case of natural frequency; an increase in SMA fiber volume fraction increases the natural frequency of the unimorph, as shown in Figure 6.15(b). Again, the percentage increase in the natural frequency decreases with an increase in SMA fiber volume fraction and approximately remains the same with a change in SMA fiber volume fraction beyond 0.05. This can be correlated with the previous result where the maximum deflection also converges to an approximately similar value of 43.12 Hz beyond 0.05 SMA fiber volume fraction, caused due to a saturation in the compliance of the structure.

Next, for the unimorph, we vary the SMA fiber orientation angle by keeping the SMA fiber volume fraction constant at 0.024, which results in a twist in the structure as we thermally actuate the system. However, the twist is negligible and cannot be utilised for desired applications. We plot the maximum deflection of the chosen point at the center of the edge at the free-end (as shown in Figure 6.5b) and find that the deflection obtained is of maximum -5mm (in the negative z-direction). Despite an increase in temperature, almost static behavior is observed upon varying the SMA fiber orientation angle, caused due to an increase in the stiffness of the structure in the transverse direction and motion resistance due to transversely fixed end, as shown in Figure 6.15c. Through this, we understood that embedding SMA wires at different fiber orientation angles is not an efficient solution for bimorph bending.

A sudden decrease in the natural frequency was observed as the SMA fiber orientation angle is changed from 0° to 90°, interestingly the value of natural frequency remains the same at an average of 23.8 Hz for all orientation angles except 0° as can be seen in Figure 6.15d. This behavior is reflected through the increased stiffness, as previously discussed, for the maximum deflection results with SMA fiber orientation angle variation.

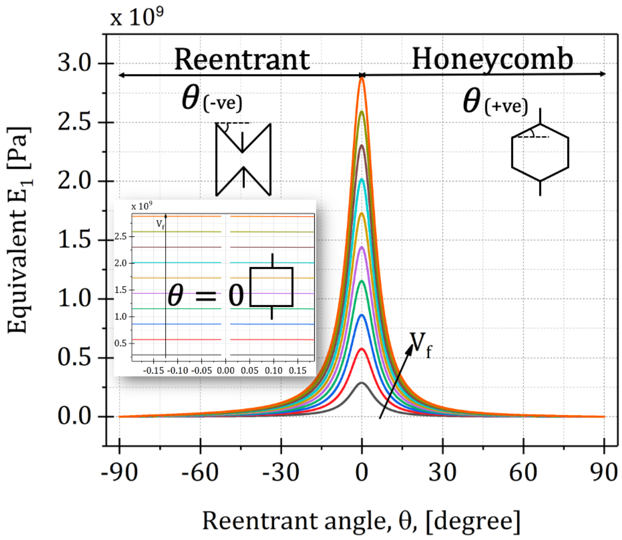

(a) Young's modulus along longitudinal direction (E_1) is plotted for varying strut fiber volume fraction (V_f^h) against change in reentrant angle (θ_h); the stiffness increases with increasing V_f^h.

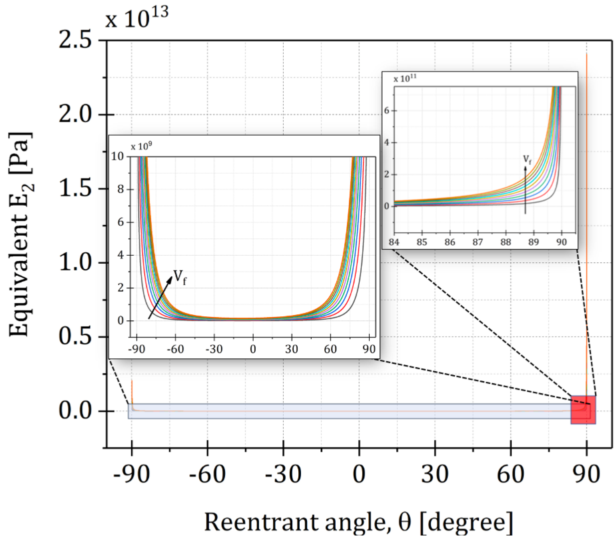

(b) Young's modulus along transverse direction (E_2) is plotted for varying strut fiber volume fraction (V_f^h) against change in reentrant angle (θ_h); the stiffness increases with increasing V_f^h.

Figure 6.12: Effect of strut fiber volume fraction (V_f^h) on the elastic modulus of the honeycomb and the auxetic ply. θ^h increment at 0.01.

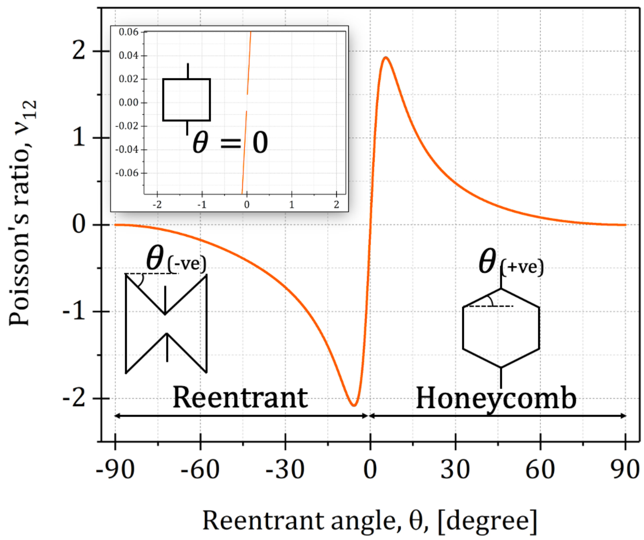

(a) In-plane Poisson's ratio, ν_{12}, is plotted for varying V_f^h against change in θ^h; ν_{12} is unchanged with varying V_f^h and is defined as $\lim_{\theta\to 0}\nu_{12} \approx 0$. The inset image shows the discontinuity as $\theta \approx 0$.

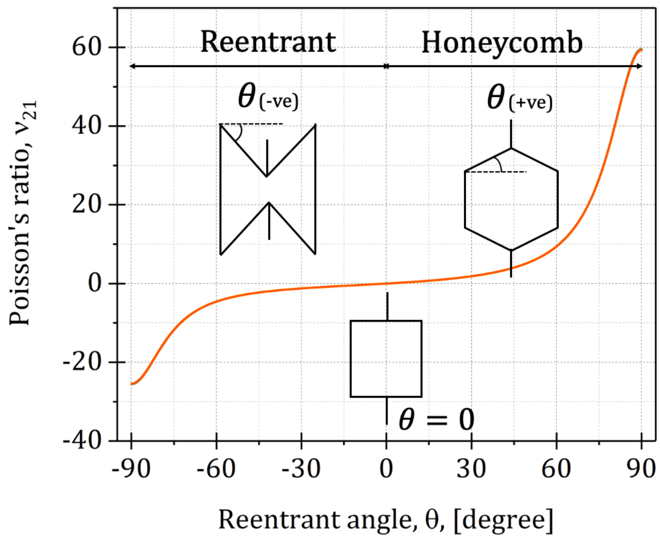

(b) Poisson's ratio in loading direction- 2, ν_{21}, is plotted for varying V_f^h against change in θ^h; ν_{21} is unchanged with varying V_f^h.

Figure 6.13: Effect of V_f^h on the Poisson's ratio of the honeycomb and the auxetic ply. θ increment at 0.01.

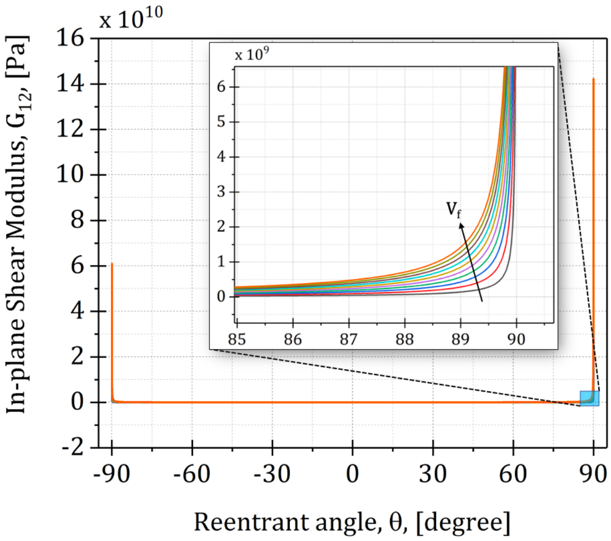

(a) In-plane Shear modulus, G_{12}, is plotted for varying V_f^h against change in θ^h; the shear modulus increases with increasing V_f^h and shows qualitative behavior like transverse Young's modulus.

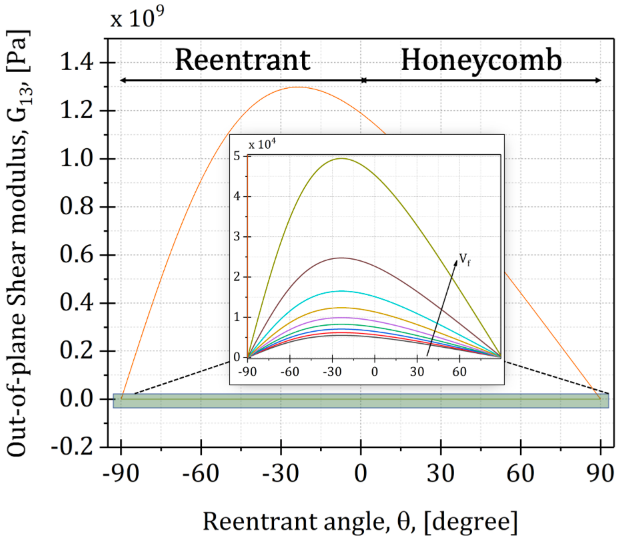

(b) Out-of-plane Shear modulus, G_{13}, is plotted for varying V_f^h against change in θ^h; the shear modulus increases with increasing V_f^h.

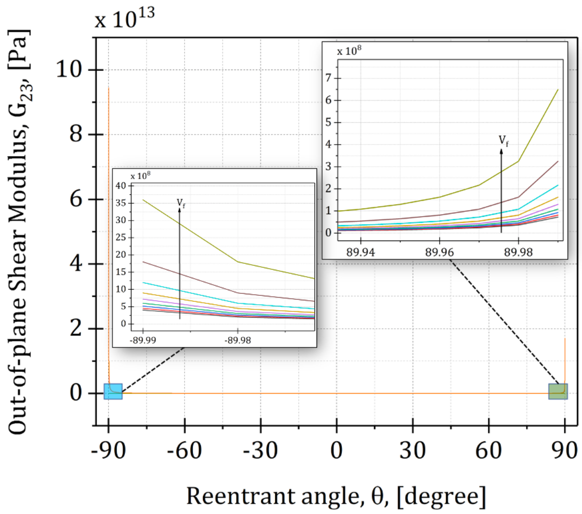

(c) Out-of-plane Shear modulus, G_{23}, is plotted for varying V_f^h against change in θ^h; the shear modulus increases with increasing V_f^h and qualitative behavior is mirror-image of in-plane shear modulus G_{12}.

Figure 6.14: Effect of V_f^h on the shear modulus of the honeycomb and the auxetic ply. θ increment at 0.01.

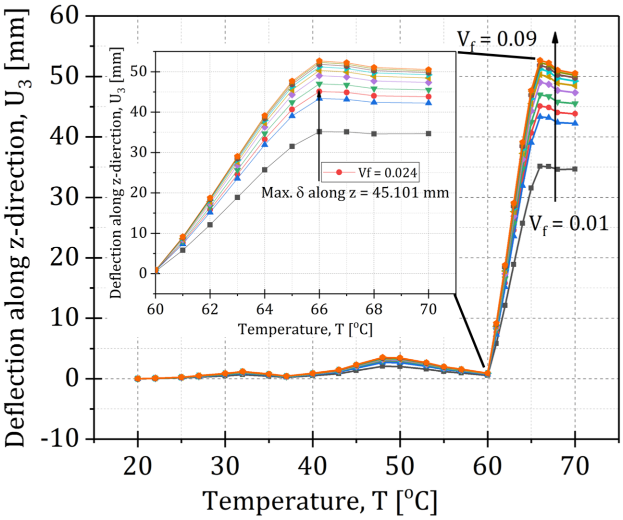

(a) SMAHC Unimorph tip deflection dependance on SMA fiber volume fraction, V_f^{SMA}, (single layer SMA reinforcement); deflection increases with increasing V_f^{SMA}.

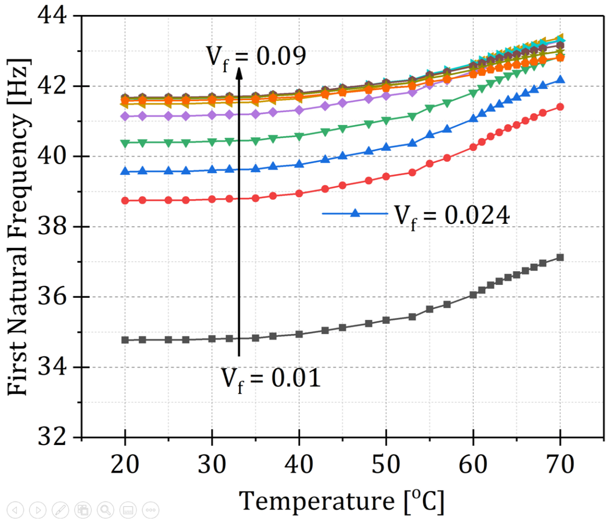

(b) SMAHC Unimorph natural frequency dependance on SMA fiber volume fraction, V_f^{SMA}, (single layer SMA reinforcement); natural frequency increases but soon saturates with increasing V_f^{SMA}.

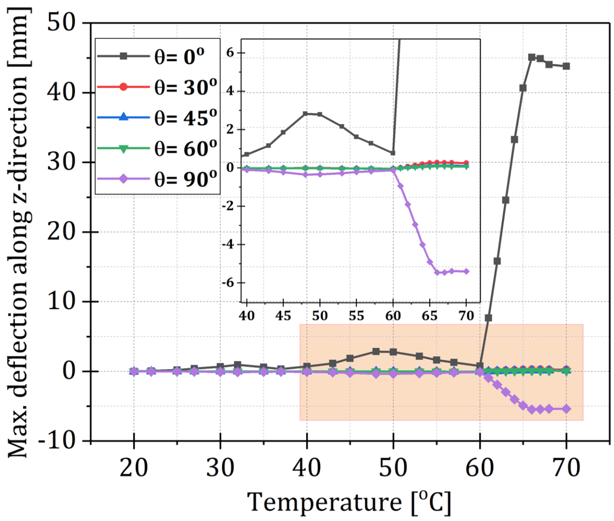

(c) SMAHC Unimorph deflection dependance on SMA fiber angle orientation, θ^{SMA}, (single layer SMA reinforcement); observable deflection is observed at $\theta^{SMA} = 0°$ to $90°$.

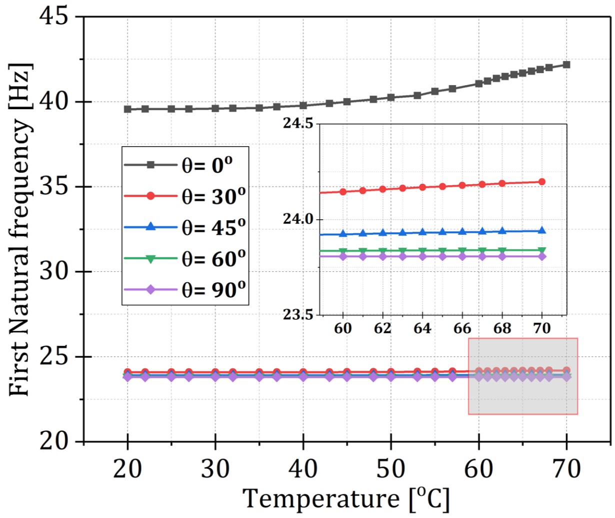

(d) SMAHC Unimorph natural frequency dependance on SMA fiber angle orientation, θ^{SMA}, (single layer SMA reinforcement); natural frequency remains almost the same with change in $\theta^{SMA} = 0°$ to $90°$.

Figure 6.15: Deflection of SMA reinforced composites upon thermal actuation.

6.4.3 effect of volume fraction and reentrant angle of honeycomb constituent fiber

Drawing inferences from the previous section, we do not study the effect of change in the SMA fiber orientation angle and the SMA fiber volume fraction in the case of SMA embedded in honeycomb and auxetic ply. We show here the results for the effect of change in glass-fiber volume fraction in the struts of the honeycomb and hence how the constituents of the struts play a major role in defining the bending behavior of the bimorphs. Here, we consider the same point (point as shown in Figures 6.5 and 6.6) and plot the deflection behavior at $66°C$ temperature where we achieve our maximum deflection, and for reentrant angles $\pm 85°, \pm 60°, \pm 45°, \pm 30°$, and $\pm 5°$, as shown in Figure 6.16a .

Since our constituent materials are E glass-fiber and Silicone matrix, the less the fiber volume fraction, the more deflection along z-direction is observed. However, it is interesting to note that the deflection curve for -85 to +85 reentrant angle forms a fold-like shape, and the deflection pattern is non-linear. For honeycomb plies with 0.1 fiber volume fraction in their struts, the deflection increases from reentrant angle $-85°$ and rises till $-5°$, then starts to decrease in the positive reentrant angle domain. For honeycomb ply, for strut-fiber volume fraction ≥ 0.3, the deflection of the point along z-direction increases till $-30°$ reentrant angle, next, decreases till $5°$, then increases again till $30°$, and finally continuously decreases till $85°$. This nonlinearity is caused due to the effect of change in the mechanical and structural properties of one lattice cell on the equivalent mechanical properties of the entire ply. The maximum deflection of the considered point along z-direction is obtained at 0.1 fiber volume fraction and at $-5°$ reentrant angle of 35.21 mm.

Lastly, we study the effect of fiber volume fraction in the honeycomb struts and the effect of change in the reentrant angle on the natural frequency of the structure. An inverted parabolic curve, almost symmetrical about 0°reentrant angle, is observed. An increase in the volume fraction of the strut fiber essentially increases the overall stiffness of the structure, and hence the natural frequency can be seen increasing with V_f^h. Also, as the reentrant angle approaches $0°$, the honeycomb lattice fundamentally becomes a rectangular lattice; hence, increased stiffness causes a higher natural frequency.

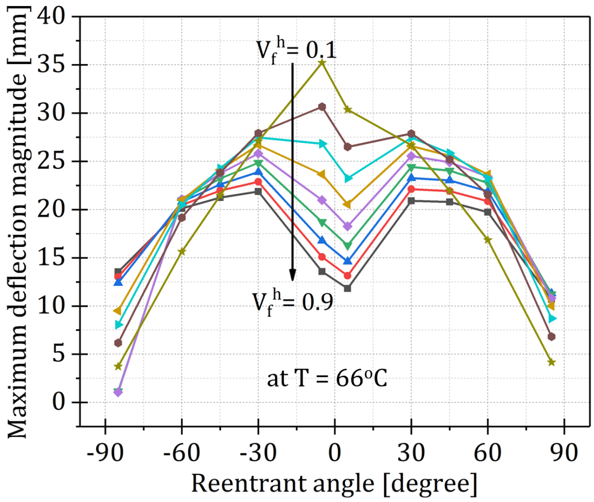

(a) Maximum tip deflection dependance of honeycomb/auxetic bimorphs on strut fiber volume fraction, V_f^h from 0.1 to 0.9 with increments of 0.1, plotted against change in reentrant angle, θ_h; non-linear relation is observed.

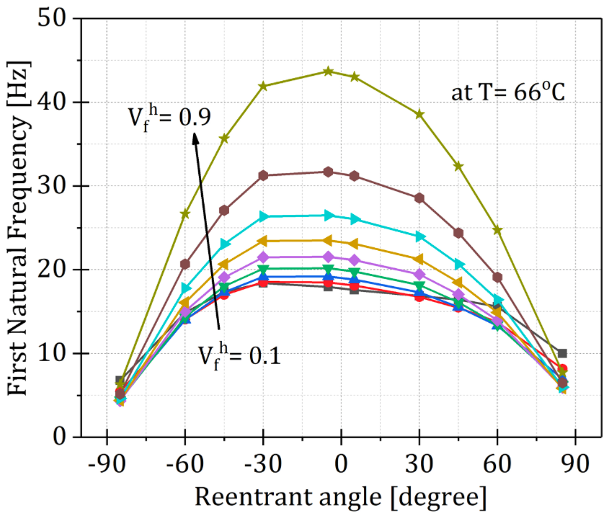

(b) Natural frequency dependance of honeycomb/auetic bimorphs on strut fiber volume fraction, V_f^h from 0.1 to 0.9 with increments of 0.1, plotted against change in reentrant angle, θ_h.

Figure 6.16: Effect of V_f^h and θ^h on the deflection and natural frequency of the honeycomb and the auxetic ply.

A comparison between Figures 6.16a and 6.16b shows the contrasting behavior of the structure; that is, with a higher deflection, a lower natural frequency is noticed and vice versa. As discussed in Section 6.3.3, an optimization study with strut fiber volume fraction and reentrant angle as parametric variables become of interest to obtain the desired deflection with natural frequency within required limits for the new SMA embedded honeycomb and auxetic core hybrid composites.

In the proposed SMA embedded composites with honeycomb and reentrant honeycomb cores with positive and negative Poisson ratios, respectively, the composite demonstrates either anticlastic or synclastic deformation. For a designer, we recommend using a honeycomb core for anticlastic and a reentrant honeycomb core for synclastic deformation. Further, if the Gaussian curvature (product of curvature of the two bending edges) in a bimorph is negative, the response will be anticlastic and synclastic with the positive product.

6.5 Summary

In this chapter, we present the developed Finite Element models for SMA embedded unimorph and bimorph composites. Additionally, we have expanded the model to include honeycomb and reentrant plies. For all these composite structures, the thermoelastic and free-vibration responses are obtained through the numerical solution. The major finding of this work is obtaining the synclastic (positive Gaussian curvature) and anticlastic (negative Gaussian curvature) bending of the composite, generated upon the thermal actuation of the SMA fibers embedded in auxetic and honeycomb core, respectively. The present model also simulates the shape control of the bimorphs by varying input parameters in the given temperature field. The honeycomb and auxetic core significantly improve the deflection of the composite from the bimorph SMAHC, and a decoupling of the first and second eigenfrequencies is also obtained. It is important to note that the mode shapes remain the same with the entire incremental temperature distribution. However, the natural frequencies increase as the stiffness increases with the temperature of the SMA embedded in composites. In the case of unimorph and bimorph SMAHCs, a trade-off between increased stiffness and higher contribution of shape memory effect upon increasing SMA fiber volume fraction is unavoidable. The parametric study in this chapter is a vital foundation for the optimization study discussed in the next part.

The major contribution of this chapter to the thesis is the proposal of SMA embedded composites with honeycomb and auxetic honeycomb core for negative and positive Gaussian curvature, respectively. Not only do the composites demonstrate the intuitive deformation behavior, but their deformation is also found to be efficiently modifiable by varying degrees of SMA volume fraction and SMA fiber orientation. Another major contribution is the parametric study of the SMA embedded composites with honeycomb and reentrant honeycomb core for varying SMA volume fractions. The effect of varying reentrant angles from negative to positive on the deflection and the natural frequency is a unique study and allows us to choose our structure based on SMA variables and the reentrant angles. This broadens our field of research and the scope of optimising the input variables for required outputs.

Part III- Structural Optimization of Unimorph and Bimorph SMA Hybrid Composites (SMAHCs)

Chapter 7

Evolutionary Optimisation and Eigenmode Decoupling

Overview

In Chapter 6, Figure 6.10 we observed that the first and second natural frequencies in the cases of unimorph SMAHC and bimorph SMAHC are coupled. In this chapter, we present the decoupling of the first eigenfrequency corresponding to bending and the second eigenfrequency corresponding to twisting. Unlike most optimisation problems solved for SMAHC vibration, to the best of our knowledge, no literature is found to utilize the Genetic Algorithm to decouple eigenfrequencies by optimising the SMA fiber orientation and SMA ply thickness and minimising the bending eigenmode, and maximising the twisting eigenmode. We implement a methodology that allows us to find a trade-off between the decoupling of the eigenfrequencies as a desirable output and the complex fabrication of optimised design as an undesirable problem. With this methodology, we have an efficiently patterned SMA reinforced composite, which can keep a distinct gap between consecutive eigenfrequencies along with the maximum deflection. The structure has been optimised to perform at the actuation temperature when maximum deflection is obtained upon SMA actuation. The optimisation tool is applied to the structure considering a continuous temperature rise, hence an increase in the eigenfrequency of the model, making our system highly nonlinear.

A complex mode or a combination of two modes at the first natural frequency can cause failure in the structure; hence it is crucial to decouple the eigenmodes in systems. Decoupling of the dominant vibration directions has previously been done in the literature for engine gearbox assemblies. In a multi-body system dynamics where external excitations, as well as the vibrations of the inter-connected structures, may affect the overall natural frequency of the system, actively controlling the vibration response is vital. The algorithm proposed in this chapter can also be used to interchange the eigenmodes of their corresponding eigenfrequencies, thus allowing the first natural frequency to give a twisting or torsional eigenmode and the consecutive natural frequency that of a bending mode. This technique can be used to avoid Phugoid motion-based failure in an aircraft by continuously controlling and interchanging the eigenmodes of its wings.

The next section discusses the four sample cases' numerical modeling for the thermoelastic and the free vibration response analysis. We then compare the results of three optimisation techniques- Multiobjective Particle Swarm (MOPS), Neighbourhood Cultivation Genetic Algorithm (NCGA), and finally, Non-dominated Sorting Genetic Algorithm (NSGA-II), when applied to the unimorph SMA reinforced composite (Case 1) problem. After the comparative study, we validate our model with experimentally obtained results and extend the NSGA-II technique to three more sample cases.

7.1 Optimisation Problem Formulation

In this study, we have modeled four SMA embedded Hybrid E-glass fiber-Silicone matrix Composites (SMAHC), (a) a unimorph with a single layer of SMA reinforcement, (b) bimorph with two orthogonally placed SMA reinforced layers, (c) bimorph with single layer SMA reinforcement with a honeycomb core, and (d) bimorph with single layer SMA reinforcement with an auxetic core. The geometric structures of the smart composites considered in the study are shown in Figure 7.1. The dimensions of the structures are the same for all four samples along the longitudinal and the transverse directions; however, the thickness varies depending upon the number of layers and inclusion of core. The temperature-dependent material properties of the SMA are shown in Figure 2.2b.

The input temperature-dependent material properties are limited to the range of room temperature to 66°C where the maximum dip in the effective coefficient of thermal expansion, α, is observed. The properties of the E-glass fiber (also collated in Table 2.2) are Youngs modulus, $E_f = 72GPa$, Poissons ratio, $\nu_f = 0.21$, and coefficient of thermal expansion, $\alpha_f = 4.9$ x $10^-6/°C$ and the properties of the matrix used as the bonding material are $E_m = 3.38$ x $10^5 Pa$, $\nu_m = 0.49$, and $\alpha_m = 250$ x $10^-6/°C$ (as provided by the suppliers- E-glass fiber- Azo Materials, Asia, and Silicone rubber- Dragon SkinTM 30, Smooth-On, Pennsylvania, USA). The finite element model of the composites is created using a 4-node, quadrilateral S4R element that includes the large-strain formulation with reduced integration. The model is defined as a composite in ABAQUS® by defining the equivalent mechanical properties for each layer, including the SMA layer with temperature-dependent properties. The equivalent properties are calculated using the Lamé's constants and Halpin-Tsai equations as discussed in Chapter 5. A uniform temperature field is applied to each sample individually, and the corresponding deflection of the composite due to offset embedded phase-transformation of the SMA, and hence shape memory effect is recorded. The free-vibration response caused due to linear perturbation is also studied at each temperature step.

We next carry out the multiobjective, single variable optimisation of Case 1 using three different optimisation techniques- Multiobjective Particle Swarm (MOPS), Neighbourhood Cultivation Genetic Algorithm (NCGA), and Non-dominated Sorting Genetic Algorithm-II (NSGA-II) with no constraints at 66°C where the phase transformation of SMA is completed, and the maximum deflection and frequency are observed. We then compare the obtained results and narrow down our technique to one that is then applied to the rest of the sample cases and optimum constraints. In the next section, we will discuss the comparative study results of the three aforementioned techniques.

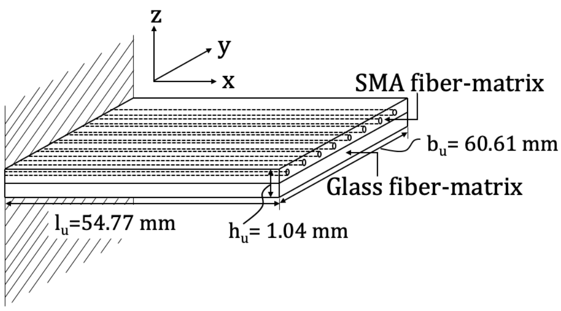

(a) Case 1: A two-ply unimorph with unidirectional SMA

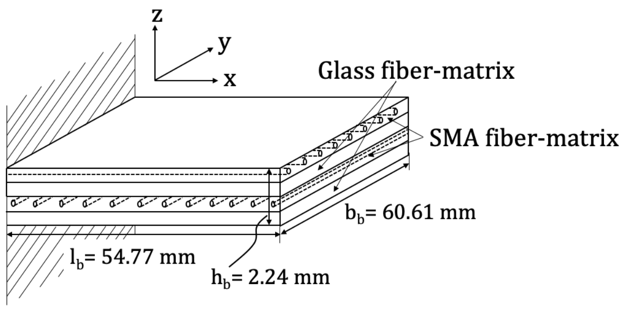

(b) Case 2: A four-ply bimorph with cross-ply reinforcement of SMA

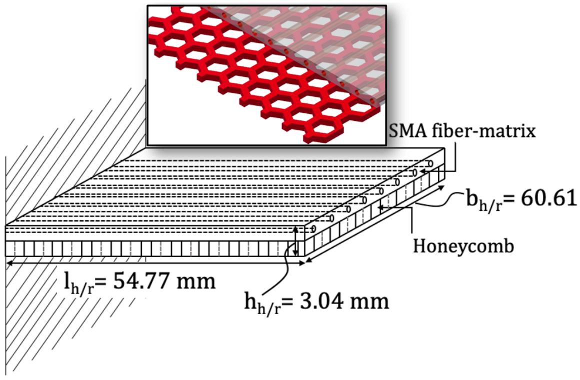

(c) Case 3: A two-ply honeycomb bimorph with unidirectional SMA

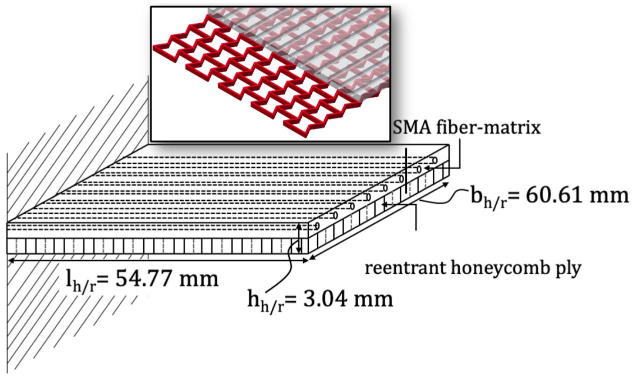

(d) Case 4: A two-ply reentrant-honeycomb bimorph with unidirectional SMA

Figure 7.1: Schematic of SMA wire embedded composites- unimorph SMAHC, bimorph SMAHC, and honeycomb/auxetic core SMAHC- laminate configuration and dimensions (non-optimised).

7.2 Optmisation Technique Comparison Study

The problem is formulated as per the following optimisation function and constraints:

Objective Functions:

$$\begin{aligned} \text{Maximize}: &\quad |EF_2(\theta,t) - EF_1(\theta,t)|^2 \\ \text{Maximize}: &\quad U_{mag}(\theta,t) \end{aligned} \tag{7.1}$$

Variables Bound:

$$\begin{aligned} \text{Variable 1}: &\quad 0^{\circ(L)} \le \theta_i \le 90^{\circ(U)} \\ \text{Variable 2}: &\quad 2.5\times 10^{-4^{(L)}} \le t_j \le 1\times 10^{-3^{(U)}} \end{aligned} \tag{7.2}$$

Where, EF_1 is the first eigenfrequency of the composite beam corresponding to the first bending eigenmode, EF_2 is the second eigenfrequency of the composite beam corresponding to the first twisting eigenmode, θ is the fiber angle orientation, t is the thickness of the SMA ply lamina, and the indices i and j denote the variation of θ and t between the lower and upper bound. The above optimisation problem has two to four design variables depending upon the sample case, three conflicting nonlinear objective functions, and three inequality constraints. Out of the three conflicting objectives, we merge two of them by maximising the difference between minimising first eigenfrequency and maximising the second eigenfrequency, making this essentially a bi-objective optimisation problem.

For solving the above multiobjective shape and vibration control, and eigenmode decoupling problem, an intuitive optimisation approach is presented, in which the MOPS, NCGA, and NSGA-II optimisation techniques are integrated with ABAQUS® for finite element analysis. The population size and the number of generations are varied until convergence is obtained, and the crossover probability is 0.9. This algorithm evaluates the numerous combinations of the SMA fiber orientation (θ) and the SMA ply thickness (t) to find the optimal combination of these parameters. The aim is to decouple bending and twisting eigenmodes, which were observed upon numerical analysis by optimising the thickness of the SMA ply and orientation of the SMA fibers. We simultaneously maximize the deflection behavior making our structure functional for both shape morphing and vibration damping. The temperature field is set to be constant, where it gives maximum deflection, and the next iteration proceeds. ABAQUS® and its sister software iSight® are coupled together, to form a bridge to transfer numerical analysis data from ABAQUS® to iSight® and vice-versa.

Particle Swarm Optimisation (PSO) is a population-based metaheuristic, first proposed by Kennedy and Eberhart (1995). Here *swarm* refers to the population size and a *particle* is an individual member of the *swarm*. For a multiobjective PSO, first, the swarm is initialised, followed by initialising a set of leaders with the nondominated particles from the swarm. Then, for all the leaders, a quality measure is calculated in order to select a leader for each particle of the swarm for every generation, and the flight is carried out. After all the particles have been updated, the leaders' set is updated, and their quality measure is re-calculated.

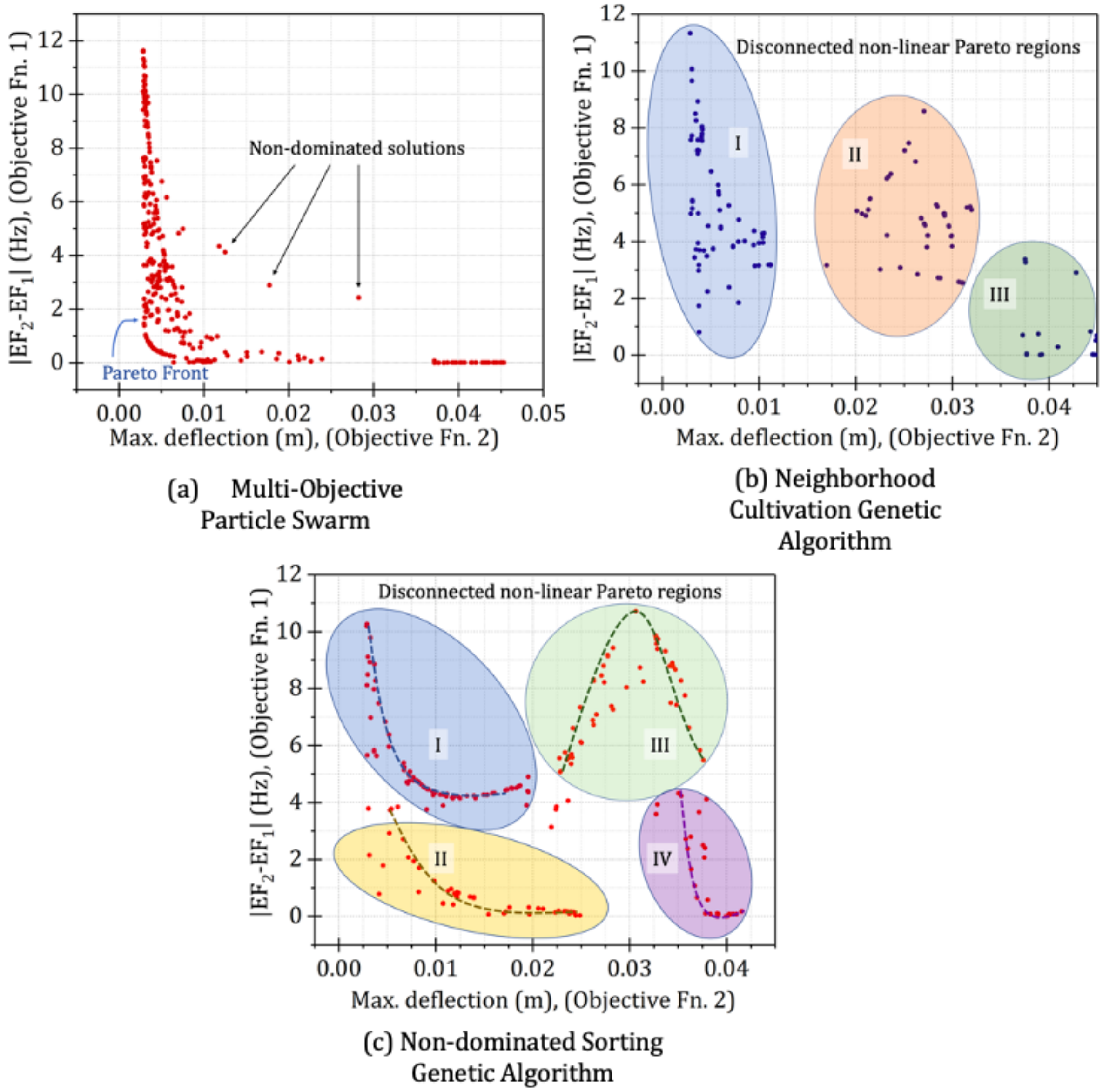

Figure 7.2: Comparison study of MOPS, NCGA, and NSGA II algorithm when no constraints are proided. The desired optimised design parameters lie in Section III of NSGA-II results as show in the figure. The selection and application of constraint is based on the NSGA-II results.

In the Neighborhood Cultivation Genetic Algorithm (NCGA) technique [Kalyanmoy (2001)], all objective parameters are treated separately, and the standard genetic mutation and crossover operation are performed. The crossover process is formed on the 'neighborhood cultivation' mechanism, where mostly between individuals with values close to one of the objectives, the crossover is performed. Whereas NSGA-II [Deb et al. (2002)] produces offspring's using a particular type of crossover and mutation where according to nondominated-sorting and crowding distance comparison, the next generation is picked.

We first evaluate the possible combinations without constraining our system, and based on the results, we constrain our system and obtain the Pareto-Optimal front. Following are the sequence of steps in the NSGA-II optimisation algorithm:

1. Setting the NSGA-II parameters- population size, crossover probability, and a number of generations.

2. Initialising the population.

3. Deciding the SMA fiber orientation angle and the SMA layer's thickness from the lower and upper bound values of the design variables for each population member. For the current study, the SMA wires are modeled as reinforced fibers for the finite element analysis (FEA).

4. The FEA is carried out for each population member to obtain the deflection and natural frequency within the given temperature range in ABAQUS.

5. The obtained values are substituted back via the Simulink bridge in iSight® into the NSGA-II algorithm.

6. Evaluation of the objective function and the values of the constraints.

7. Performing nondominated sorting of the population and assigning front-ranking.

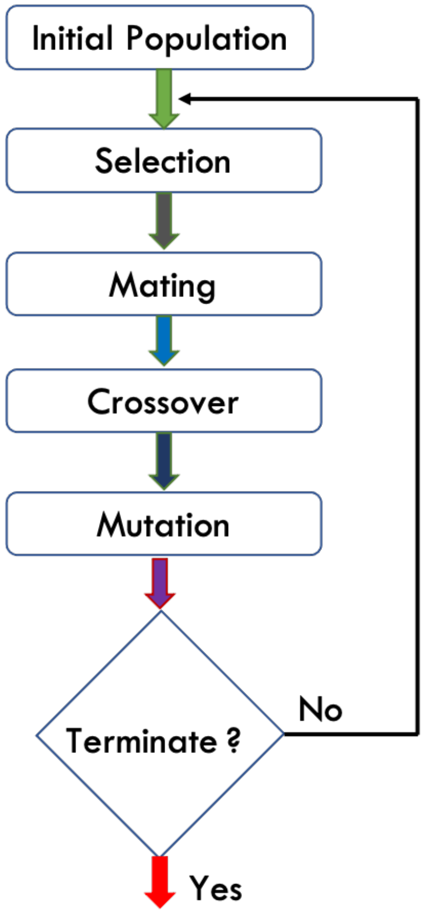

Figure 7.3: Basic structure and sequence of the evolutionary algorithm

Further steps of the algorithm follow the generic steps of the optimisation problem, such as creating offspring using selection, crossover, and mutation operators, combining parent and offspring population, calculating the crowding distance, and replacing the previous parent population with the updated child population. Finally, until the defined number of generations is reached, we reiterate the steps for the succeeding generation.

The results of the three techniques with the same set of objective functions and variables are shown in Figure 7.2. As can be seen, MOPS gives us a convex Pareto Optimal Set, and the NCGA and NSGA-II give us disconnected Pareto Optimal sets. However, to maximize both our objective functions, we need a technique that can give us a non-convex Pareto Optimal set. The desired set of solutions was found in Region- III of the NSGA-II Pareto solutions; we then constrain our problem accordingly to achieve the non-convex set of solutions discussed in the next section.

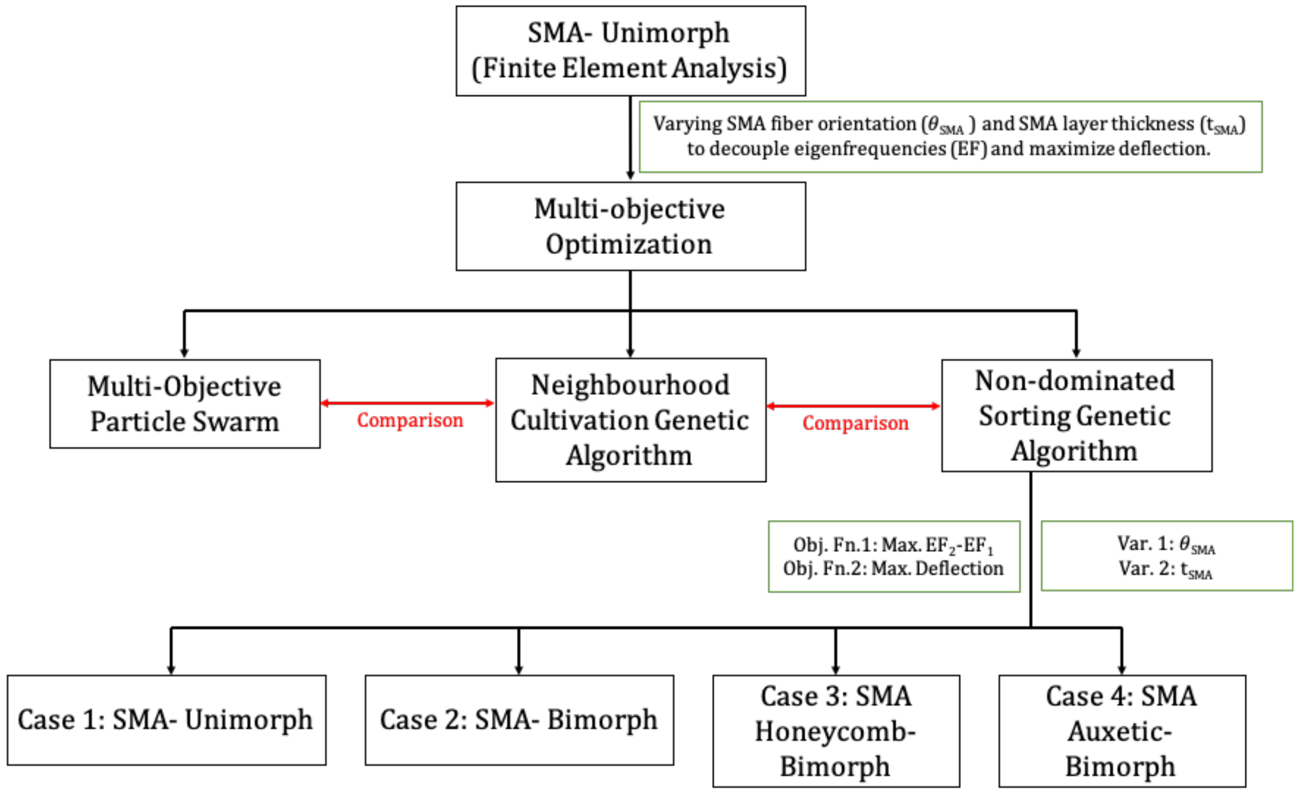

Figure 7.4: Flow-diagram explaining the steps for the finite element modelling of the SMAHC cases- multi-objective optimisation comparison, objective functions, and variable constraints.

7.3 Results and Discussion

7.3.1 Case 1: SMA unimorph

In this case, we consider the SMAHC with a single layer of SMA reinforcement. Since the SMA is embedded at an offset (refer Figure 7.1a), upon thermal actuation, the phase transformation in the SMA causes it to contract to its parent Austenite state, and the entire structure gives bending along the z-direction. We can intuitively observe that the maximum deflection will be obtained in this case when the SMA fibers are oriented along with the composite's longitudinal direction. We first get the Pareto-optimal solutions for the single objective optimisation problem by varying the SMA fiber orientation angle with 0°and 90°as lower and upper bound, respectively.

As shown in Figure 7.5 maximising the deflection, minimising the bending mode or the first eigenfrequency, and maximising the twisting mode or the second eigenfrequency gives an intuitive result. An increase in fiber orientation angle, θ, and the thickness of the SMA ply, t, gives the highest deflection at the minimum in orientation angle and at an optimised almost center in the case of thickness. In case of the minimisation of the first natural frequency corresponding to bending mode, minimum frequency was obtained at increased SMA fiber orientation angle and decreased SMA ply thickness; whereas in case of maximisation of the second natural frequency corresponding to twisting mode, the maximum frequency is obtained at decreased orientation angle and increased ply thickness. Hence, due to the contrasting behavior of the system, multiobjective optimisation of the same is vital.

The finite element solution for this case with 0°θ produces a maximum deflection in the structure of 45.101 mm. We validate our result with our experimental observations wherein a unimorph SMA-reinforced composite is fabricated with the given dimensions and material properties. An average of 45mm deflection was observed in our structure upon complete phase transformation of the SMA, as shown in Figure 6.5. The validation of the numerical analysis has been discussed in Chapter 6.

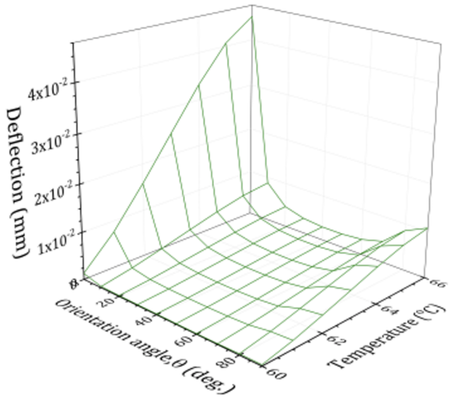

(a) SMA fiber orientation angle vs Maximum deflection vs Temperature

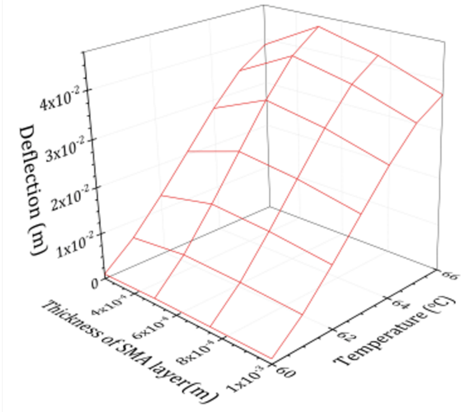

(b) SMA ply thickness vs Maximum deflection vs Temperature

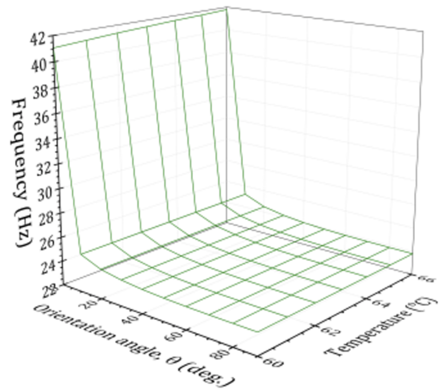

(c) SMA fiber orientation angle vs First eigenfrequency vs Temperature

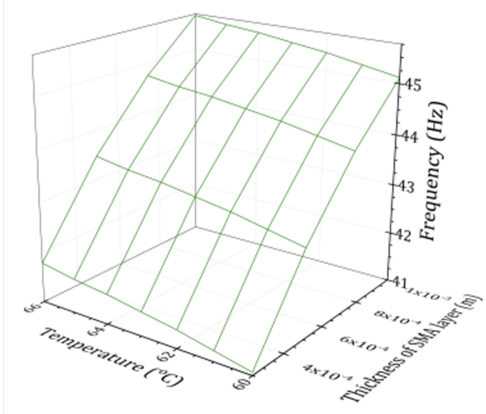

(d) SMA ply thickness vs First eigenfrequency vs Temperature

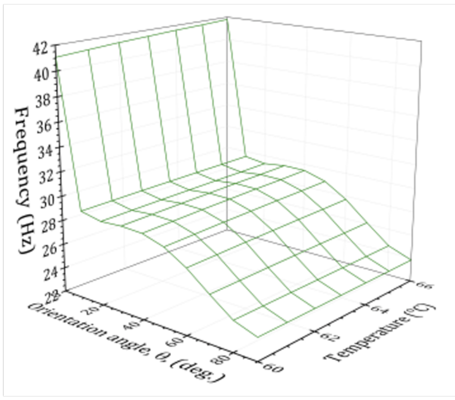

(e) SMA fiber orientation angle vs Second eigenfrequency vs Temperature

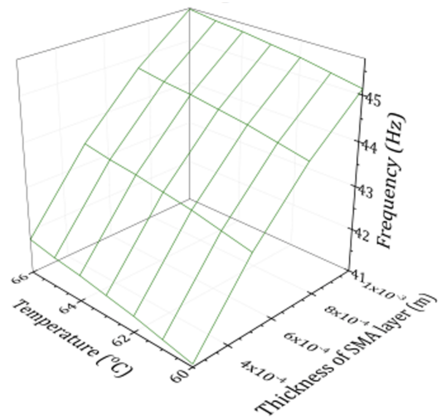

(f) SMA ply thickness vs Second eigenfrequency vs Temperature

Figure 7.5: Single objective opmisation of the SMA unimorph for maximising deflection 7.5a, and 7.5b, minimising first eigenfrequency 7.5c, and 7.5d, and maximising second eigenfrequency 7.5e, and 7.5f.

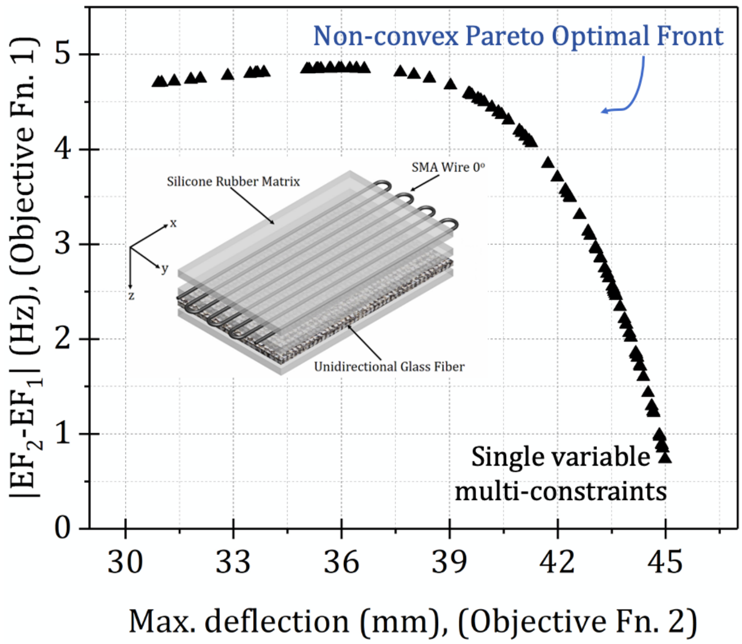

Figure 7.6: Pareto Optimal Curve for the unimorph SMAHC sample case (Case 1), single variable- θ with deflection and decoupling bounds.

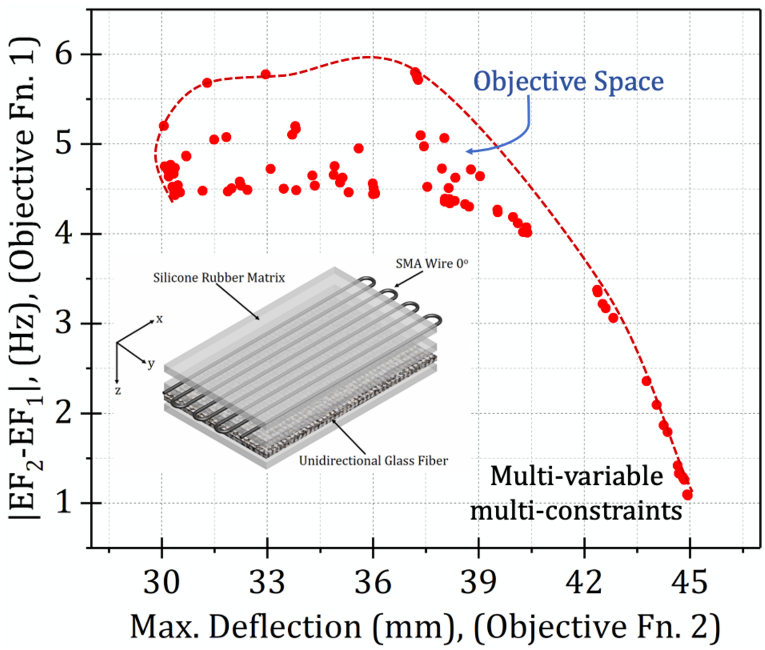

Figure 7.7: Pareto Optimal Curve for the unimorph SMAHC sample case (Case 1), multi-variable- θ and t, with deflection and decoupling bounds.

We also give a linear perturbation to our structure to analyze its dynamic response. Here, we observe numerically that both the first and the second natural frequencies are at 41.79Hz, and the corresponding eigenmodes are symmetric-out-of-plane bending and twisting, respectively. This makes our system chaotic as we will observe two modes at the same frequency resulting in a complex mode. Hence, we decouple the frequencies by minimising the first and maximising the second natural frequency. The results corresponding to the decoupling of frequencies and maximising the deflection are shown in Figure 7.6.

We further observed that by a considerable change in the θ we were able to extract a twist from the structure; however, by slightly changing the orientation angle to 1.43°from 0°, we were able to get almost get a 5Hz of frequency decoupling with a slight reduction in bending performance to 37.20mm from 45.101mm (refer to Table 7.1).

We then carried out the same set of steps with both SMA orientation angle and SMA layer thickness as variables and constraining our system to get a minimum of 30mm of deflection. In this case, we get a set of Pareto-optimal solutions and an objective space, as shown in Figure 7.7. In this case, we can slightly increase the deflection by almost 2mm by keeping the orientation angle the same as obtained in the single-variable case and reducing the thickness by 0.03mm. A larger objective space allows us to choose our input variables for even more sophisticated and accurate results. The non-convex Pareto-optimal Solution that is obtained does not give linear relation of the variation in θ_{SMA} and t_{SMA}. The multiobjective optimisation problem, as stated in the previous section is solved using the proposed integrated iSight-ABAQUS optimisation formulation. The computation time for solving this problem on an Intel Core^{TM} i7 processor computer was around 20 hours.

7.3.2 Case 2: SMA bimorph

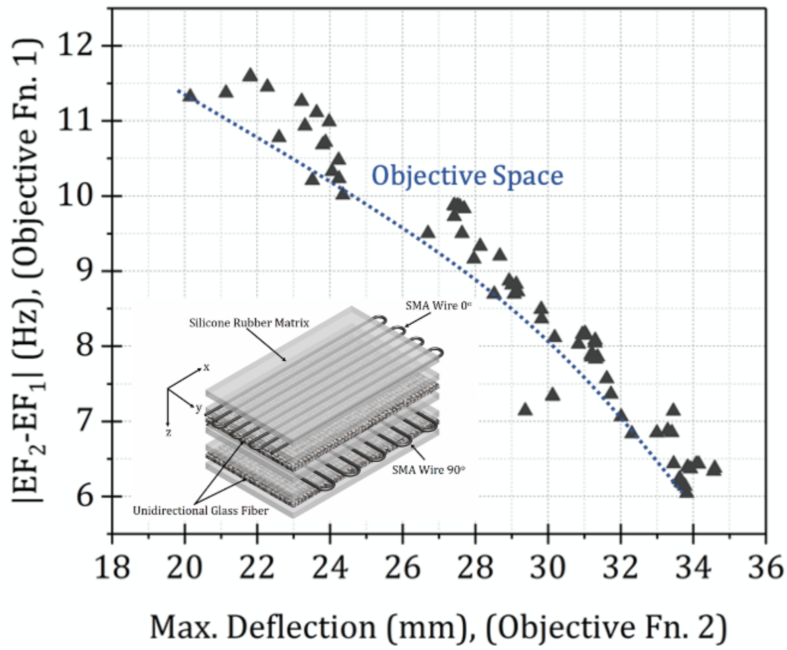

Figure 7.8: Pareto Optimal Curve for the bimorph SMAHC sample case (Case 2), multi-variable- θ and t, with deflection and decoupling bounds.

In the second case (refer to Figure 7.1b), the maximum deflection obtained from our structure when analysed numerically is 0.5mm in the opposite direction. This reduction in bending is caused due to orthogonal placement of SMA fibers causing a bending constraint to each other. However, by changing the SMA fiber orientation angles for both the plies, we experience a twist in the structure with subsequent decoupling of the modes. Hence, the decoupling of the modes, in this case, was obtained at the expense of considerable twisting in the structure. The high amount of twist gives a large deflection along the z-direction; the applications with the given ply lay-up are confined to domains where twisting of the structure is either required or can be neglected.

7.3.3 Case 3: SMA bimorph with honeycomb core

In this case, the SMA fibers are placed along the longitudinal direction of a honeycomb core. The honeycomb core gives the structure a saddle-shaped deflection caused due to the contraction in the SMA upon temperature increase. This bimorph deflection behavior can be utilised where the active shape morphing requires an overall negative Gaussian curvature. Similar to the previous cases, a significant difference in the SMA fiber orientation angle from 0°can cause a significant twist in the system. Hence, to maintain a bimorph bending without noticeable twisting with the decouple natural frequency, we select the Pareto-optimal solution with the least θ variation. The saddle shape is a limiting case of the inner surface of the Torus structure. Shape control of such skewed composites is useful in applications like controlling the shape of the airfoil and torus-like structures.

7.3.4 Case 4: SMA bimorph with auxetic core

Lastly, we apply the NSGA-II optimisation to the SMA reinforced bimorph with the reentrant-honeycomb (auxetic) core. The SMA fibers are placed along the longitudinal direction of the auxetic core and thermally actuated. The maximum deflection and the first and second eigenfrequencies are recorded after the SMA phase transformation. The optimising technique is applied at this temperature to maximize the deflection and the second eigenfrequency and minimize the first eigenfrequency, thus decoupling the two frequencies. Similar to previous cases, as we maximize our decoupling, we experience a twisting in the structure; however, keeping the θ variation between 0°to 90°keeps the twisting minimal with considerable decoupling. Figure 7.10 gives the Pareto Optimal set of solutions for this case where a large amount of decoupling can be seen as the structure experiences twisting. Table 7.1 shows the shift in the deformation and eigenfrequency data with a slight change of θ from 0°to 0.85°.

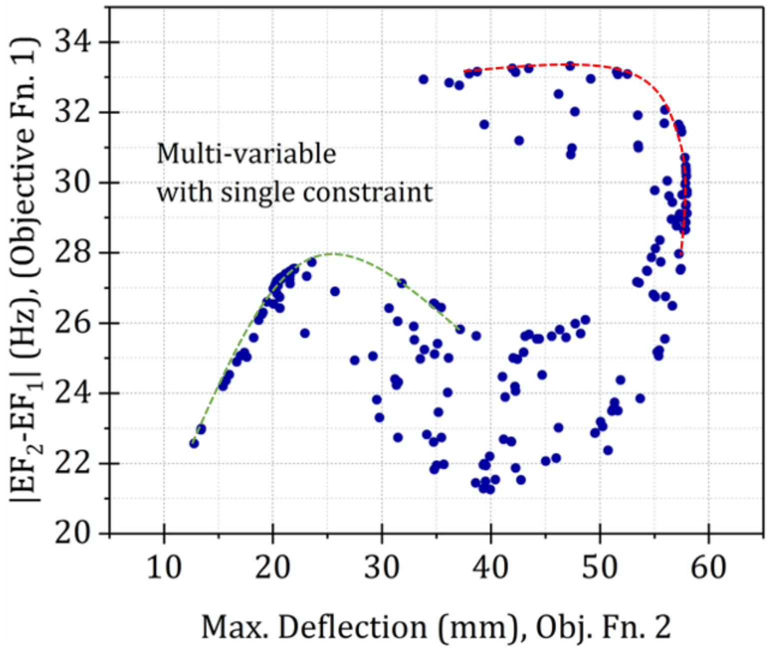

Figure 7.9: Pareto Optimal Curve for the bimorph SMAHC with honeycomb ply sample case (Case 3), multi-variable- θ and t, with only deflection bounds.

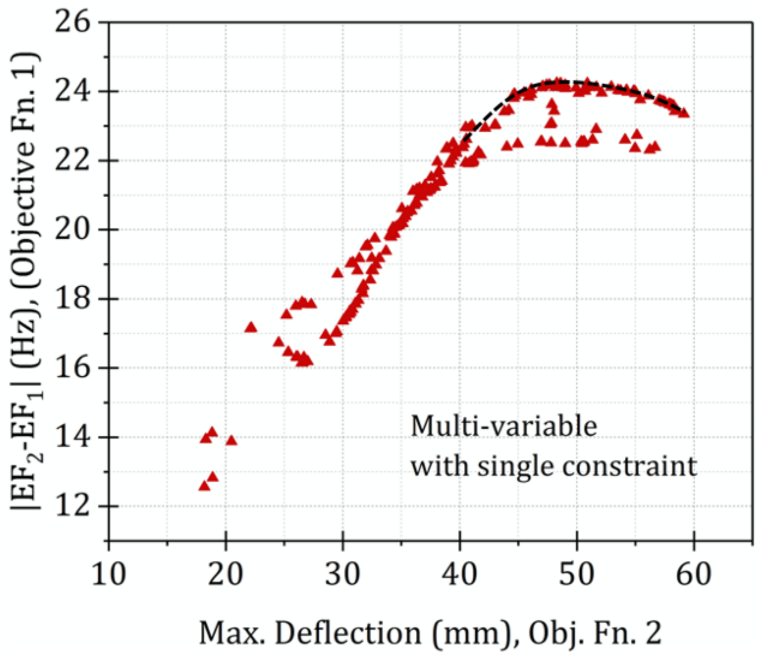

Figure 7.10: Pareto Optimal Curve for the bimorph SMAHC with reentrant-honeycomb ply sample case (Case 4), multi-variable- θ and t, with only deflection bounds.

Case no.	Non-Optimised / Optimised	Deflection (along z-direction) mm	First Eigenmode (Bending) Hz	Second Eigenmode (Twisting) Hz
1	θ= 0° t= 0.54mm	45.10	41.79	41.79
	θ= 1.43° t= 0.61mm	37.20	38.02	43.82
2	θ_1= 0° θ_2= 90° t_1= 0.54mm t_2= 0.54mm	-0.49	38.47	38.49
	θ_1= 10.8° θ_2= 40.4° t_1= 0.97mm t_2= 0.97mm	27.7	36.10	45.93
3	θ= 0° t= 0.54mm	19.73	24.73	75.38
	θ= 0.18° t= 0.5mm	20.36	24.54	51.74
4	θ= 0° t= 0.54mm	20.11	26.67	40.29
	θ= 0.85° t= 0.63mm	19.68	26.53	39.71

Table 7.1: Optimised vs non-Optimised deflection and eigenfrequencies for the four sample cases.

7.4 Summary

In this chapter, we have presented the comparative study of MOPS, NCGA, and NSGA-II optimisation techniques for a multi-variable SMA reinforced composite showing unimorph bending upon SMA thermal actuation. Subsequently, we have carried out three optimisation studies corresponding to the maximisation of compliance and fundamental natural frequencies in bending and torsion. This is further treated as multiple objective problems to maximize the deflection of the unimorph and separating the band gap between bending and twisting mode. The active shape and vibration control, as well as the eigenmode decoupling, is formulated as a multiobjective optimisation problem. An algorithm has been proposed based on population eigenmodes used to evaluate the variable bounds of the objective functions. The convergence of the obtained Pareto Optimal solution is validated by comparing it with single-objective solutions of the same problem. The successful validation of the finite element model against the experimental response values as shown in Chapter 6 is also discussed here. The optimisation study concludes the research work under the domain of this dissertation. The disconnected Pareto regions found in this study can be utilised to choose our variable bounds and functional constraints if any, depending upon the optimisation function.

The major contribution of this chapter to the thesis is the decoupling of complex eigenmodes we observed in SMA unimorph and bimorph structures corresponding to the first eigenfrequency. This study further allows us to interchange the corresponding eigenmodes of the eigenfrequencies depending upon requirement and condition. Overall, this chapter concludes the exploration of SMA embedded composites and the study of maximising deflection behavior by optimising the structures. An optimised structure is of considerable significance in finding the required combinations of SMA unimorph, SMA embedded with honeycomb, and with reentrant honeycomb core for obtaining the three major torus Gaussian curvatures hence making this study an essential component in the completion of this dissertation.

Chapter 8

Conclusions and Future Work

Overview

This dissertation presents a set of novel SMA-based composites for application in controlled deployment and rigidisation of structures. The bimorph anticlastic and synclastic shape morphing behavior upon SMA actuation sets the composites apart from the conventional composites. Further, the ability to optimize and actively control the shape and natural frequency of the structures by varying the fiber volume fraction and SMA fiber orientation angle give us the scope to advance the application domain of the active SMAHCs. To quantify the hypothesis, we begin with the experimental analysis of the thermoelastic and free vibration response of the unimorph and bimorph SMAHCs. Following this, we model the SMAHCs using the finite element method and, upon validation, extend the study to honeycomb and reentrant honeycomb-based SMAHCs. We conduct a thorough parametric study to expand our understanding of the impact of input parameters on the stiffness and eigenfrequencies. This parametric study serves as a strong foundation for the multi-objective, multi-constraint optimisation study using the Nondominated Sorting Genetic Algorithm. The entire work gives a well-founded design output for the deployment and rigidisation of a flexible structure. A part-wise summary and major findings of the dissertation is collated in the following sections.

8.1 Part I- Experimental analysis of Unimorph and Bimorph SMA Hybrid Composites

- The thermoelastic response and the free vibration response of the composite have been analysed through experiments.
- Bimorph bending of the structure in two-layer SMA reinforcement has been observed using single-point laser sensor and image processing techniques.
- Dependence of deflection on the current causing Joule heating has also been realised. The heating of the SMA wire is controlled through current applied; however, the cooling of the SMA after actuation is allowed through the heat-dissipating to the environment at room temperature. A study based on controlled cooling is envisaged.
- A maximum of 45mm of deflection is obtained from the unimorph, and 22.7mm from bimorph (when top-layer actuated). Since the bimorph deflection behavior, in this case, is slightly less than intended, we propose honeycomb and reentrant-honeycomb core-based SMAHCs.
- To study the effect of separate and coupled SMA layers actuation on the vibration response, the bimorph SMAHC is actuated accordingly. For this, we considered the actuation of top and middle layers separately and then connected them in series and parallel and observed the change in natural frequency.
- The minimum frequency upon complete phase transformation was observed in the case of the series connection of 36.25Hz and the maximum in case of mid-layer of SMA actuation (90o) of 48.75 Hz. The series connection of the SMA wires in the two layers contributes to increased resistance, thus lowering the performance of the composite corresponding to that case. The viscoelastic behavior of the polymer matrix also influences the natural frequency of the system upon a critical rise in temperature. The polymer softening causes an overall reduction in natural frequency; however, it increases the bimorph bending magnitude.
- **The major contribution of this part to the thesis is forming the experimental foundation for the numerical and optimisation problem in the**

latter parts. The sudden drop observed in the coefficient of thermal expansion upon thermal actuation of SMA was an interesting observation and is attributed to the phase transformation of SMA from Martensite to Austenite. The considerable difference between the yield strength of the E-glass fiber and E-glass fiber reinforced silicone matrix was found to be caused due to the fracture but longstanding embedding of the fibers in an elastic medium. The experimental analysis- shape morphing and vibration analysis- gives us vital insight into utilising bimorph behavior and natural frequency variation. This highlights the utility of the SMA in producing not only saddle shape upon bidirectional embedding in composites but also the combination of actuation of these SMA plies to help us manipulate the natural frequency of the structure. We, hence, were successfully able to derive the required zero and negative Gaussian curvature for our envisioned torus structure from the smart composites fabricated, experimented upon, and discussed in this part of the dissertation.

8.2 Part II- Numerical analysis of Unimorph and Bimorph SMA Hybrid Composites

- The numerical models for four sample cases- (a) Unimorph SMAHC, (b) Bimorph SMAHC, (c) Honeycomb core SMAHC, and (d) Auxetic core SMAHC, are discussed in this section.

- Deflection result for the Unimorph SMAHC is validated against the experimental results, and further models are built on the validated result model.

- The mono-clastic, anticlastic, and synclastic bending behavior of the SMAHCs are observed, and the effect of parameters on the bimorph behavior is also discussed. The tip deflection of the honeycomb core and auxetic core is similar when observed for 0.9 strut fiber volume fraction and at 60°reentrant angle, but varies considerably for 0.7 strut fiber volume fraction at reentrant angle 30°. No lateral deflections are observed in the bimorph SMAHC and honeycomb/auxetic core composites. Since the structure undergoes large deformation under thermal actuation, investigation of inter-ply shear, interlaminar slipping, and delamination using a cohesive approach are of interest for future studies. The mode shapes are reported at 66°C where the phase transformation for the SMA completes.

- Maximum deflection of the honeycomb bimorph was found to be 19.73mm, and that of auxetic was found to be 20.11.
- Two new classes of lightweight composites are presented to achieve bimorph behavior with single layer SMA embedding.
- Parametric study showing the effect of input parameters on the bending and vibration response of all the sample cases is also discussed. We successfully remove the dependence of multiple layers of SMA reinforcement for bimorph behavior by utilising the honeycomb and auxetic cores. This remarkably reduces not only the weight and stiffness of the structure but also the complexity of our system, allowing us better structural and vibration control. It is envisaged that these studies will enable us to optimize the design of the composite structure against maximum deflection, decoupling of modes, and desired curvature generation. This model will pave the way for the experimental development of a self-rigidizable SMA reinforced composite structure.
- **The major contribution of this part to the thesis is the formulation of the numerical model, a digital twin, of the SMA unimorph and the SMA bimorph composites fabricated in the previous part. This study was then extended to obtain anticlastic and synclastic surfaces through SMA embedded composites with honeycomb and reentrant honeycomb core. These novel smart composites form vital elements of the torus structure as they give negative and positive Gaussian curvatures upon bending due to SMA actuation. Hence we were able to obtain structures pertaining to our requirement of the major curvatures in a torus. The parametric study that follows the thermoelastic and the vibration analysis of these**

structures gives us an understanding of the variations in the bending behavior and the eigenfrequencies subject to varying SMA volume fraction, SMA fiber orientation, and in the latter analysis concerned with SMA embedded composites with honeycomb and auxetic core with varying lattice or reentrant angles. This part, hence, concludes by obtaining the required elements of a torus structure.

8.3 Part III- Structural Optimisation of Unimorph and Bimorph SMA Hybrid Composites

- In this section, we present the optimisation study of the SMA embedded unimorph and bimorph samples. We start with a comparison study between three popular multi-objective optimisation algorithms- MOPS, NCGA, and NSGA-II for our multi-variable system with no constraints. Based on our results and the deduced inferences, we select NSGA-II for our optimisation problem and select the constraints accordingly.

- Subsequently, we have carried out three optimisation studies corresponding to the maximisation of compliance and decoupling between fundamental natural frequencies in bending and torsion. Through our observations from previous sections, we find the first and second eigenfrequencies of the unimorph and bimorph SMAHCs to be coupled, or in other terms, complex and coupled modes are observed at the first natural frequency.

- The decoupling of the eigenfrequencies of the two sample cases was successfully achieved along with the maximisation of the deflection of the structures.

- It was found that with slight changes in the input parameters- fiber volume fraction and fiber angle orientation, a considerable amount of improvement in the output- bimorph deflection and natural frequency, can be attained.

- We were able to see an almost 57 times increase in the deflection of the SMA bimorph and decoupling of eigenfrequencies by 10 Hz, by changing the SMA fiber orientation angle from 0°to 11°, and 90°to 40°, and thickness from 0.54 mm to almost 1 mm.

- An algorithm has been proposed based on population eigenmodes used to evaluate the variable bounds of the objective functions. We validated the convergence of the obtained Pareto Optimal solution by comparing it with single-objective solutions.

- **The major contribution of this part to the present dissertation is the optimised elemental smart composites for the envisaged torus structure. Apart from this, the complex eigenmodes observed in the previous part were successfully decoupled in a manner such that this method can be utilised to interchange the eigenmodes corresponding to eigenfrequencies by vaying the variables and their bounds. This unique algorithm thus allows us to shift the frequency range as well as interchange eigenmodes of any SMA embedded composite. Another component of this analysis, the maximisation of bending behavior, paves the way for variable sizes of toroidal components by optimising the structure as per the current requirement.**

8.4 Future Scope

The present study has designed a strong foundation for smart auxetic composite structures. The versatility of the work to produce multiple Gaussian curvatures by changing the reentrant angle of the honeycomb and reentrant honeycomb (auxetic) core is the major contribution of this work to the evergrowing field of smart structures. There are several application-based research that we envisage to be conducted based on this study. The first and foremost is the design of a toroidal semi-flexible structure, as discussed at the beginning of this thesis. The plan to obtain this shape has been shown in Figure 8.1 wherein the three major Gaussian curvatures- positive, negative, and zero are attained through the suggested designs in the thesis, and these elements are combined to obtain the complete structure.

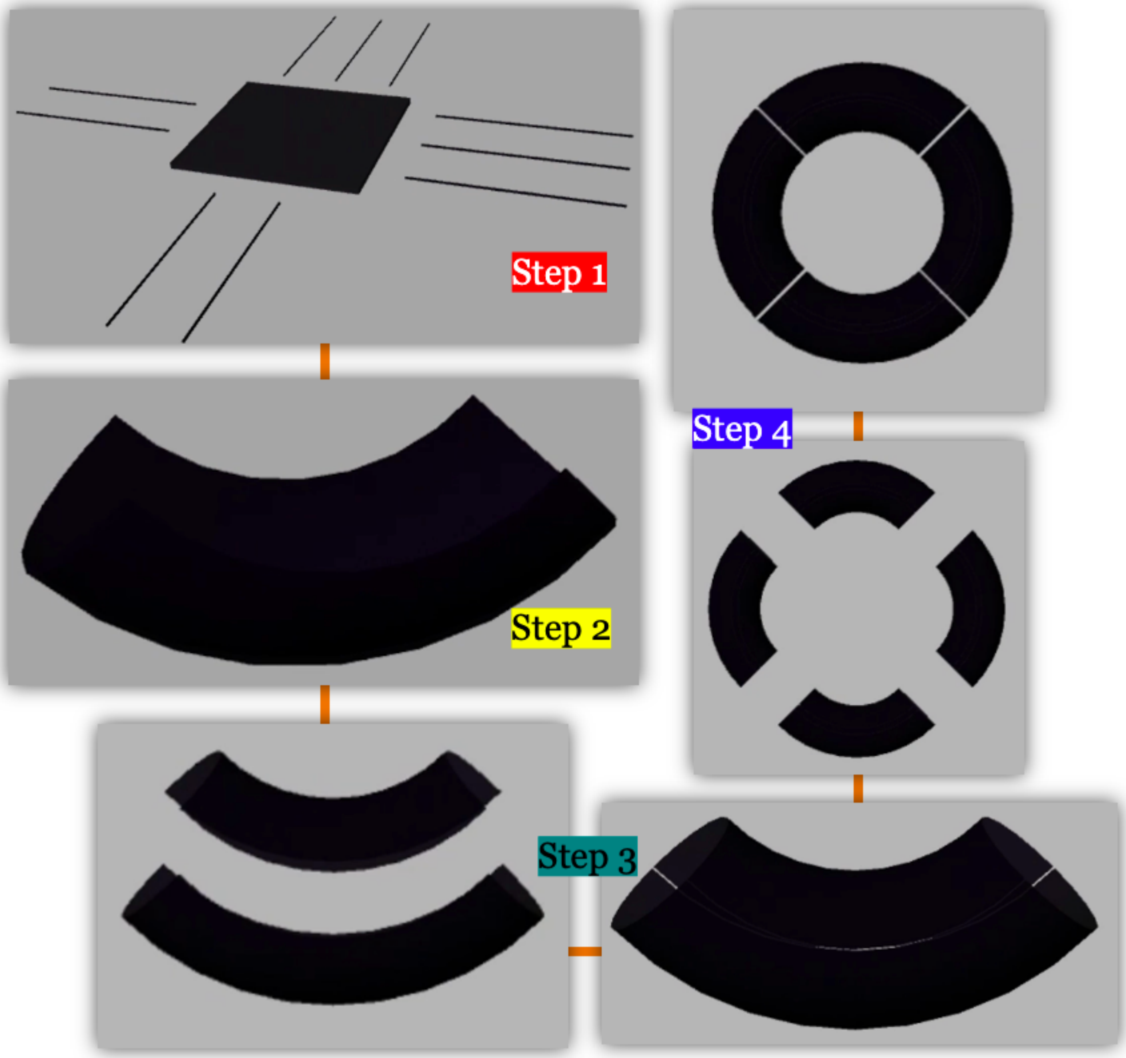

Figure 8.1: A sequential representation of the steps involved for the design of SMAHC based torus for controlled shape control of deployment and rigidisation process.

Another prime application for these structures is as active shape morphing resonators on a tunable metamaterial beam. Previously simple bending SMA resonators have been studied Candido de Sousa et al. (2018); however, the effect of twisting and bimorph bending of resonators has not been considered. A great deal of parametric study can be carried out under this work, and the bandgap can be actively tuned and controlled by optimising the input parameters such as the phase transformation temperature of the embedded SMA, SMA fiber orientation angle, reentrant angle, and fiber volume fraction. With increased input parameters, a wider range of regulating output will be observed, thus expanding the scope of research. We would like to explore the area of Vortexinduced Vibrations observing the change in the pressure distribution on the body by actively modifying the natural frequency of the structure as studied in Chapter 4. The fabrication and testing of the optimised SMA auxetic and honeycomb bimorphs are vital, and we propose it as an extension of our work.

Scientific Papers from Dissertation

S1. Rupal Srivastava, and Bishakh Bhattacharya, '**De-coupling eigenmodes of a shape memory alloy reinforced hybrid composite using multi-objective optimisation**,' *[under review- Journal of Vibration Engineering Technologies]* 2021

S2. Rupal Srivastava, and Bishakh Bhattacharya, '**Thermoelastic and Vibration Response Analysis of Shape Memory Alloy reinforced Active Bimorph Composites**,' *Smart Materials and Structures*, Doi: https://doi.org/10.1088/1361-665X/abc56d 2020

S3. Rupal Srivastava, Ranjeet Kumar, and Bishakh Bhattacharya, '**Vibration response studies of a Bi-morph SMA hybrid composite using 3D Laser Doppler Vibrometer**,' *Smart Materials, Adaptive Structures and Intelligent Systems, ASME*, Doi: 10.1121/1.399683 2020

S4. Rupal Srivastava and Bishakh Bhattacharya, '**Thermoelastic Response Analysis of a Shape Memory Alloy Wire Embedded Active Hybrid Bimorph Composite**,' *Proc. of the 14th International Conference on Vibration Problems, Springer Nature Singapore Pte Ltd.* 2019

S5. Rupal Srivastava, Arun Kumar Sharma, Arup Kumar Hait, and Bishakh Bhattacharya, '**Design and development of active bimorph structure for deployable space application**,' *Proc. SPIE 10595, Active and Passive Smart Structures and Integrated Systems XII, 105953E*, Doi:10.1117/12.2296547 2018

Bibliography

Akbari, T. and S. Khalili (2019). Numerical simulation of buckling behavior of thin walled composite shells with embedded shape memory alloy wires. *Thin-Walled Structures 143*, 106193.

Allred, R. E., A. E. Hoyt, P. M. McElroy, S. Scarborough, and D. P. Cadogan (2002). UV rigidizable carbon-reinforced isogrid inflatable booms. *43rd AIAA/ASME/ASCE/AHS/ASC Structures, Structural Dynamics, and Materials Conference*.

Arrieta, A. F., O. Bilgen, M. I. Friswell, and P. Ermanni (2013). Modelling and configuration control of wing-shaped bi-stable piezoelectric composites under aerodynamic loads. *Aerospace Science and Technology 29*(1), 453 – 461.

Ashir, M., M. Vorhof, and A. Nocke (2019). Influence of thickness ratio and integrated weft yarn column numbers in shape memory alloys on the deformation behavior of adaptive fiber-reinforced plastics. *Composite Structures 215*, 493 – 501.

Baburaj, V. and Y. Matsuzaki (1996). Material damping analysis of smart hybrid composite laminated plate structures. *Journal of Intelligent Material Systems and Structures 7*(4), 427–432.

Bachmann, F., R. de Oliveira, A. Sigg, V. Schnyder, T. Delpero, R. Jaehne, A. Bergamini, V. Michaud, and P. Ermanni (2012, jun). Passive damping of composite blades using embedded piezoelectric modules or Shape Memory Alloy wires: a comparative study. *Smart Materials and Structures 21*(7), 075027.

Bartlett, M. D., N. Kazem, M. J. Powell-Palm, X. Huang, W. Sun, J. A. Malen, and C. Majidi (2017). High thermal conductivity in soft elastomers with elongated liquid metal inclusions. *Proceedings of the National Academy of Sciences 114*(9), 2143–2148.

Baz, A., K. Imam, and J. McCoy (1990). Active vibration control of flexible beams using shape memory actuators. *Journal of Sound and Vibration 140*(3), 437–456.

Baz, A. M. and T.-H. Chen (1993). Performance of Nitinol-reinforced drive shafts. *1917*, 791 – 808.

Bertagne, C., P. Walgren, L. Erickson, R. Sheth, J. Whitcomb, and D. Hartl (2018, may). Coupled behavior of shape memory alloy-based morphing spacecraft radiators: experimental assessment and analysis. *Smart Materials and Structures 27*(6), 065006.

Bhaskar, J., A. K. Sharma, B. Bhattacharya, and S. Adhikari (2020, jun). A review on shape memory alloy reinforced polymer composite materials and structures. *Smart Materials and Structures 29*(7), 073001.

Bidaux, J.-E., Bernet, N., Sarwa, C., Månson, J.-A.E., and Gotthardt, R. (1995). Vibration frequency control of a polymer beam using embedded shape-memory-alloy fibres. *J. Phys. IV France 05*, C8–1177–C8–1182.

Bormann, T., M. de Wild, F. Beckmann, and B. Muller (2013). Assessing the morphology of selective laser melted NiTi-scaffolds for a three-dimensional quantification of the one-way shape memory effect. In N. C. Goulbourne and H. E. Naguib (Eds.), *Behavior and Mechanics of Multifunctional Materials and Composites 2013*, Volume 8689, pp. 281 – 288. International Society for Optics and Photonics: SPIE.

Brinson, L. (1993). One-dimensional constitutive behavior of shape memory alloys: Thermomechanical derivation with non-constant material functions and redefined martensite internal variable. *Journal of Intelligent Material Systems and Structures 4*(2), 229–242.

Buehler, W. J., J. V. Gilfrich, and R. C. Wiley (1963). Effect of lowtemperature phase changes on the mechanical properties of alloys near composition tini. *Journal of Applied Physics 34*(5), 1475–1477.

Candido de Sousa, V., D. Tan, C. De Marqui, and A. Erturk (2018). Tunable metamaterial beam with shape memory alloy resonators: Theory and experiment. *Applied Physics Letters 113*(14), 143502.

Chang, L. C. and T. A. Read (1951). Plastic deformation and diffusionless phase changes in metals the gold-cadmium beta phase. *Journal of Metals 3*(1), 47–52.

Chen, D. and S. Ozaki (2009). Analysis of in-plane elastic modulus for a hexagonal honeycomb core: Effect of core height and proposed analytical method. *Composite Structures 88*(1), 17 – 25.

Chillara, V. S. C., L. M. Headings, R. Tsuruta, E. Itakura, U. Gandhi, and M. J. Dapino (2019). Shape memory alloyactuated prestressed composites with application to morphing automotive fender skirts. *Journal of Intelligent Material Systems and Structures 30*(3), 479–494.

Chopra, I. and J. Sirohi (2013). Smart structures theory. *Cambridge Aerospace Series.*

Cohades, A. and V. Michaud (2018). Shape memory alloys in fibre-reinforced polymer composites. *Advanced Industrial and Engineering Polymer Research 1*(1), 66 – 81.

Cui, D., G. Song, and H. Li (2010, apr). Modeling of the electrical resistance of shape memory alloy wires. *Smart Materials and Structures 19*(5), 055019.

Deb, K., A. Pratap, S. Agarwal, and T. Meyarivan (2002). A fast and elitist multiobjective genetic algorithm: Nsga-ii. *IEEE Transactions on Evolutionary Computation 6*(2), 182–197.

Duerig, T., A. Pelton, and D. Stckel (1999). An overview of nitinol medical applications. *Materials Science and Engineering: A 273-275*, 149 – 160.

Elder, D. C. (1995). *Out from Behind the Eight-Ball: A History of Project Echo*, Volume 16. Amer Astronautical Society.

Epps, J. and R. Chandra (1997, jun). Shape memory alloy actuation for active tuning of composite beams. *Smart Materials and Structures 6*(3), 251–264.

Evans, K. E. and A. Alderson (2000). Auxetic materials: Functional materials and structures from lateral thinking! *Advanced Materials 12*(9), 617–628.

Fonseca, M., B. Abreu, F. Goncalves, A. Ferreira, R. Moreira, and M. Oliveira (2013). Shape memory polyurethanes reinforced with carbon nanotubes. *Composite Structures 99*, 105 – 111.

Freeland, R., G. Bilyeu, G. Veal, M. Steiner, and D. Carson (1997). Large inflatable deployable antenna flight experiment results. *Acta Astronautica 41*(4), 267 – 277. Developing Business.

Geuskens, F. J. J. M. M., J. T. Tielking, S. Koussios, and A. Beukers (2013). Modified linear-membrane formulation for the pressurized torus and multitorus. *AIAA Journal 51*(9), 2114–2125.

Ghaznavi, A. and M. Shariyat (2017). Non-linear layerwise dynamic response analysis of sandwich plates with soft auxetic cores and embedded SMA wires experiencing cyclic loadings. *Composite Structures 171*, 185 – 197.

Gibson, L. J. and M. F. Ashby (1999). *Cellular solids: structure and properties*. Cambridge university press.

Granberry, R., K. Eschen, B. Holschuh, and J. Abel (2019). Functionally graded knitted actuators with NiTi-based Shape Memory Alloys for topographically self-fitting wearables. *Advanced Materials Technologies 4*(11), 1900548.

Grediac, M. (1993). A finite element study of the transverse shear in honeycomb cores. *International Journal of Solids and Structures 30*(13), 1777 – 1788.

Gunton, D. J. and G. A. Saunders (1972). The young's modulus and poisson's ratio of arsenic, antimony and bismuth. *Journal of Materials Science 7*(9), 1061–1068.

Haghdoust, P., S. Cinquemani, A. L. Conte, and N. Lecis (2017). Optimal design of damping layers in sma/ gfrp laminated hybrid composites. *Smart Materials and Structures 26*(10501), 5–13.

Hassan, M., F. Scarpa, and N. Mohamed (2009). In-plane Tensile Behavior of Shape Memory Alloy Honeycombs with Positive and Negative Poisson's Ratio. *Journal of Intelligent Material Systems and Structures 20*(8), 897–905.

Hassan, M., F. Scarpa, M. Ruzzene, and N. Mohammed (2008). Smart shape memory alloy chiral honeycomb. *Materials Science and Engineering: A 481-482*, 654 – 657. Proceedings of the 7th European Symposium on Martensitic Transformations, ESOMAT 2006.

Hassan, M. R., F. L. Scarpa, and N. A. Mohamed (2004). Shape memory alloys honeycomb: design and properties. In D. C. Lagoudas (Ed.), *Smart Structures and Materials 2004: Active Materials: Behavior and Mechanics*, Volume 5387, pp. 557 – 564. International Society for Optics and Photonics: SPIE.

Holschuh, B. and D. Newman (2014). Low spring index, large displacement Shape Memory Alloy (SMA) Coil Actuators for use in macro- and micro-systems. *Proceedings of SPIE - The International Society for Optical Engineering 8975*.

Hua, Y., Q.-Q. Ni, A. Yamanaka, Y. Teramoto, and T. Natsuki (2011). The development of composites with negative thermal expansion properties using high performance fibers. *Advanced Composite Materials 20*(5), 463–475.

Jia, J. and C. Rogers (1989). Formulation of a mechanical model for composites with embedded SMA actuators. *Failure prevention and reliability*, 203–210.

Kalyanmoy, D. (2001). *Multi-Objective Optimization Using Evolutionary Algorithms.* USA: John Wiley and Sons, Inc.

Karimi, M., H. Bayesteh, and S. Mohammadi (2019). An adapting cohesive approach for crack-healing analysis in sma fiber-reinforced composites. *Computer Methods in Applied Mechanics and Engineering 349*, 550–575.

Karimiasl, M., F. Ebrahimi, and B. Akgz (2019). Buckling and post-buckling responses of smart doubly curved composite shallow shells embedded in sma fiber under hygro-thermal loading. *Composite Structures 223*, 110988.

Kennedy, J. and R. Eberhart (1995). Particle swarm optimization. *Proceedings of ICNN'95 - International Conference on Neural Networks 4*, 1942–1948 vol.4.

Khalili, S., M. B. Dehkordi, and E. Carrera (2013). A nonlinear finite element model using a unified formulation for dynamic analysis of multilayer composite plate embedded with SMA wires. *Composite Structures 106*, 635 – 645.

Kirkby, E., V. Michaud, J.-A. Mnson, N. Sottos, and S. White (2009). Performance of self-healing epoxy with microencapsulated healing agent and shape memory alloy wires. *Polymer 50*(23), 5533–5538.

Kuang, K. S. C. and W. J. Cantwell (2003, jul). The use of plastic optical fibres and shape memory alloys for damage assessment and damping control in composite materials. *Measurement Science and Technology 14*(8), 1305–1313.

Kwon, O.-H. and J.-H. Roh (2019). Origami-inspired shape memory dual-matrix composite structures. *Journal of Intelligent Material Systems and Structures 30*(17), 2639–2647.

Lakes, R. (1987). Foam structures with a negative poisson's ratio. *Science 235*(4792), 1038–1040.

Lau, K. T. (2002). Vibration characteristics of sma composite beams with different boundary conditions. *Materials and Design 23*(8), 741–749.

Leal, P. B., R. Petterson, and D. J. Hartl (2017). Design optimization toward a shape memory alloy-based bio-inspired morphing wing. *AIAA/AHS Adaptive Structures Conference 25*.

Lee, K.-J., J.-H. Lee, C.-Y. Jung, and E. Choi (2018). Crack-closing performance of NiTi and NiTiNb fibers in cement mortar beams using shape memory effects. *Composite Structures 202*, 710 – 718. Special issue dedicated to Ian Marshall.

Lelieveld, C., K. Jansen, and P. Teuffel (2016). Mechanical characterization of a shape morphing smart composite with embedded shape memory alloys in a shape memory polymer matrix. *Journal of Intelligent Material Systems and Structures 27*(15), 2038–2048.

Li, Y. (1976). The anisotropic behavior of poisson's ratio, young's modulus, and shear modulus in hexagonal materials. *Physica Status Solidi (a) 38*(1), 171–175.

Lin, H., C. Shao, and D. Cao (2020). Nonlinear flutter and random response of composite panel embedded in shape memory alloy in thermal-aero-acoustic coupled field. *Aerospace Science and Technology 100*, 105785.

Loughlan, J., S. Thompson, and H. Smith (2002). Buckling control using embedded shape memory actuators and the utilisation of smart technology in future aerospace platforms. *Composite Structures 58*(3), 319 – 347.

Machairas, T., A. Kontogiannis, A. Karakalas, A. Solomou, V. Riziotis, and D. Saravanos (2018, sep). Robust fluid-structure interaction analysis of an adaptive airfoil using shape memory alloy actuators. *Smart Materials and Structures 27*(10), 105035.

Masters, I. and K. Evans (1996). Models for the elastic deformation of honeycombs. *Composite Structures 35*(4), 403 – 422.

Meo, M., F. Marulo, M. Guida, and S. Russo (2013). Shape memory alloy hybrid composites for improved impact properties for aeronautical applications. *Composite Structures 95*, 756 – 766.

Michailidis, P., N. Triantafyllidis, J. Shaw, and D. Grummon (2009). Superelasticity and stability of a shape memory alloy hexagonal honeycomb under in-plane compression. *International Journal of Solids and Structures 46*(13), 2724 – 2738.

Miyazaki, S. (1998). Medical and dental applications of shape memory alloys. *Shape memory materials 12*, 267–281.

Mukhopadhyay, T. and S. Adhikari (2016). Effective in-plane elastic properties of auxetic honeycombs with spatial irregularity. *Mechanics of Materials 95*, 204 – 222.

Nagai, H. and R. Oishi (2006, feb). Shape memory alloys as strain sensors in composites. *Smart Materials and Structures 15*(2), 493–498.

Narayanan, P. and M. Elahinia (2016). Control of a shape memory alloyactuated rotary manipulator using an artificial neural networkbased self-sensing technique. *Journal of Intelligent Material Systems and Structures 27*(14), 1885–1894.

Neville, R. M., J. Chen, X. Guo, F. Zhang, W. Wang, Y. Dobah, F. Scarpa, J. Leng, and H.-X. Peng (2017, apr). A Kirigami shape memory polymer honeycomb concept for deployment. *Smart Materials and Structures 26*(5), 05LT03.

Paine, J. S. N., C. A. Rogers, and R. A. Smith (1995). Adaptive composite materials with shape memory alloy actuators for cylinders and pressure vessels. *Journal of Intelligent Material Systems and Structures 6*(2), 210–219.

Pfaeffle, H. J., D. C. Lagoudas, I. G. Tadjbakhsh, and K. C. Craig (1993). Design of flexible rods with embedded SMA actuators. *1917*, 762 – 773.

Pollard, D. D. and R. C. Fletcher (2005). Fundamentals of structural geology. *4*(443).

Riche, R. L. and R. T. Haftkat (1993). Optimization of laminate stacking sequence for buckling load maximization by genetic algorithm. *AIAA Journal 31*, 951–956.

Rossiter, J., K. Takashima, F. Scarpa, P. Walters, and T. Mukai (2014, feb). Shape memory polymer hexachiral auxetic structures with tunable stiffness. *Smart Materials and Structures 23*(4), 045007.

Saeedi, A. and M. Shokrieh (2017). Effect of shape memory alloy wires on the enhancement of fracture behavior of epoxy polymer. *Polymer Testing 64*, 221–228.

Scarpa, F. and P. J. Tomlin (2000). On the transverse shear modulus of negative poissons ratio honeycomb structures. *Fatigue and Fracture of Engineering Materials and Structures 23*(8), 717–720.

Schetky, L. M., C. Liang, and C. A. Rogers (1994). Hybrid composite materials using shape memory alloy actuators to provide vibration and acoustic control. In N. W. Hagood (Ed.), *Smart Structures and Materials 1994: Smart Structures and Intelligent Systems*, Volume 2190, pp. 422 – 433. International Society for Optics and Photonics: SPIE.

Schmit, A. and B. Farshi (1973). Optimum laminate design for strength and stiffness. *International Journal of Numerical Methods in Engineering 7*, 519–536.

Shames, I. and C. Dym (1985). *Energy and Finite Element Methods in Structural Mechanics.* CRC Press.

Shapiro, I. I. and H. M. Jones (1960). Perturbations of the orbit of the echo balloon. *Science 132*(3438), 1484–1486.

Sharma, A. K. and B. Bhattacharya (2019). Parameter estimation of butyl rubber aided with dynamic mechanical analysis for numerical modelling of an air-inflated torus and experimental validation using 3d-laser doppler vibrometer. *Journal of Low Frequency Noise, Vibration and Active Control 38*(2), 296–311.

Silva, S., R. Ribeiro, J. Rodrigues, M. Vaz, and J. Monteiro (2004). The application of genetic algorithms for shape control with piezoelectric patches- an experimental comparison. *Smart Materials and Structures 13*, 220–226.

Sorohan, S., D. M. Constantinescu, M. Sandu, and A. G. Sandu (2019). Design of commercial hexagonal honeycombs of equal out-of-plane shear moduli. *Materials Today: Proceedings 12*, 309 – 318. 35th Danubia Adria Symposium on Advances in Experimental Mechanics.

Sorohan, S., M. Sandu, D. M. Constantinescu, and A. G. Sandu (2015). On the evaluation of mechanical properties of honeycombs by using finite element analyses. *INCAS Bulletin 7*(3), 135.

Srivastava, R., A. K. Sharma, A. K. Hait, and B. Bhattacharya (2018). Design and development of active bimorph structure for deployable space application. In A. Erturk (Ed.), *Active and Passive Smart Structures and Integrated Systems XII*, Volume 10595, pp. 818 – 829. International Society for Optics and Photonics: SPIE.

Stachiv, I., P. Sittner, J. Olejnicek, M. Landa, and L. Heller (2017). Exploiting niti shape memory alloy films in design of tunable high frequency microcantilever resonators. *Applied Physics Letters 111*(21), 213105.

Stiles, L., H. Schaub, K. Maute, and D. Moorer (2010). Electrostatic inflation of membrane space structures. *AIAA/AAS Astrodynamics Specialist Conference*.

Tanaka, K. (1986). A thermomechanical sketch of shape memory effect: One dimensional tensile behavior. *Res. Mechanica 18*, 251–263.

Tao, T., Y.-C. Liang, and M. Taya (2006, Oct). Bio-inspired actuating system for swimming using shape memory alloy composites. *International Journal of Automation and Computing 3*(4), 366–373.

Thomas, S., M. Almanza, and Y. Perriard (2019, July). Design analysis of a Shape Memory Alloy bias-spring linear actuator. In *2019 12th International Symposium on Linear Drives for Industry Applications (LDIA)*, pp. 1–5.

Turner, T., Z. Zhong, and C. Mei (1994). Finite element analysis of the random response suppression of composite panels at elevated temperatures using shape memory alloy fibers. *35th Structures, Structural Dynamics, and Materials Conference*.

Turner, T. L. (2000). A new thermoelastic model for analysis of shape memory alloy hybrid composites. *Journal of Intelligent Material Systems and Structures 11*(5), 382–394.

Valle, G. and N. Wells (2017). Bigelow expandable activity module (beam) ISS year-one.

Werber, F. X. (1980). Analysis and performance of fiber composites, b. d. agarwal and l. j. broutman, wiley-interscience, new york, 1980, 355 pp. price: $24.50. *Journal of Polymer Science: Polymer Letters Edition 18*(10), 689–690.

Young, A. C., W. G. Davids, D. J. Whitney, J. D. Clapp, and A. J. Goupee (2017). Structural testing and analysis of a braided, inflatable fabric torus structure. *Acta Astronautica 139*, 189 – 200.